CONTRIBUTIONS
OF THE ASTRONOMICAL OBSERVATORY
SKALNATÉ PLESO

• VOLUME LI •

Number 1

January 2021

Editorial Board

CONTENTS

EDITORIAL

STARS

THE GATE SUMMER SCHOOL
Brno, Czech Republic, August, 2020

The Contributions of the Astronomical Observatory Skalnaté Pleso
are available in a full version
in the frame of ADS Abstract Service
and can be downloaded in a usual way from the URL address:

https://ui.adsabs.harvard.edu/

as well as from the web-site of
the Astronomical Institute of the Slovak Academy of Sciences
on the URL address:

https://www.astro.sk/caosp/caosp.php

The journal is covered/indexed by:

Thomson Reuters services (ISI)

Science Citation Index Expanded (also known as SciSearch®)
Journal Citation Reports/Science Edition

SCOPUS

EDITORIAL

During 2020, the journal Contributions of the Astronomical Observatory Skalnaté Pleso (CAOSP) published 102 papers on 735 pages within four issues. The journal received 153 citations corresponding to the impact factor of 0.636 for 2019. From September 2020, CAOSP is registered in the Index Copernicus International World of Journals (see `https://journals.indexcopernicus.com/search/details?id=13209`). The content of 2020 issues can be shortly summarized as follows.

Volume 50/1 contains contributions based on lectures presented at the "12-th Serbian Conference on spectral line shapes in astrophysics", held in Vrdnik, Serbia, during June 3-7, 2019.

Volume 50/2 introduces talks and posters from proceedings of the conference "Universe of Binaries, Binaries in the Universe", held in Telč, Czech Republic, during September 7-11, 2019.

Volume 50/3 presents four regular papers, all from stellar astrophysics. Here, we mainly pay attention to the paper on the close eclipsing binary BD And, for which the authors revealed the presence of a third slowly-rotating component, and that devoted to the famous interacting binary beta Lyrae, the first part of a large review.

Volume 50/4 publishes two regular articles (the second part of the review on beta Lyrae, and a particular solution of the polytropic theory of stars) together with two additional contributions from the conference in Telč.

During 2021 we plan to publish four issues with regular articles enriched by five contributions from the summer school GATE, "GAIA & TESS: Tools for understanding the Local Universe" held on-line in Brno, Czech Republic, during August 8–15, 2020.

Finally, we recommend that authors use an updated version of the CAOSP style, v3.08, which introduces some minor changes and fixes. In particular, it implements the author's ORCiD identifier, which will appear in the manuscript's record on both the CAOSP and ADS websites. The updated style can be downloaded directly from the CAOSP website.

Tatranská Lomnica, January 4, 2021

Augustín Skopal, Editor-in-Chief

Richard Komžík, Managing Editor

Formation of magnetized spatial structures in the Beta Lyrae system

III. Reflection of magnetically controlled matter in circumbinary structures in helium lines, in particular arising from metastable levels

M.Yu. Skulskyy

Lviv Polytechnic National University, Department of Physics, 79013, Lviv, Ukraine (E-mail: mysky@polynet.lviv.ua)

Abstract. Spatial gaseous structures in the Beta Lyrae system have been studied with the fact of change in the longitudinal component of the donor's magnetic field during the orbital period in mind. The investigation was based primarily on the study of the dynamics of the circumstellar structures surrounding the binary system as a whole. The special emphasis was placed on the study of complex helium lines, in particular those arising from metastable levels. A number of different observable facts from the ultraviolet to the red spectral region were analyzed. The configuration of the donor magnetic field is a factor that not only enhances mass transfer and influences the formation of spatial gas structures between stellar components but, to some extent, also affects the outflow of matter and the formation of external gas structures around this interacting binary system. Together with previous articles (Skulskyy, 2020a,b), the pieces of evidence of this work, confirming the reflection of magnetically controlled matter in circumbinary structures, define the basis for a coherent picture of the mass exchange between components and outflows of matter outwards.

Key words: binaries: individual: Beta Lyrae – emission-line: magnetic field: mass-loss

1. Introduction

In previous papers, the focus was on the research of the relationship between the structure of the donor magnetic field and its reflection in the characteristic physical parameters of the visible and infrared Beta Lyrae spectra (Skulskyy, 2020a,b). Taking into account the spatial configuration of the donor magnetic field, the emphasis was put on certain facts of its reflection in the moving magnetized accretions structures between the stellar components of this binary system. The data of absolute spectrophotometry and spectral analysis, changes along with the orbital phases of the radial velocities and intensities of complex

emission-absorption lines were examined, primarily based on the own spectral and spectrophotometric observations in the visual range spectrum. This was due to a series of conscious and consistent spectral observations and relevant studies conducted mainly in 1980-1995, after the discovery of the donor magnetic field. Such a method of approach has already made it possible to make certain generalizations and reflect moving magnetized structures as the original phenomenon of mass transfer, which is inherent to this binary system.

It is clear that by the time when nothing was known about the donor's magnetic field and its possible effect on the physical conditions in the near and far gas structures of this binary system, a number of significant scientific studies had been completed. Some physical characteristics and certain parameters of radiating gas structures near both stellar components or in the common shell were often described by the known paradigms, which were later rejected or modified. This is especially true of researchers who have studied the spectral lines of the shell and the characteristics of the spectrum in the far ultraviolet region. A large number of scientific materials are available for their coverage and further rethinking. In this article, special attention is paid to the scientific works in order to investigate the influence of the magnetic field on the dynamics of the circumstellar structure surrounding this binary system as a whole. Clearly, to create a coherent picture, such studies should be conducted in comparison with the already obtained results of the investigation of the magnetized gas structures both near the donor and the gainer and between them.

The previous researches of Skulskyy (2020a,b) demonstrate an efficient collision of magnetized plasma in the phases of observation of magnetic poles on the donor surface. These shock collisions with the accretion disk in the phases of the secondary quadrature, in which the high-temperature environment and the system of formed accretion flows are observed, are especially noted. There are obvious correlations between the phase variability of the donor magnetic field and the corresponding variability of dynamic and energy characteristics of different complex lines, but above all the strongest emission lines H_α and He I λ 7065. Moreover, the phase boundaries of the location of the magnetic pole on the surface of the donor, above which the matter outflows are formed, were discovered. The additional loss of matter from the donor surface is observed mainly from the donor surface in the phase region round 0.855 P, i.e., when the magnetic field pole is facing the gainer. This allowed us to predict certain correlations between the behavior of the above strong lines, as well as certain helium lines formed in shell gas structures extending outward from the binary system. Therefore, in this article, closer attention is paid to such lines of helium, primarily those arising from metastable levels.

It should be recalled that the donor's magnetic field changes significantly during the orbital period (which is close to 12.94 d); phase changes in the range from zero to one are tied to the main eclipse of this binary system in the visible spectral region when the more massive accretor obscures of the bright donor; the schematic model of the Beta Lyrae system and the picture of mass transfer

are shown in Fig.1 of Skulskyy (2020a), which should be kept in mind for a better understanding of the geometry and physical properties of this interacting binary system in further analysis; as this article is a continuation of a number of ongoing comprehensive studies of the proposed topic, references to previous results are quite natural.

2. Magnetic field and gaseous structures surrounding the binary system

2.1. Magnetic field and the He I lines arising from metastable levels around the visual spectrum

The gas shell surrounding the Beta Lyrae system was discovered long ago and its structure has always been studied on the basis of helium lines originating from metastable levels. First of all, it concerned the strongest emission-absorption line of the He I λ 3888 in the violet spectrum. Well-known traditional studies of the broadening shell in the complex line of He I λ 3888 (e.g. Struve, 1941; Sahade et al., 1959) were subsequently extended through the study of this shell in the infrared line of the He I λ 10830 of this triplet series (e.g. Girnyak et al., 1978). It should draw attention that the contours of these lines contain narrow and deep absorption components with negative radial velocities in all orbital phases. If they exceed the parabolic velocities of moving microparticles in the binary system, it has traditionally been believed that the structural components of this shell, in which such lines are formed, move outward from this binary system. The He I $\lambda\lambda$ 3888, 10830 lines have a metastable level of 2^3S. This level is highly populated with electrons and the effects of collision are crucial for the manifestation of these lines in the spectrum. Indeed, absorption components of these triplet lines of helium are well visible in the diluted shell structure around this binary system. At the same time, these helium lines have a very strong emission component in their contours, in many respects similar to those in lines H_α and He I λ 7065 (see Skulskyy, 2020b), where clear intercorrelations were discovered between the phase variability of the donor's magnetic field and dynamic and energy characteristics of these strong emission lines. This may indicate the general nature of the formation and spatial localization of all these emissions. It can be supposed that the absorption in the He I $\lambda\lambda$ 3888, 10830 lines, which cuts through their emission component, arises as self-absorption and should reflect the specificity of the matter loss from the donor surface, which, showing certain structural features of the magnetic field, reaches the Roche cavity. The advanced attempt to re-study the characteristic spectral features of these and other He I lines, which arise from metastable levels, in combination with the corresponding manifestation in the spectrum of the binary system of the donor magnetic field configuration presents new opportunities in this study.

2.2. Magnetic field and He I lines arising from metastable levels in the violet spectrum

2.2.1. The above question and known article by Sahade et al. (1959)

Based on the concept of the existing configuration of the donor's magnetic field, the careful work of Sahade et al. (1959) can be considered as one of the most consistent and informative studies of the He I λ 3888 line. The results of this investigation are based on studies of 195 plates with a dispersion of 10 Å/mm obtained from observations of Beta Lyrae on the Mount Wilson 100-inch reflector over 12 orbital cycles in the 1955 season (the article presents an atlas of photographic spectrograms in the region $\lambda\lambda$ 3680-4580). However, only in 4-7 cycles in June-July they were performed most fully to be suitable for a detailed analysis. In Fig. 1, which is a copy of Fig. 13 from the article of Sahade et al. (1959), "radial velocity measurements from the shell line at He I λ 3888" are presented. As it is seen at the bottom of Fig. 1, where the two absorption components "with very definite" velocities of about -170 km/s and -130 km/s are shown, they converge to one absorption component near the 0.85 P phase of the visibility of the magnetic pole on the donor surface. These absorption components demonstrate very clear sequences over the orbital phases, and, according to the understanding of Sahade et al. (1959), their formation "must occur in a shell that surrounds the whole system". Their radial velocities are the largest and differ in curves shape from such curves of radial velocities of the absorption components that are at the top of Fig. 1. The latter more resemble the absorption components superimposed on emissions in lines H_α and He I λ 7065 (reflecting the gas flows between the donor and the gainer; see Section 2.3 in Skulskyy (2020b)).

It is well known that the He I λ 3888 line also has an emission component, which consists only of the very high red peak in contrast to the two-peak emission, with superimposed absorption, at strong lines H_α and He I λ 7065 (the latter are also above the continuous spectrum in all orbital phases). The violet peak in the He I λ 3888 line is virtually absented owing to deep violet absorption, showing appreciable changes in observations of different investigators (see, for example, Skulsky & Kos, 2011). Fig. 2, which is a copy of Fig. 18 from the article of Sahade et al. (1959), illustrates the radial velocities curve from the red emission peak at the He I λ 3888 line. One sees two maxima at the 0.35 P and 0.85 P phases, i.e., in the phases of visibility of the magnetic field poles on the donor surface (the small local maximum in the 0.6 P phase may reflect the collision of the gas flow with the accretion disk). The similar two maxima are observed on the radial velocity curve of the red peak at the He I λ 4472 line (see Fig. 19 in Sahade et al. (1959)). The red peaks of these helium lines of the violet spectrum exhibit the same behavior as red peaks at the H_α and He I λ 7065 lines. The spectral features of all components at the H_α and He I λ 7065 lines were considered in detail on the basis of Figures 5 and 6 in Skulskyy
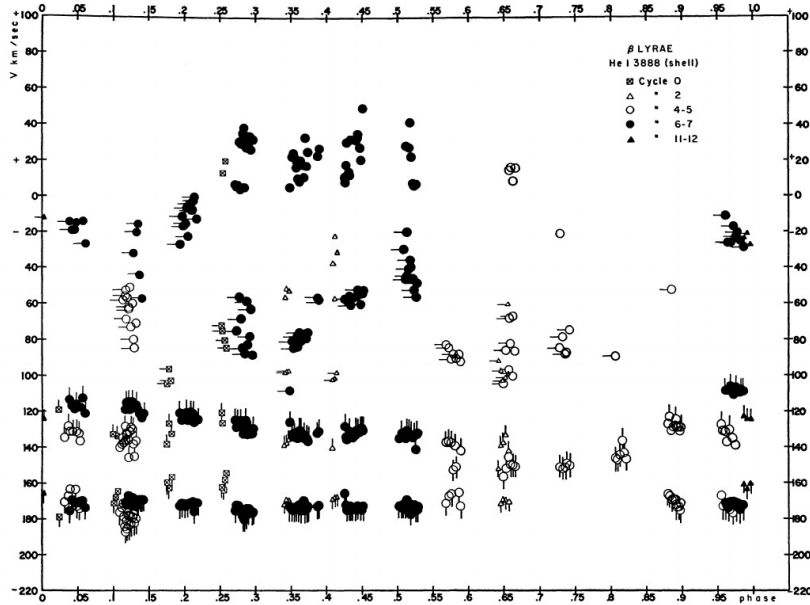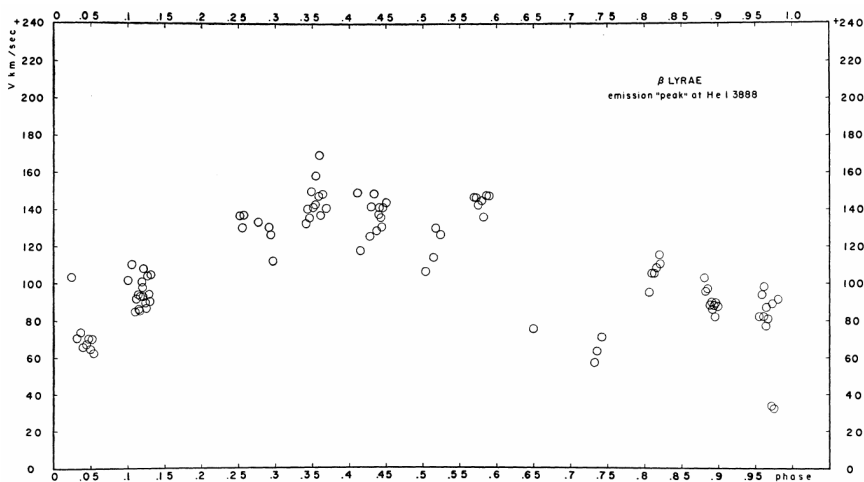
Figure 1. Radial velocities from the shell (triplet) line at He I λ 3888. The "tails" distinguish the groupings which the different components suggest. Two components yield rather constant velocities of about -170 and -130 km./sec. The rest of the components do not behave so regularly and show large differences in different cycles. Adopted from Sahade et al. (1959).

(2020b). These maxima at the 0.35 P and 0.85 P phases match clearly the phases of the two maxima on the curve of the effective magnetic field strength of the donor (see also Fig. 1 in Skulskyy, 2020b). Being synchronized in orbital phases, all these emission components have clear similarities, their physical nature and spatial interconnection seem indisputable. It can be assumed that the formation of red peaks in these lines, including such for the line He I λ 3888, should be associated with the moving radiation near the donor surface, close to the poles of the magnetic field on this surface. This corresponds to the conclusions of Skulskyy (2020b) on the study of dynamics of emission components in the H$_\alpha$ and He I λ 7065 lines.

The dynamic behavior of both the above absorptions of the He I λ 3888 line in Sahade et al. (1959), which are shown at the bottom in Fig. 1, is even more interesting. Their double nature has not been so clearly defined or repeated by investigators in other studies (see, for example Harmanec & Scholz (1993); Skulsky & Kos (2011), which analyzed such studies from the early 20th century). It should be noted that the radial velocity of the center of mass of this binary system, as determined from the interstellar Ca II lines by

Figure 2. Radial velocities from the emission "peak" at He I λ 3888. Adopted from Sahade et al. (1959).

Sahade et al. (1959), is -15.2 km/s. The γ - velocity determined in Table 9, for the set of orbital elements of Beta Lyrae computed on the basis of all 192 spectral plates in the summer of 1955, is -16.0 km/s. The set of orbital elements, calculated from observations taken between 0.85 P and 0.15 P phases, i.e., with the data discarded during the main (or primary) eclipse, showed -15.0 km/s for the -velocity. That is, both absorption components with radial velocities of approximately -170 and -130 km/s, should be considered as components with average velocities of about -155 and -115 km/s. Modern stellar masses of this binary system and the inclination of the orbit (see in Skulskyy, 2020a) allow affirming that the parabolic velocity of the moving gas particles reaches a value slightly smaller, but close to -115 km/s, which is sufficient to reach the Roche cavity with the Lagrange point L2. A simple calculation also shows (Burnashev & Skulskij, 1991) that the velocity of the particles, which is sufficient to reach the Roche cavity with the Lagrange point L3, is near to -160 km/s. That is, the absorption component with an average radial velocity of approximately -155 km/s, or its possible greater values, may indicate a mass loss in a wider range of directions, in particular in the direction of the Lagrange points L4 and L5.

Here it is important to emphasize that Sahade et al. (1959) themselves noted: "there are striking changes with phase and cycle in the spectrum" and "the great complexity of the spectrum of Beta Lyrae makes it impossible to give a description which would do justice to the wealth of information contained in the material". Indeed, at some points, this spectral material is presented as a general description. Now it is possible to consider the data of the observation in the light of modern ideas and concepts, in a more detailed manner. The

behavior of its identified two absorption components of the He I λ 3888 line should be investigated as carefully as possible, supplementing the analysis of radial velocities, given primarily in Table 3 from Sahade et al. (1959). But here there are also several other lines of helium, in particular those arising from metastable levels, which on the basis of tabular data and graphs will help to significantly expand the scope of research.

Based on Table 3, it is possible to estimate the behavior of the absorption of the He I λ 3888 line with a smaller averaged radial velocity. In most orbital phases, Table 3 shows measurements of its radial velocities in the range of 125-135 km/s. This corresponds to a matter outflow velocity of about -115 km/s relative to the center of gravity of the binary system, i.e., with the first parabolic velocity. The most "striking changes with phase and cycle in the spectrum" are visible in the phases (0.95-0.13) P within a wide primary eclipse (see Fig. 1), when the donor is in the process of the eclipse by the gainer hidden in the accretion disk. At the time, according to the data of Table 3, the radial velocity of this absorption, during several days of observations at the boundary from 6 to 7 and from 11 to 12 orbital cycles, is observed in the range from -95 to -105 km/s, i.e., smaller than the parabolic velocity. The significant decrease in the radial velocity of this absorption component at the boundary of these orbital cycles indicates that the gas, flowing in the direction of the gainer in its Roche cavity, can only reach nearer structures of the accretion disk. But this is not observed in the same phases of the zero cycle and at the boundary of 4 to 5 orbital cycles, where the averaged radial velocity is approximately -115 km/s relative to the center of gravity. This indicates that the flows of matter during mass transfer are not laminar and have a variable nature within several cycles. Because in both events the motion of matter is visible above the accretion disk, i.e., the observer behind the gainer records a significant elevation of the moving matter above the plane of the orbit, this determines a considerable height of the rim of this disk from the side of the donor. As shown in Skulskyy (2020b), the vertical component of the gaseous flow in the direction of the gainer can be formed due to the configuration of the donor's magnetic field, in which the magnetic axis is directed at a significant angle to the plane of the orbit of this binary system.

It should be noted that in phases (0.95-0.13) P of the main eclipse, the more negative absorption component in the He I λ 3888 line also shows the various radial velocities in different cycles. In phases (0.95-0.99) P on June 8 of the 4th cycle and on July 4 of the 6th cycle this absorption component shows the average radial velocity of -173 km/s (or -158 km/s relative to the center of gravity), reflecting the motion of matter over the accretion disk, which approaches the velocity of its exit outside the Roche cavity with the Lagrange point L3. The dynamics of gaseous flows recorded in phases (0.03-0.13) P of the 5th cycle when measuring the radial velocity of this absorption component on 8 spectrograms on June 9 and 16 spectrograms on June 10? is most intriguing. In phases (0.03-0.05) P of the first date, the average radial velocity was -170 km/s with its
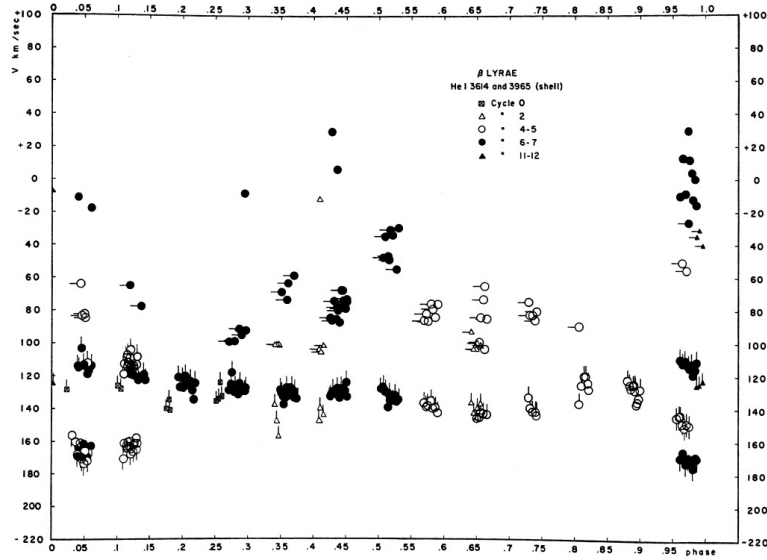
Figure 3. Radial velocities from the shell (singlet) lines at He I λ 3614 and 3964. The "tails" distinguish the groupings which the different components suggest. Adopted from Sahade et al. (1959).

growth within 5 km/s, however, in phases (0.11-0.13) P on June 10, its average the velocity was -180 km/s (on the first 4 plates it was -175 km/s, on the next 4 plates in phase near 0.12 P has reached the average velocity of -185 km/s, then it was -181 km/s and -180 km/s, respectively). Confident achievement of the radial velocity of -185 km (-170 km/s relative to the center of gravity) indicates that in this direction, the velocity of the particles was sufficient for the free escaping of the matter from the binary system with the intersection here of the boundary of the Roche cavity with the Lagrange point L3. But in the phases (0.03-0.05) P on July 5 and (0.12-0.14) P on July 6 of the 7th cycle, the average radial velocity was -171 km/s, which is much smaller than the velocity of -185 km/s in the 0.12 P phase on June 10. Moreover, for example, in the phases (0.987-0.002) P at the boundary of cycles 11 and 12, this absorption component of the He I λ 3888 line revealed a significantly lower average radial velocity of -163 km/s (or only -148 km/s relative to the center of gravity). That is, passing over the center of the accretion disk, the moving matter with such velocity, most likely, must be captured by the outer side of the revolving accretion disk. Therefore, the more negative absorption component of the He I λ 3888 line also indicates that the matter flows during mass transfer are not laminar and have a variable character during one or several cycles.

For comparison of the behavior of the He I λ 3888 line during phases of the

main eclipse, it makes sense to evaluate the behavior of other helium absorption lines arising from metastable levels. Sahade et al. (1959) measured the radial velocities from He I $\lambda\lambda$ 3614, 3965 lines of the singlet series. The radial velocities of their absorption components, as well as for the He I λ 3888 line, are listed in Table 3 and shown in Fig. 3 (as a copy of Fig. 14 from the article Sahade et al. (1959)). In almost all phases, the more negative component of these singlet lines forms a successive curve with an average radial velocity close to -115 km/s relative to the center of gravity (i.e., close to the first parabolic velocity) with complex deviations from it in phases (0.95-0.13) P. This also applies to phases (0.95-0.05) P around the middle of the main eclipse both for the zero's cycle (April 5 as the first observation date in 1955) and at the boundary of the 11th and 12th cycles (September 7 as the last observation date). But an important difference in the variability of these lines around the middle of the main eclipse concerns the observation periods of June 8-10 at the boundary of the 4th and 5th cycles and July 4-5 at the boundary of the 6th and 7th cycles. It is in these June and July observations that two narrower absorption features in these singlet helium lines are clearly distinguished. The development of events should be considered from the end of the 4th cycle, noting that on June 7 in the phases (0.88-0.90) P of direct visibility of the magnetic pole on the donor surface there was the average radial velocity of this absorption of about -115 km/s relative to the center of gravity. A clear rise of the radial velocity of the above absorption at its increment from -130 km/s to -135 km/s for 8 spectrograms occurred on June 8 within the phases (0.96-0.98) P. On June 9, within the phases (0.03-0.05) P, this absorption component during 8 spectrograms reached the radial velocity from -146 km/s for the first 4 spectrograms to -156 km/s for the next 4. Such velocity of moving matter is close to the second parabolic velocity. However, on June 10, within the phases (0.11-0.13) P, this average radial velocity on all 16 spectrograms fell slightly to -148 km/s with respect to the center of gravity. For the first time, these spectrograms clearly manifested the second component of absorption that had an average radial velocity of -97 km/s, somewhat smaller than the parabolic velocity (near -115 km/s relative to the center of gravity). On July 4 of the 6th cycle, 8 spectrograms within the phases (0.96-0.99) P recorded an average radial velocity of -155 km/s for the first absorption component and -98 km/s for the secondary one. On July 5, 7 spectrograms within phases (0.04-0.06) P of the 7th cycle recorded an average radial velocity of -151 km/s for the first absorption component and -98 km/s for the secondary one. However, the next night, July 6, unexpected changes were recorded: all 12 spectrograms in phases of (0.12-0.14) P showed that the radial velocity of the first absorption component dropped to -105 km/s, and the second absorption component disappeared regarding the measurement of radial velocities.

Thus, in the June and July observations, these singlet helium lines, becoming double in certain phases of the main eclipse, reveal asynchronous differences. Between the two orbital rotations from June 10 to July 6, in the same phases (0.11-0.14) P, the spectrum of the binary system represents very different ex-

pressed sets of both absorption components of these lines. If on June 10 both components of these lines became clearly double at radial velocities of -148 km/s and -98 km/s, then after two orbital cycles on July 6 the first of the two absorption components diminished its velocity to -105 km/s, i.e., slightly less than the parabolic velocity, but the second absorption component was absent. Moreover, if in the 5th cycle in June both components of these lines with velocities of -148 km/s and -98 km/s became visible only in the phases (0.11-0.13) P, then in the 6th cycle similar radial velocities -155 km/s and -98 km/s of both these components were measured in phases (0.98-0.99) P on July 4 and close to such velocities -151 km/s and -98 km/s on July 5 (in the 7th cycle) in phases (0.04-0.06) P (the next night on July 6, in phases (0.11-0.14) P the first absorption component had the radial velocity only -105 km/s, and the second absorption component unexpectedly disappeared and was invisible on the following nights of this 7th cycle). Hence, it should be noted that within the main eclipse the He I $\lambda\lambda$ 3614, 3964 lines show two phase segments of significant changes in their intensity and dynamics, which may indicate disordered changes in the density of the accretion disk. They are grouped close to the 0.95 P and 0.05 P phases, which, reflecting the formed dynamically changing structures of the disk, correspond simultaneously to the phases of the maximum manifestation of satellite lines (see Skulskyy (2020a) and more fully Skulskij (1992)). The third region of such changes is formed by the denser matter flow in the phases (0.10-013) P, which opens after the center of the eclipse.

Comparing the changes in the radial velocities in the absorption components of singlet and triplet helium lines arising from metastable levels, it should be especially noted the observation on June 10 in the phase near 0.12 P. In the He I λ 3888 line, there was recorded the radial velocity -170 km/s relative to the center of gravity, which is sufficient for the motion matter from the binary system in any direction, including its exit outside the Roche cavity with the Lagrange point L3. At the same time, for the first time, a clear bifurcation of He I $\lambda\lambda$ 3614, 3964 lines (of the singlet series) into two absorption components with radial velocities comparable to two parabolic velocities was recorded. It is also important that Table 4 and Fig. 15 in Sahade et al. (1959) show that these observations on June 10 recorded on all 16 spectrograms the strongly shifted radial velocities for absorptions, which cut through emissions of H$_\gamma$ and He I $\lambda\lambda$ 4472, 4026 lines. Shifts in the position of these absorptions make up -151 km/s (as the average on the first eight spectrograms) and -141 km/s (on the last eight of them) relative to the center of gravity of the binary system. A similar phenomenon was recorded only during the zero's cycle on April 6 in phase 0.10 P, when measurements of these lines showed on the obtained spectrograms the radial velocity of -157 km/s relative to the center of gravity of the binary system, at clear excess of the second parabolic velocity, sufficient to an outflow matter via stellar wind from the Lagrange point L3.

The events described above, recorded in the behavior of the radial velocities of the absorption components of helium and hydrogen lines in the violet

spectrum, show, within the main eclipse, not laminar but to some extent an unpredictable sharply variable mass transfer between the components of the binary system. In close phases of different dates, the observer behind the mass gainer registers the approach of the matter from the donor to the gainer at different radial velocities above the surface of the accretion disk. It is clear that when such velocities of a matter are slightly smaller than the first parabolic velocity, this matter settles down on the surface of the accretion disk, from the donor side. When the radial velocities of the moving substance exceed the first parabolic velocity or are a significant fraction of the second parabolic velocity, such gas flows can be captured directly by the gainer or the outer parts of the accretion disk. Repeatedly recorded velocities of matter surpassing the second parabolic velocity confirm the direct exit of matter beyond the close circular structures of the binary system and the possibility of forming a distant shell. This agrees with the observations of the radio-nebula, which surrounds the Beta Lyrae system, indicating the substantial non-conservative mass-loss during the evolution of this interacting system (Umana et al., 2000). The obtained generalized picture does not yet have data that would allow us to make specific predictions of the above events. They can be caused by a holistic system of secondary periods and resonances that change synchronously with the growth of the orbital period, variable substructures of the outer layers of the accretion disk, the peculiar spatial configuration of the donor's magnetic field, or other reasons considered in Skulskyy (2020a,b). In addition, the findings on the variable dynamic behavior of the absorption components of the above helium lines may to some extent confirm the results of disk-forming motions of matter in gas-dynamic modeling of stellar structures and accretion disk, given by Bisikalo et al. (2000).

Analyzing the behavior of the radial velocities of the absorption components in complex helium and hydrogen lines, the previous points in this section focused on the details of the transfer of matter from the donor to the gainer within the main eclipse, i.e., in the direction of the gravitational axis of the binary system. It is equally important to evaluate their behavior in the phases associated with the transfer of moving matter in the direction of the axis of the donor's magnetic field. It should be noted (Skulskyy, 2020a) that a dipole magnetic field with the axis in the direction of the orbital phases (0.355-0.855) P has a maximum magnetic field on the donor surface at the 0.855P phase, which reflects the location of this magnetic pole close to the gainer. In addition, the magnetic dipole axis inclined to the orbit plane of the binary system by $28°$, and therefore, this magnetic pole on the surface of the donor in phase 0.855P is also above the plane of the orbit. This means that the ionized gas directed by the donor's magnetic field moves in the direction of the dipole axis from the donor's surface and, deviating along the magnetic field lines towards the accretion disk, can rise above the front edge of the disk without much energy loss.

The tables and graphs in Sahade et al. (1959) allow of stand out certain aspects related to the moving matter in the direction of the axis of the mag-

netic field of the donor. It is reasonable to estimate first the behavior of radial velocities of absorption components of the above lines in orbital phases near 0.85 P, i.e. in the phases of direct visibility on the donor surface of the magnetic pole facing the gainer. From Fig. 1 it is seen that in phases around 0.8 P both absorption components in the He I λ 3888 line form the single absorption with the radial velocity near -135 km/s. This is sufficient for a direct entering of matter in to an external medium in this direction through the Roche cavity with the Lagrange point L2 (the first parabolic velocity relative to the center of gravity of the binary system is near -115 km/s). In these phases, the more negative absorption component of the He I $\lambda\lambda$ 3614, 3964 singlet lines shows a single average radial velocity close to -115 km/s (not showing any bifurcation, see Fig. 3). Several absorption groups with much smaller radial velocities, which are present in other phases, are completely absent in phases before 0.855 P, i.e., the flow of magnetized plasma is manifested as a single whole. In the phases (0.88-0.90) P after 0.855 P, the physical conditions changed. The more negative absorption component in the He I λ 3888 line reached the average radial velocity of -156 km/s, and the absorption of the He I λ 3888 line with a lower average radial velocity approached to a radial velocity near -115 km/s, i.e., to the second and first parabolic velocities, respectively. Evidencing the certain stratification of their formation, the He I lines of both series arising from metastable levels emphasize the average direction of plasma flows in the direction of the donor's magnetic field axis and localization in phases around 0.855 P on the donor surface of the magnetic pole close to the gainer. This indicates that in the phases of direct visibility on the donor surface of this magnetic pole there is an outflow of magnetized matter outwards from the donor surface, as one of the important directions of non-conservative loss of matter during the evolution of this interacting system.

Based on Sahade et al. (1959) observations in 1955 it can be stated that the radial velocities in the phases near both poles of the magnetic field in the He I λ 3888 absorption line showed a radial velocity much higher than the first parabolic velocity (see Fig. 1). However, the stellar wind behaves somewhat differently in the phases of the first quadrature, in particular in the vicinity of the 0.355P phase of the magnetic field pole on the donor surface. This applies, for example, to both the phase interval (0.25-0.5) P in the He I λ 3888 line (see Fig. 1) and phases of (0.25-0.45) P in the H$_\alpha$ and He I $\lambda\lambda$ 4472, 4026 lines (see Figures 13, 15, and 16 and Tables 3 and 4 in Sahade et al. (1959)). Several groups of radial velocities inherent to the corresponding absorption components are visible. The group of absorptions with positive radial velocities around +20 km/s, i.e., +35 km/s relative to the center of gravity of the binary system is important. It indicates that within the (0.35$\pm$ 0.1) P phases of the visibility of the magnetic pole on the donor surface, a runoff of magnetized matter from the observer is formed in the direction of the axis of the donor's magnetic field (0.35-0.85) P. Reflecting the thermal velocity of matter from the surface of the donor, which reaches its Roche cavity, the radial velocity in these phases indicates the

direction of the stellar wind from the surface of the donor. It is directed from the observer along the magnetic axis of the donor to the visibility phases of 0.855P on the donor surface of the magnetic pole facing the gainer, where the magnetic field of the donor reaches its maximum value. As it can be seen from Fig. 3, such a group of radial velocities is not clearly detected in the lines He I $\lambda\lambda$ 3614, 3964, indicating some stratification of physical conditions in the moving matter. But these lines, like the lines He I λ 3888, H$_\alpha$ and He I $\lambda\lambda$ 4472, 4026 have absorption components, which clearly are changed in radial velocities from -60 km/s to -40 km/s in phases of (0.30-0.45) P. This exhibits certain variable events near this pole of the donor's magnetic field that are related, for example, to variations in these phase ranges of the total flux of polarization recorded in Hoffman et al. (1998) and Lomax et al. (2012). To some extent, these changes were studied on the basis of helium lines arising from metastable levels by Skulsky & Kos (2011). Now, this requires detailed coverage and comparison with the evidence of Sahade et al. (1959).

2.2.2. Helium lines arising from metastable levels in more modern studies

As it was previously pointed out, the issues of the dynamics of circumstellar gaseous structures using lines He I $\lambda\lambda$ 3888, 3964, 5015, which arise from metastable levels, were studied by Skulsky & Kos (2011). During 2008-2010, they obtained almost 100 echelle spectrograms with a resolution of about 45 000 on the 2-m reflector of the Peak Terskol Observatory. The narrow absorption components of the He I $\lambda\lambda$ 3964, 5015 showed that the variability of radial velocities and intensities with the phase of the orbital period is practically correlated: both lines formed at approximately the same distance from the center of the system and participate in the same processes. The intensities of these lines reach a minimum in the phases near (0.45-0.60) P, when the donor closes the gap between it and the gainer, simultaneously highlighting the phase direction (0.6-0.1) P perpendicular to the axis of the donor's magnetic field. The intensity of these lines also decreases sharply within less than 0.1 P in the phases of 0.35 P and 0.85 P of polar regions on the donor's surface (more obviously in the He I λ 3964 line, see Fig. 1 in Skulsky & Kos (2011)). But particularly sharp changes are clearly seen in the negative radial velocities of the He I $\lambda\lambda$ 3964, 5015 lines, which indicates complex processes in the orbital structures of this binary system (see Fig. 4, which is a copy of Fig. 2 from Skulsky & Kos (2011)). It can be seen that within 0.1 P in the 0.35 P and 0.85 P phases, which correspond to the location of the magnetic poles on the donor surface, there is a sharp drop in the radial velocity from -55 km/s to -125 km/s, i.e., by 70 km/s relative to the center of gravity of the binary system (γ = -18 km/s according to measurements of the radial velocities of the sharp interstellar line Ca II λ 3933).

The behavior of the radial velocities curve of these helium lines is actually clearly associated with the magnetic field curve obtained in the course of mea-
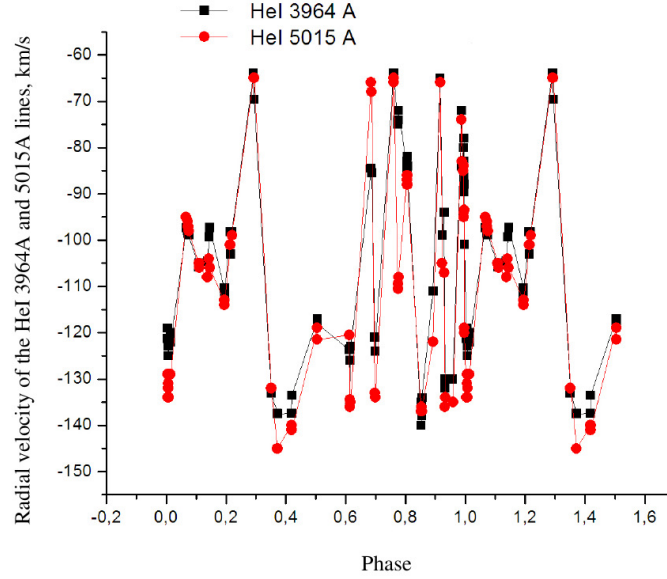
Figure 4. Variations in the radial velocities curve of the He I $\lambda\lambda$ 3964, 5015 lines. Adopted from Skulsky & Kos (2011).

surements of the Zeeman splitting at Si II $\lambda\lambda$ 6347, 6371 lines by Skulskij & Plachinda (1993). The effective intensity of the longitudinal component of the magnetic field varies during the orbital period within $\pm$ 200 G, but as it can be seen from Figures 5 and 6 of Skulskyy (2020a), rapid changes in the magnetic field curve are clearly visible only in the phases near the poles of the magnetic field. In both cases, the polarity of the magnetic field varies within 0.1 P in the 0.355 P phase of the first quadrature and in the 0.855 P phase of the second quadrature. The behavior of the photographic curve of the magnetic field is also characterized by rapid changes in the magnetic field curve around the 0.855 P phase (i.e. the phase of observation of the magnetic pole facing the gainer) and in the phases around the main eclipse.

Note that the sharp peak of radial velocities with a rapid change in their values is observed in Fig. 4 in the phase of about 0.67 P (one can assume that the opening gas flow is in collision with the accretion disk). Similarly formed two narrow peaks of radial velocities are observed in the same phases of the main eclipse, in which the radial velocities of the opposite sign are observed in the satellite lines, characterizing the outer edges of the accretion disk. It should be concluded that due to different physical parameters at the edges of the accretion disk a complex structure of plasma flows is formed, which may participate primarily in mass transfer between components of the binary system, as well as in the outflow of matter outside it. In addition, note that the rapid
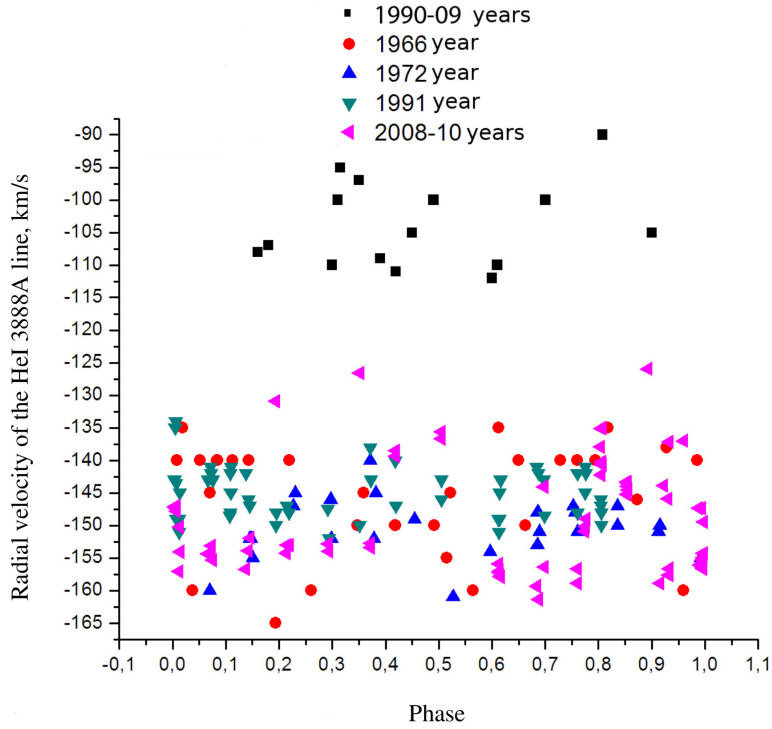
Figure 5. The radial velocity of the He I λ 3888 line in 1900 - 2010. Adopted from Skulsky & Kos (2011).

changes of radial velocities near the main eclipse in the He I $\lambda\lambda$ 3965, 5015 lines (see Fig. 4) are to some extent related to such events recorded in the similar phases (0.88-0.90) P and (0.96-0.98) P of radial velocities from the He I $\lambda\lambda$ 3614, 3965 lines according to their measurements in Sahade et al. (1959) (their behavior was discussed above since the end of the 4th cycle on June 8, 1955). Such a coincidence is not accidental.

Based on observations of the Peak Terskol Observatory in 2008-2010, Skulsky & Kos (2011) also investigated the behavior of radial velocities of the He I λ 3888 line for 1900-2010. Some dynamic characteristics are shown in Fig. 5 as a copy of Fig. 3 from their paper. Without commenting on the nature of the peculiar understatement of radial velocities on the Potsdam 1900-1909 spectra (one can agree with the thorough analysis of this problem conducted by Harmanec & Scholz (1993)), one should note certain points (given the average radial velocity of the center of gravity of this binary system γ = -18 km/s, which is determined within 2 km/s on the spectrographs of the Crimean, Ondrejov and Peak Terskol Observatories). The range of measurements of radial velocities according to our

Crimean observations in 1966-68 and 1972, our more recent observations in 2008-2010 at Peak Terskol, as well as observations in 1991 in Ondrejov, lies in a range from -118 km/s to -142 km/s at the average radial velocity near -130 km/s. There are no such sharp jumps in radial velocities inherent in the curve of radial velocities of the He I $\lambda\lambda$ 3964, 5015 sharp lines shown above in Fig. 4. Well-provided observations of the 1991 season at the Ondrejov Observatory show the average radial velocity in the He I λ 3888 line, which is only about -127 km/s, but the radial velocity curve based on the data in Table 4 and Fig. 3 by Harmanec & Scholz (1993) shows a hump with a value of -122 km/s in the phase range (0.70-0.85) P of the visibility of the magnetic pole on the donor surface (and -132 km/s in the phase of 0.05 P). This is consistent with the convergence of both absorption dependences on He I λ 3888 (see Fig. 1) to a single absorption component, which yields a reduced radial velocity to -(130-135) km/s in the phase range (0.75-0.85) P of the visibility of this magnetic pole on the donor surface as shown in Sahade et al. (1959). In both papers, the flow of matter in the direction of the axis of the donor's magnetic field is significantly greater than the first parabolic velocity. If the difference of 10 km/s in radial velocities between two distant seasons of active observation is real, then this could be a confirmation of long-term changes in the non-laminar loss of moving matter out of the circumstellar structures of this binary system. It should be noted that none of the researchers of the He I λ 3888 line observed this type of bifurcation of its absorption into two different components during the almost entire orbital period. In this aspect, the article by Sahade et al. (1959) remains original and its consideration required special research. This is one of the reasons why this issue was not considered in the report of Skulsky & Kos (2011). Note that the He I λ 3888 line behaves somewhat differently in the known article by Flora & Hack (1975). This thorough article also deserves a detailed review, which for some reason has not been conducted for a long time.

2.2.3. Magnetic field and behavior of shell lines in the known article by Flora & Hack (1975)

In this study, it is necessary to consider the radial velocity curve of the He I λ 3888 sharp absorption line in the paper of Flora & Hack (1975), the variability of which seems somewhat unusual. In most orbital phases these radial velocities should now be considered much smaller than the first parabolic velocity for this binary system (perhaps this is one of the reasons for the inactive use of this work). Flora & Hack (1975) gave the results of the radial velocity (RV) measurements and the profiles and intensities of the most significant lines, which were taken during the international campaign in the period of July 18 - August 1, 1971. The rich spectrographic material (lacking only one day at the orbital period that is about 13 days) consisted of 70 spectrograms of the enough high-dispersion (7 and 12 Å/mm) obtained at the 1.52-m telescope of the Haute Provance Observatory. Flora & Hack (1975) indicate "an asym-

metrical distribution of matter in the envelope surrounding the whole system". They conclude that the behavior of the RV curves for the Balmer and He I shell absorption cores must be real because these lines are virtually independent of blending with absorption lines of the B9 star (or now the donor). It is also noted that "none various absorption or emission features show any correlation with the invisible companion" (or now the gainer). This motivates to consider their rich observational material, drawing on modern concepts in the approach to its interpretation.

Fig. 6, along with other spectral lines, shows the data of measurements of the radial velocities of the He I λ 3888 line, taken directly from the tables of the article of Flora & Hack (1975). If the average velocity of the center of gravity of the binary system is -17 km/s (according to Table 3 in interstellar components line Ca II λ 3933 it is -15 km/s, and in lines of Na I λ 5899 and 5895 it is -19 km/s), all applied radial velocities should in Fig. 6 shift up 17 km/s, in the direction of reducing negative velocities. Then, in phases (0.65-0.85) P, the He I λ 3888 line will show the radial velocities of about -80 km/s relative to the center of gravity of the binary system (which is actually much smaller than the current first parabolic velocity for this binary system). This result immediately revealed several important points in relation to further research. First, the radial velocity -80 km/s is comparable to the average radial velocity obtained on Potsdam spectrograms in the early 20th century, the reality of which has been repeatedly discussed and questioned (see, for example, Harmanec & Scholz (1993)). Second, the stability in profiles, intensity, and radial velocities of the He I λ 3888 line in orbital cycles during the 1971 season can be questioned, based, for example, on significant changes in these spectral characteristics in the observations of Sahade et al. (1959). The question arises of changing the directions of active loss of matter both between stellar components and in relation to circumstellar medium, as well as the reasons for the variable density of such outflows.

Regarding the direction of interpretation of Fig. 6, it is necessary to pay attention to its three parts, which, according to the classification of Flora & Hack (1975), present the radial velocity curves of two of the non-metastable He I $\lambda\lambda$ 5875, 6678 lines of the highest intensities, the metastable lines of He I $\lambda\lambda$ 3888, 5015, 3447, and the shell components of the Na I $\lambda\lambda$ 5889, 5895 lines. One can consider a central part of Fig. 6, which shows three of the five lines measured in Flora & Hack (1975) arising from metastable levels. The absorption components of these lines form dome-shaped curves of radial velocities in the phases of the second quadrature. The maxima of these dome-shaped curves were recorded in consecutive days of observations in the phases (0.78 - 0.77) P and (0.84 - 0.86) P. Similar curves show two more such lines He I λ 3964 and He I λ 6313, the radial velocities of which in these phases are located mainly between the curves of radial velocities of the He I λ 5015 and He I λ 3447 lines (in Fig. 6 there were not introduced so as not to overload the general picture). All five lines of these helium lines with certain potential difference between the upper and lower levels demonstrate clear stratification in the radial velocities, but the
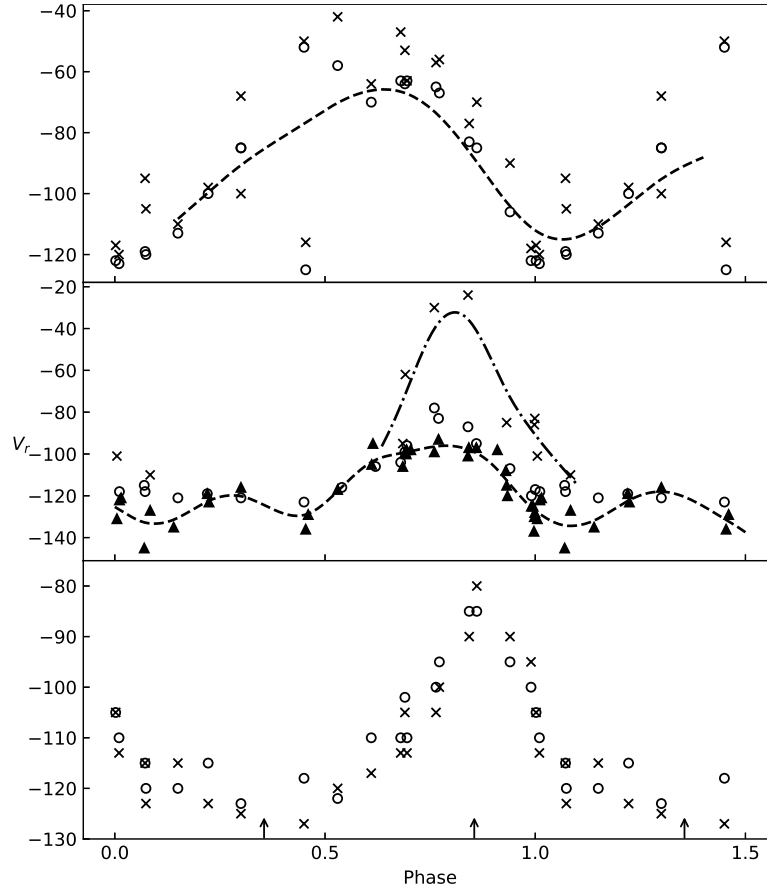
Figure 6. The radial velocities (plotted according to data of Flora & Hack (1975)) for certain shell lines in the Beta Lyrae spectrum. At the top there are lines He I λ 5875 (circles) and He I λ 6678 (crosses); in the middle, there are lines He I λ 3888 (triangles), He I λ 5015 (circles) and He I λ 3447 (crosses); at the bottom there are lines Na I λ 5889 (crosses) and Na I λ 5895 (circles). The arrows in the 0.355 P and 0.855 P phases indicate the direction of the poles of the donor's magnetic field.

matter outflows have velocity much smaller than the parabolic velocity.

Since the observer in phases (0.75 - 0.85) P looks perpendicularly to the line of centers of stellar components and along the axis of the dipole magnetic field of the donor (the motion of matter to the observer), the most adequate explanation of this picture can be considered as the consequences of loss of matter directly from the donor surface near its magnetic pole in phase 0.855 P and its subsequent transfer to the gainer. It should be noted that the He I λ

3888 line shows the single absorption, the radial velocity of which confidently reaches the current value of the first parabolic velocity only in the vicinity of phases (0.0 - 0.1) P, i.e. in the directions of motion of the matter to the gainer, as well as in phases near 0.45 P. It is known that in phases (0.42 - 0.49) P a hot spot is registered on the accretion disk, according to Burnashev & Skulskij (1991) and Lomax et al. (2012). Here, the interpretation of such velocities can be related to the outflow of matter from the donor surface or, conversely, to this surface, reflecting the specifics of the location of the pole of the magnetic field on this surface. Indeed, Burnashev & Skulskij (1991) showed that the observer begins to see excess radiation (hot surface on the donor) only from the 0.355P phase, i.e., along the axis of the magnetic field when its pole opens on the donor surface (see Fig. 1 in Skulskyy (2020b)). This is more likely when the pole of the magnetic field is significantly shifted to the upper hemisphere on the surface of the donor (the magnetic dipole axis is inclined to the orbit plane of the binary system by $28°$ (Skulskij, 1985). Indeed, the hot surface on the donor continues to be observed almost to the 0.50P phase, demonstrating during the orbital phases (0.38-0.49) P the clear variability of the absolute radiation flux in the H_α emission line and the rapid variability of the spectrum in the H_α emission region (see also Alexeev & Skulskij, 1989). This may be a reflection of the collisions of the hot plasma with the donor surface, directed (to the observer with the radial velocity close to the first parabolic velocity) along the lines of force of the magnetic field. Note that in these phases, there is a bifurcation of the absorption component so that both shallow absorption components are superimposed on the strong emission component of lines H_α, He I λ 6678, and He I λ5875, respectively, in Fig. 3d, 6a, and 7a in Flora & Hack (1975). The more violet-shifted component of this absorption shows that the tabular radial velocity approaches in the phase of 0.45 P to current values of parabolic velocity (see Fig. 6). Their occurrence can also be explained by the motion of the magnetic plasma along the lines of force of the magnetic field. In the He I $\lambda\lambda$ 5875, 6678 lines the red-shifted component of this absorption shows much smaller radial velocities close to the velocities in the lines of the donor atmosphere. Interestingly, Flora & Hack (1975) suggested that the violet-shifted absorption in phase 0.45 P may reflect the escape of gas matter through the Lagrange point in front of the donor. Such a hypothesis requires more observational evidence.

The radial velocity curve of the sodium lines resonates with the previous remark. The bottom of Fig. 6 does not so clearly show that the observation phase of 0.375 P (near the phase of 0.355 P of direct vision of the pole of the magnetic field on the surface of the donor) was missed. In the phase range (0.30 - 0.45) P one can assume both a certain minimum of this curve near the 0.355 P phase and a small local hump. In each case, the curve of radial velocities of the Na I $\lambda\lambda$ 5889, 5895 absorption lines clearly manifests itself as the wide maximum of negative velocities near the 0.355 P phase and their clear narrow minimum in the phase 0.855 P, i.e., in the phases of visibility of the magnetic field poles according to the photographic curve of the effective magnetic field strength of

the donor (see Fig. 1 in Skulskyy (2020b)). The presence of narrow interstellar components of the Na I lines allowed us to check the tabular data and to clarify the radial velocities of the shell components of these sodium lines directly from Figs. 7a and 7b of Flora & Hack (1975). Fig. 6 shows that the observation in phases (0.8 - 0.9) P is especially interesting. Since the interstellar components in Na I $\lambda\lambda$ 5889, 5895 lines are -19 km/s, the radial velocity in the direction of the observer in these phases is the smallest one and is only of about -70 km/s, which is much smaller than the first parabolic velocity. Here the observer looks perpendicular to the donor surface along the axis of the magnetic field. Important is the fact of rapid dynamic changes in the moving plasma in the ranges of 0.1 P in phases near 0.855 P, i.e., of the center of the magnetic pole on the donor surface. Within 0.1 P, the movement of the plasma clearly slows down, stops at a certain level, and accelerates again. Hence, the observations of Flora & Hack (1975) clearly state the fact of actual variations in the sign of the RV progression curves of both helium and sodium lines reflecting the direction of motion of matter around the 0.855 P phase. It can be argued that the observations of Flora & Hack (1975) during the 1971 international campaign clearly identified the region of the donor surface that is responsible for the location of the pole of the magnetic field facing the gainer. This is consistent with studies of Zeilik et al. (1982) and Skulsky & Kos (2011), confirming CCD research of the magnetic field by Skulskij & Plachinda (1993).

Radial velocities in the Na I $\lambda\lambda$ 5889, 5895 lines in Fig. 6 do not show a detailed picture of their possible variability in phases (0.95 - 0.05) P of eclipsing of the donor by the gainer wrapped in the accretion disk. The observer sees in phases (0.60 - 0.85) P a gradual decrease in the radial velocities by 30 km/s, which in phase 0.855 P immediately changed to their such gradual increase in phases (0.85 - 0.10) P. One should think that the spatial configuration of the donor magnetic field reflects the direction (0.6 - 0.1) P, perpendicular to the direction (0.35 - 0.85) P of the donor magnetic axis. This is the direction of movement of the plasma perpendicular to the lines of force of the magnetic field in the space between the stellar components under the action of gravity of a massive gainer. It should also be noted that the radial velocity curves of the He I $\lambda\lambda$ 5875, 6678 absorption lines show in certain respects similar behavior. Their average curve at the top in Fig. 6 is made using measurements of the radial velocities of the line He I $\lambda\lambda$ 5875 as a line, the theoretical intensity of which is seven times greater than that of the He I λ 6678 line. The radial velocities of the He I λ 6678 line are located slightly higher than the velocities of the He I λ 5875 lines, but in general, the behavior of these lines with the orbital phase is similar. The extreme values of their radial velocity curves correspond to phases of approximately 0.6 P and 0.1 P, reflecting the direction (0.6 - 0.1) P, perpendicular to the magnetic axis of the donor with the direction (0.35 - 0.85) P. These curves are shifted relative to the 0.855 P phase by about a quarter of the orbital period, as it is seen in comparison, for example, with the RV-curves in Fig. 6 for the Na I $\lambda\lambda$ 5889, 5895 lines. The absorption component with radial

velocities, which changes rapidly in the phases near (0.60 - 0.65) P, is well seen in the higher members of the singlet lines of helium, in particular, as shown in Fig. 6 in the He I λ 3447 line. Starting from the phases (0.60-0.65) P, this may indicate the occurrence of gas flows that are directed perpendicularly to the axis of the donor's magnetic field in the direction of the gainer. Similar behavior in the phases of (0.1 - 0.6) P is demonstrated in the central depth variations of the He I $\lambda\lambda$ 3888, 3964 shell lines at the maximum value in the phase of 0.1 P, and its minimum in the phase of 0.6 P (see Fig. 14 of Flora & Hack (1975)).

It should be noted that all this is consistent with the picture of the directions of the plasma motion of magnetically controlled circumstellar matter in the helium stars according to the study of Shore & Brown (1990) (see Figure 11 in the paper of Shore & Brown (1990), and its representation as Fig. 8 in Skulskyy (2020b)). Their model can be illustrative for the donor as an oblique magnetic rotator of intermediate obliquity because the dipole axis of its magnetic field deviates relative to the orbital plane of the binary system, and the center of the dipole of the donor's magnetic field is significantly shifted in the direction of the gainer. The outflows of matter from the donor surface in the mass transfer picture are possible both in the direction of the donor's magnetic axis and in the direction perpendicular to this axis (see Skulskyy, 2020b). Some proof of this type of phenomenon may be the behavior of a complex line H$_\alpha$ along the surface of the donor. In particular, Fig. 15 of Flora & Hack (1975) shows that the equivalent width of the absorption, measured with respect to the total area of the emission in the H$_\alpha$ line, is halved in the phase direction (0.1 - 0.6) P, and the total equivalent width of emission plus the absorption of the H$_\alpha$ line shows two deep minima in the phases (0.25-0.45) P and about 0.855 P, i.e. near the phases of visibility of both magnetic poles on the donor surface. Of course, to some extent, this is the result of reflecting the characteristics of the donor that fills its Roche cavity: the loss of matter along the axis of the magnetic field at its pole and the loss of matter at the Lagrange point L1, amplified by the massive gainer and deflected by Coriolis forces to the 0.1 P phase, are significantly different. At the same time, the variable motions of the plasma are reflected more clearly in the phases around 0.855 P of the visibility of the magnetic pole, facing the gainer, in accordance with the changes in the polarity of the magnetic field in the observations of Skulskij & Plachinda (1993).

2.3. Magnetic field and the He I λ 10830 line arising from metastable level

If the structure and behavior of the He I λ 3888 line as the second member of the principal series of triplet helium were studied during the first half of the XX century, then to some extent successful observations and studies of the He I λ 10830 line, as the first member of this series, was carried out by Alduseva & Esipov (1969) only in 1961-1962. They used a contact image-converter as an image receiver mounted on a 12-inch reflector. The spectral resolution was
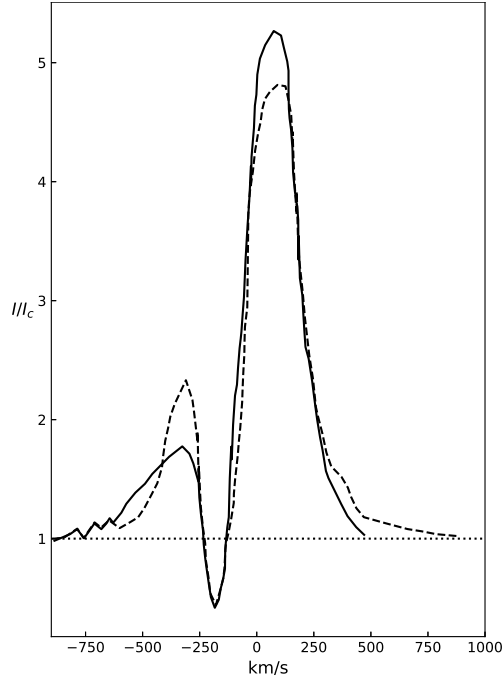
Figure 7. Contours of the He I λ 10830 line in Beta Lyrae spectrum in the phases 0.056 P (solid line) and 0.854 P (dashed line). Adopted from Girnyak et al. (1978).

4.8 Å(11 days of observations in 1961) and 2.8 Å at 9 days of observations in 1962. This highlighted the complex structure of the line contour and gave some initial data on the change with the orbital period of the shell radial velocities and equivalent widths of the emission in the He I λ 10380 line during the orbital period. They indicated that "the line appears in the very external parts of the shell, surrounding Beta Lyrae as a whole". Morgan et al. (1974) made the next attempt in the study of the He I λ 10380 line. They observed on the rapid-scan interferometer at the coud focus of the 2.7-m telescope at McDonald Observatory in April 1973, but received only two spectra in the 0.90 P and 0.13 P phases, respectively. The best resolution of 4.7 Å in the 0.90 P phase allowed them to record the value of the absorption component -140 km/s with an error of 60 km/s.

Our more complete observations of the He I λ 10830 line by Girnyak et al. (1978) were conducted in April-November 1974. There are no data on the following observations, and these studies need more attention. The observations were performed using an electron-optical image-converter of type FKT-1A (S1) mounted on the 50-inch telescope of the Crimean Astrophysical Observatory.
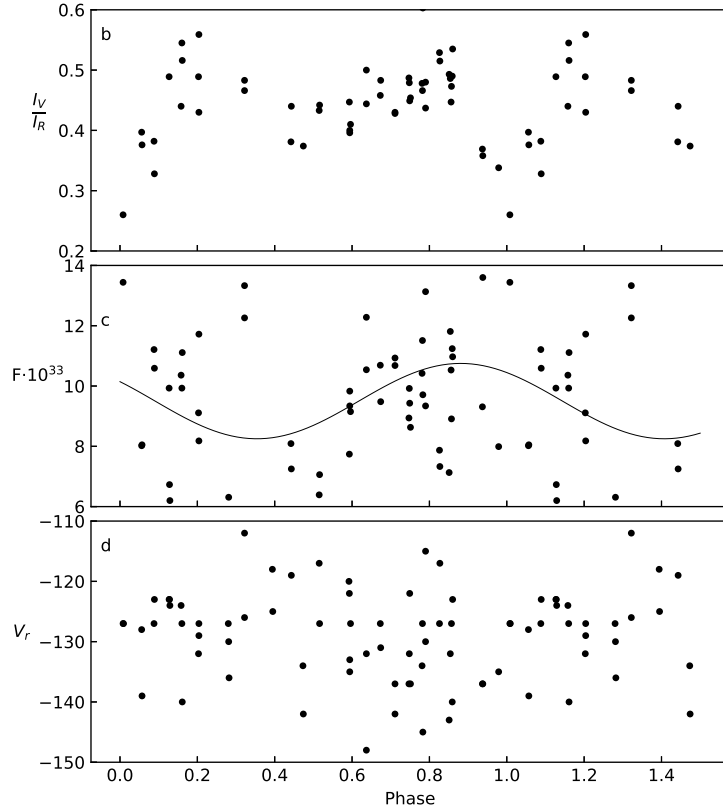
Figure 8. Changes with the phase of the orbital period of the ratio of intensities of emission components, radiation flux, and radial velocities of the absorption component in the He I λ 10830 line (plotted according to Girnyak et al. (1978)).

During 26 nights of this season, 59 spectrograms with a dispersion of 48 Å/mm were obtained, which allowed measuring radial velocities with an error of 10 km/s. As it can be seen from Fig. 7, which is a copy of Fig. 1 from Girnyak et al. (1978), this line in the Beta Lyrae spectrum represents the strong emission that is several times higher with respect to the continuum than such emission in the He I λ 3888 line. The considerable width of the He I λ 10830 line indicates the movements in the gas plasma structures with velocities up to 800 km/s. The deep absorption component, which cuts through the emission, is shifted to the short-wave side. Girnyak et al. (1978) noted that the total intensity and ratio of its short-wavelength and long-wavelength emission components change significantly with the orbital phase. This is a new important factor that requires additional attention and further research.

Girnyak et al. (1978) proposed processed physical parameters of the He I λ 10830 line, introduced in a general table and five figures. Fig. 8 reproduces, on the basis of tabular values, two of these five figures, which are presented below as the radial velocity curve of the absorption component of the He I λ 10830 line and the sum of its absolute fluxes from violet and red emissions components given in erg s^{-1} A^{-1} km/s, multiplied by 10^{33} (contours in the He I λ 10830 line were built in absolute energy units based on six-color colorimetry (Burnashev & Skulskij, 1978)). Fig. 8 indicates some new interesting points. They concern the upper part of Fig. 8, which illustrates the variability in the orbital phase of the ratio of the intensity of the short-wave and long-wave components of emission, i.e. the dependence of $I_v/I_r = f(P)$, which we built here on the basis of the tabular data. In Fig. 8, bottom, it is seen that the $V_r = f(P)$ curve of the absorption component, which separates these emission components, remains approximately the same in the orbital phases at an average value of about -130 km/s (taking into account the radial velocity of -18 km/s for the center of gravity of this binary system). The largest scattering of data and rapid changes in radial velocities are observed in the range of phases (0.7-0.9) P, and a particularly sharp velocity change is shown in the phases around 0.855 P of the visibility of the magnetic pole, facing the gainer. Similar behavior in these phases there is in changes of contours in the He I λ 10830 line (see the middle part of Fig.8). Despite some sharp changes in the total emission, which can occur at times from tens of seconds to tens of minutes (see, e.g., Alexeev & Skulskij (1989) and Skulskyy (2020b)), some trend is observed to a sinusoidal curve of the absolute flux of the total emission with extrema in the phases of (0.35-0.45) P and 0.85 P. It is known that these phases correspond to the phases of both extrema of the donor's magnetic field (Burnashev & Skulskij, 1991; Skulskij & Plachinda, 1993). This picture is more clearly manifested in the dependence of $I_v/I_r = f(P)$ (the upper part of Fig. 8), characterizing the expected variability of shell structures in this binary system. The dependence of $I_v/I_r = f(P)$ showed a clear decrease in the I_v/I_r ratio after the 0.855 P phase (of the direct visibility of the magnetic field pole on the donor surface) to the minimum in the main eclipse phase and its rapid rise to the phase 0.15 P, when the main flow of matter from the donor to the gainer, deflected by the Coriolis forces, begins after the main eclipse. It should be noted that these observations do not provide enough data for more definite conclusions in the phases (0.95-0.05) P of the main eclipse.

Nevertheless, the radial velocity curve of the He I λ 10830 line looks similar to that of the He I λ 3888 line defined by Skulsky & Kos (2011) over five different seasons (see Fig. 5 above). Figs. 5 and 8 show that the average values of the radial velocity of the absorption components of the first two triplet helium lines are close to -130 km/s relative to the center of gravity of the binary system, which significantly exceeds the first parabolic velocity. It could be assumed that the sharp absorption components of both lines are formed in a dynamically identical medium moving in all directions relative to the center of gravity of the binary system. Moreover, the strong emission of the He I λ 10830 line does
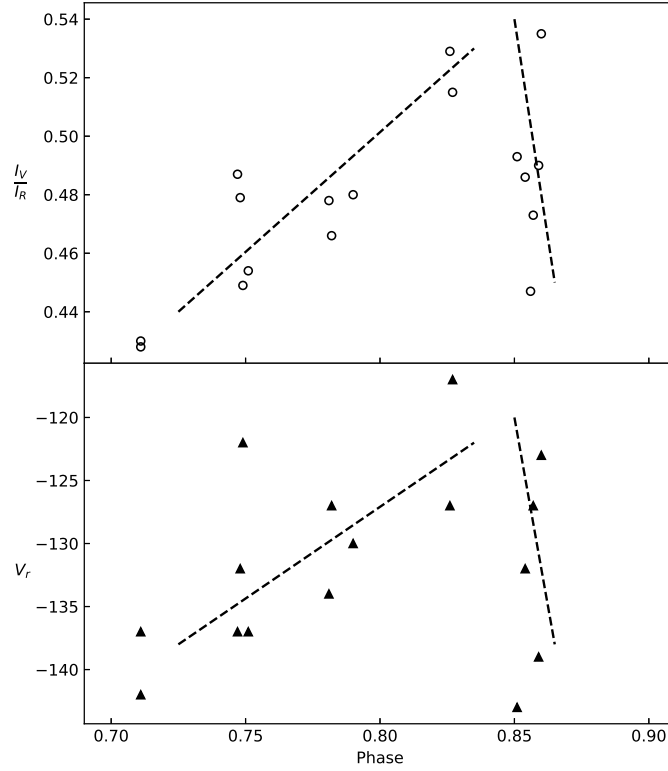
Figure 9. The same as in Fig. 8 for the He I λ 10830 line, but on an enlarged scale in phases near 0.855 P of direct visibility of the magnetic pole on the donor surface.

not explicitly distort the position of the absorption component, and the radial velocity of the emission center as a whole turned out to be close to the orbital velocity of the gainer, based on the previously established mass ratio of the stellar components (Skulskij, 1975). However, Figs. 1 and 6, which respectively relate to the studies of Sahade et al. (1959) and Flora & Hack (1975), showed that the behavior of the He I λ 3888 line at different seasons and epochs can significantly differ. Such facts are real, they required a detailed consideration of some, unnoticed by Girnyak et al. (1978), dynamical characteristics of the He I λ 10830 line at certain parallels in the study of the lines He I λ 3888 and He I λ 10830.

First of all, this applies to the phase interval (0.75-0.9) P around the 0.855 P phase of the direct visibility of the magnetic field pole on the donor surface close to the gainer. Note that the observations of 1971 by Flora & Hack (1975) and our observations of 1974 by Girnyak et al. (1978) can be attributed to fairly

close seasons and the dynamic behavior of the shell lines He I λ 3888 and He I λ 10830 may have some similarity. As it can be seen from the bottom of Fig. 8, our observations were most frequent in the (0.7-0.9) P phases, showing rapid changes in the radial velocity at large amplitudes of their variability. The observation data at these phases were rebuilt on a larger scale in Fig. 9. It can be seen that the radial velocity curve of the He I λ 10830 line in these phases, like the domed-shaped curve in Fig. 6 for the He I λ 3888 line, also has a domed-shaped peak at a clear rise in negative radial velocity immediately after the phase 0.855 P of direct visibility of the magnetic pole on the donor surface. This peak of the radial velocities of the He I λ 10830 line that changes in the ranges of 0.1 P within 20 km/s is twice smaller than that for the He I λ 3888 in Fig. 6. At least, this points to some analogies in the dynamic parameters of gas structures in which these triplet helium lines were formed in the first half of the 1970s. The decrease of negative radial velocities at approaching the 0.855 P phase and their subsequent rapid increase after this phase in the He I λ 10830 line (as well as in metastable lines of He I $\lambda\lambda$ 3888, 5015, 3447, and the shell components of the Na I $\lambda\lambda$ 5889, 5895 lines - see Fig. 6 built on the data of Flora & Hack (1975)) indicates the similarity of physical processes along the donor surface near this magnetic field pole.

At the same time, the He I λ 3888 and He I λ 10830 lines show a physically significant difference in radial velocities. It is clearly seen that if in the He I λ 10830 line in Fig. 9 in all phases, including phases (0.6-0.8) P, the radial velocities are greater than the parabolic velocity, then in the He I λ 3888 line according to Fig.6 in phases (0.6-0.8) P, they are much smaller than the parabolic velocity. This indicates the nonstationarity of the outflow of matter and the variable flow density in the direction of the dipole axis of the magnetic field. The clear changes, which were noticed in the absolute radiation flux (the central part of Fig. 8) within (0.8-0.9) P, also reflect the complex structure of the emission formation near 0.855 P in this short phase interval with a width of approximately 0.1 P. This emphasizes that rapid changes are inherent in these phases of both energy and dynamic parameters of the magnetized plasma. The rapid change in radial velocities near 0.855 P may indicate that the vector components of the magnetized plasma motion at the edges of the magnetic field pole are superimposed on the total plasma motion in the direction of the donor magnetic field axis. This one can also see from Fig.4, which demonstrates similar variations in the radial velocities of the He I $\lambda\lambda$ 3964, 5015 lines in the short phase interval with a width of approximately 0.1 P in phases of the visibility of both magnetic field poles on the donor surface. The observations of Girnyak et al. (1978) in phases (0.25-0.45) P are not dense enough to conduct a detailed analysis of the behavior of the He I λ 10830 line in the phases of visibility of the magnetic field pole on the donor surface in the first quadrature, although, in these phases, the radial velocities of this line are also subject to abrupt changes similar to Fig.4. However, as a whole, the above research facts confirm the general picture of the behavior of energetics and dynamic parameters of magnetized plasma caused by

a certain configuration of the donor's magnetic field. The study of the spectral characteristics of the He I λ 10830 line has led to certain clarifications in the formation of the picture of the transfer matter between stellar components and its movement into the medium around the Beta Lyrae system.

3. Conclusions and discussion

The study of shell structures in the Beta Lyrae system seemed natural on the basis of previous studies by Skulskyy (2020a,b), which involved a continuous interaction of the outer shell with a complex system of plasma flows between the donor and the gainer. It is clear that the spectral lines formed in external structures, in particular the helium lines arising from metastable levels, were studied. Scientific articles were used for the study, which, on the basis of qualitative observations, covered the orbital period well. There are few similar works, in particular Sahade et al. (1959); Flora & Hack (1975); Girnyak et al. (1978), which are half a century old. It is to some extent well that the authors of these works presented their results without the influence of modern interpretations, say, without information about the magnetic field of the donor or ideas about bipolar jet structures associated with the accretion disk. However, these articles have a lot of important spectral material in the form of published tables and graphs. As a whole, this material, together with data from more recent publications of Harmanec & Scholz (1993) and Skulsky & Kos (2011), have not been analyzed in more detail. Here an attempt was made to overcome this shortcoming.

All researched articles are distinctive. They differ significantly in the energy and dynamic parameters of the moving plasma in the medium near each component and between stellar components of the binary system. First, significant long-term differences were found within half a century in the movements of matter to the gainer and in external structures. Second, there are significant differences in the physical parameters of this plasma within one observation season and their variations from cycle to cycle (especially in Sahade et al. (1959)). It was established (see Fig. 1) only in Sahade et al. (1959) that: "He I λ 3888 has two components with very definite and fairly constant velocities" of about -155 km/s and -115 km/s (in the 1955 season), i.e., close to the second and first parabolic velocities. In Flora & Hack (1975), the absorption component of the He I λ 3888 line in certain phases of the 1971 season is approximately -80 km/s, which is much less than the parabolic velocity (see Fig. 6). The averaged radial velocity of the absorption component in the He I λ 3888 line during the 1991 season is -127 km/s (see also Fig.3 in Harmanec & Scholz (1993)), which is very different from that in the previous two articles. The He I $\lambda\lambda$ 3964, 5015 lines (Fig. 4) show rapid changes in radial velocities in the range from -55 km/s to -125 km/s in short phase intervals up to 0.1 P, in particular close to the magnetic field poles, which were recorded in the seasons 2008-2010 in Skulsky & Kos

(2011). It seems that all these differences are not periodically ordered. It should be emphasized that all researched articles show the averaged radial velocity in the He I $\lambda\lambda$ 3888, 10830, i.e., the velocity of the outflowed plasma in external structures, to be of about -130 km/s, except for one orbital cycle in 1971, in which observations by Flora & Hack (1975) were made.

The article gradually reveals the analyzed facts from the available spectral material, and since there is quite a substantial amount of them, they are further presented as touches of the obtained research picture in a possibly concise form. It turned out that this picture is based on fragments of a generalized investigation during the orbital period. They can be grouped into certain phase intervals as a reflection of slightly different physical processes occurring in them. Formally, they can be divided into five interconnected intervals. The phase range (0.95-0.05) P reflects nonstationary processes that occur during the transfer of mass to the gainer at the donor eclipse by the accretion disk. The phase range (0.07-0.14) P reflects the motion of the main gas flow deflected by Coriolis forces outside the accretion disk. It is necessary to distinguish the behavior of plasma structures near the phases of visibility of both poles of the magnetic field (0.30-0.45) P and (0.75-0.90) P, as well as within the range of phases (0.4-0.6) P eclipse of the accretion disk by the donor.

There are a number of effects and events associated with the eclipsing of the donor surface by the accretion disk in the phases (0.9-0.1) P of the main eclipse of the binary system. It can be noted that within phases (0.95-0.05) P of the deeper eclipse, the He I $\lambda\lambda$ 3614, 3964 and He I λ 3888 absorption lines show, according to Sahade et al. (1959), two main regions of changes in their intensities and radial velocities. They are grouped near the 0.95 P and 0.05 P phases, which corresponds to the phases of maximum accretion disk density. This follows from many studies, in particular from phase changes of the equivalent widths of satellite lines in 1991-1992 (see Fig. 2 in Skulskij (1993c), or from the light curve based on observations by the BRITE Satellites in May-October 2016 (see Fig. 2 in Rucinski et al. (2018)). In these phases, there is the greatest variability of the radial velocities of both absorption components of the He I $\lambda\lambda$ 3614, 3965 and He I λ 3888 lines. Their more negative shifted component varies in the range from -140 km/s to -160 km/s, sometimes reaching the second parabolic velocity (near -160 km/s) without a certain regularity in orbital cycles. This also applies to the center of the eclipse in different orbital cycles in phases (0.98-0.02) P, where the radial velocities also show variation within the same limits (for example, in phases (0.98-0.99) P at the end of the 6th cycle on July 4, 1955, their radial velocity was -(155-160) km/s, that is sufficient for an outflow matter from the Lagrange point L3). It is clear that in the range (0.95-0.05) P the dynamic behavior of moving matter reflected in the more negative absorption component in the He I $\lambda\lambda$ 3614, 3964 and He I λ 3888 lines can be the product of instability processes of the matter transfer between the stellar components. The less negative absorption component of the He I λ 3888 line in these phases reaches only the first parabolic velocity, and in the He I $\lambda\lambda$ 3614, 3964 lines

they only approach it or are much smaller, also demonstrating the fact of non-laminar, but clearly variable events during the mass transfer. It should be noted that the observations of Sahade et al. (1959) were carried out in the 1955 season with significant phase gaps during the day (its time is $0.077\,\mathrm{P}$), which does not allow to clarify the structure of the accretion disk. The important fact of the detection of disk-shaped structures in phases $(0.95\text{-}0.05)\,\mathrm{P}$ are the observations of Skulsky & Kos (2011) during 2008-2010, which clearly show rapid changes of radial velocities from -55 km/s to -125 km/s in He I $\lambda\lambda$ 3965, 5015 singlet lines (see Fig. 4) in two short phase intervals.

Thus, the variable nature of the flows of matter during mass transfer in phases of the main eclipse indicates eruption processes on the donor, the appearance of matter clots over the rims of the disk from the side of the donor and their movement in the direction to the observer over the surface of the accretion disk accelerated by the massive gainer. Incidentally, Skulskyy (2020b) showed that the vertical component of the plasma flows in the direction of the gainer can be formed due to the configuration of the donor's magnetic field, in which the magnetic axis is inclined at a significant angle to the orbit of the binary system. The structure of gas flows above the surface of the accretion disk significantly depends on the location of the magnetic pole on the donor surface relative to its distance to the gainer and relative to the plane of the orbit. These remarks also apply to the third region of active events in the phases $(0.9\text{-}0.1)\,\mathrm{P}$ reflected in the changeable and denser flows of matter in the phases $(0.07\text{-}014)\,\mathrm{P}$, which start after the center of the main eclipse of the binary system. The dynamic behavior of the moving matter in the He I $\lambda\lambda$ 3614, 3964 and He I λ 3888 lines is similar to that in the phase range $(0.95\text{-}0.05)\,\mathrm{P}$. Interestingly, the highest radial velocity for the observation season in Sahade et al. (1959) was recorded in phases $(0.11\text{-}0.13)\,\mathrm{P}$ of the 5th cycle on June 10, 1955. The more negative absorption component of the He I λ 3888 line showed the velocity of -(160-170) km/s, which is more than enough for the outflow of the matter from the Lagrange point L3. These more dense gas flows, when deflected by Coriolis forces outside the accretion disk in the Roche cavity of the gainer, push the outer part of the disk to the gainer surface (see Skulskij, 1992; Skulskyy, 2020a).

The range of phases $(0.4\text{-}0.6)\,\mathrm{P}$ eclipse of the accretion disk by the donor, as a specific part of the orbital period, deserves a separate study (by analogy with the studies in phases $(0.9\text{-}0.1)\,\mathrm{P}$ of the primary eclipse). The preliminary study of existing observations in this phase range leads to certain conclusions and ideas about the behavior of physical parameters in the vicinity of both stellar components. Although they require additional observations, they were worth paying attention to. Analysis of Tables 3 and 4 together with their illustrations 13-16 in the article Sahade et al. (1959) (see also Fig. 1-3 above), as well as the study of Skulskij (1992, 1993b,a,c); Ak et al. (2007) and others, leads to the conclusion that in these phases, in addition to complex shell lines formed near the accretion disk, clear changes of the curve of radial velocities of the gainer lines are visible. Their behavior can be explained by the Rossiter effect in the

passage of the donor in front of the accretion disk. In phases (0.38-0.50) P the
right part of the disk is observed (its left part being closed by the donor); in
phases (0.45-0.55) P the central parts of the disk, closed by the donor, pass in
front of the observer; in phases (0.5-0.6) P dominates in these lines the left part of
the accretion disk (the donor obscures the right part of the disk). Approximately
at 0.62 P, this effect disappears (further there are opened phases of the collision
of the main flow into the accretion disk and the region of the magnetic field
pole on the donor surface). In particular, this effect is well observed in phases
(0.38-0.62) P in the behavior of the gainer radial velocities of the Si II $\lambda\lambda$ 6347,
6371 lines, for example, in Fig. 3 in Skulskij (1992), where it was revealed, and,
especially in Fig. 5 in Ak et al. (2007). It is more likely that these lines are
formed near the central part of the disk.

The visibility phases of both poles of the magnetic field (0.30-0.45) P and
(0.75-0.90) P as specific parts of the orbital period are important for obtaining
a general picture of the influence of the donor's magnetic field on moving mag-
netized gas structures in near and farther medium regarding the donor. Some of
the key facts identified in this study are, first of all, illustrated by the behavior of
the radial velocities of helium lines arising from metastable levels. Fig. 1 shows
that only within phases of about 0.1 P near the phases 0.855 P, both absorption
components of the He I λ 3888 line in Sahade et al. (1959) converge into a single
absorption with radial velocities in the range -(125-135) km/s, i.e., with a radial
velocity much greater than the first parabolic velocity. This indicates that in
the phase of direct visibility of the pole of the magnetic field on the surface of
the donor facing the gainer, the matter outflows in the direction of the axis of
the donor magnetic field, perpendicular to the surface of the donor. According
to Fig. 3, the radial velocities from the shells of the He I $\lambda\lambda$ 3614, 3964 singlet
lines, although showing some stratification of their formation relative to the
line He I λ 3888, indicate that the He I lines of both series in phases close to
0.855 P behave in these phases in a similar way. The particularly sharp peaks
of radial velocities with a rapid change in their values are observed in Fig. 4 in
the He I $\lambda\lambda$ 3964, 5015 lines according to Skulsky & Kos (2011). Within 0.1 P
in the 0.355 P and 0.855 P phases, there are sharp changes in the radial velocity
from -55 km/s to -125 km/s, or 70 km/s relative to the center of gravity of
the binary system. This indicates complex processes in the plasma structures of
this binary system, which are close to the location of the magnetic poles on the
donor surface. It should be recognized that Fig. 9 also confirms that the rapid
changes in the radial velocity of the He I λ 10830 line in phases immediately
close to 0.855 P (at the mean velocities over the orbital period near -130 km/s -
see Fig. 8) indicates the reality of rapid changes in plasma movement and events
in this phase range.

Evidencing certain stratification of their formation, the He I lines of both
series show in theses phases a certain relationship between their dynamic and
energy parameters. Figure 9 also shows the parallel changes in the profile of
the He I λ 10830 line expressed through the dependence of $I_v/I_r = f(P)$, i.e.,

the ratio of the intensity of the short-wave and long-wave components of these emission profiles. This dependence is similar to the radiation increasing near the 0.855 P phase on light curves in the range of (3.5-4.6) m in Zeilik et al. (1982), which allowed to identify (see Skulskyy, 2020b) on the donor surface the region of this magnetic field pole. Figure 2 illustrates also the radial velocity curve from the red emission peak at the He I λ 3888 line. Such two maxima are observed on the radial velocity curve of the red peak at the H$_\alpha$ line (see Figures 5 in Skulskyy (2020b). The maxima at the 0.355 P and 0.855 P phases coincide with the phases of the two maxima on the curve of the effective magnetic field strength of the donor (see Figure 1 in Skulskyy (2020b) or Figure 2 in Burnashev & Skulskij (1991)). Moreover, the radial velocity curve for the Gaussian center of emission in H$_\alpha$, as well as for such centers on radial velocity curves of the He I $\lambda\lambda$ 6678, 7065, and Si II $\lambda\lambda$ 6347, 6371 lines, see Figure 6 in Skulskyy (2020b), demonstrate that both their maxima match the extrema of the effective magnetic field strength of the donor (a similar shift on the V_r-curve of the center of the He I λ 10830 emission as a whole is discussed by Girnyak et al. (1978)). The generation of the radiation flux and the formation of the emission-absorption profile of these lines can be largely carried out under the influence of the existing configuration of the donor magnetosphere in the interconnected spatial structures.

A similar conclusion is supported by the observations of Flora & Hack (1975). Conducted within one orbital cycle, they showed unusual variability of physical parameters within the phases (0.70-0.90) P close to the 0.855 P phase of the magnetic field pole close to the gainer. Fig. 6 shows a much lower velocity of the moving plasma than the first parabolic velocity in all five helium lines arising from metastable levels. This clearly indicates nonstationarity of the outflow of matter and the variable flow density in the direction of the dipole axis of the magnetic field. The behavior of radial velocities in phases (0.8-0.9) P in the shell lines Na I $\lambda\lambda$ 5889, 5895 is also particularly important. During 0.1 P, the moving plasma slows down, stops at a certain point, and accelerates again, stating the fact of actual variations in the sign of this movement. Thus, the study of observations of Flora & Hack (1975) also confirmed that the observer, looking perpendicular to the surface of the donor along the axis of the magnetic field, reveals the region of the donor surface that is responsible for the location of the pole of the magnetic field facing the gainer and the loss of matter directly from the donor surface in phase 0.855 P with its subsequent transfer to the gainer.

However, the fact of localization of the poles of the magnetic field on the surface of the donor, reflected in many studies, needs some clarification, based on the spatial location of its magnetic axis. Let us turn to the model of the donor as a magnetic rotator, by analogy to the model of a helium star as an oblique magnetic rotator presented by Shore & Brown (1990). This model (see Fig. 8 in Skulskyy (2020b)) may be quite illustrative since the dipole axis of its magnetic field is deviated by 28° relative to the orbital plane of the binary

system (Skulskij, 1985). The center of the donor magnetic dipole is displaced by 0.08 of the distance between the centers of gravity of both components toward the gainer's center. It is also clear that the magnetic pole, located on the surface of the donor and observed in phases of about 0.855 P, is more effective in terms of the amount of transferred matter to the gainer, which is confirmed by all studies. The ionized gas, directed by the magnetic field of the donor in the direction of its dipole axis from the surface of the donor, is deflected along the lines of the magnetic field primarily to the accretion disk. However, a certain amount of charged particles will move along the lines of force of the magnetic field in the direction to the second pole of the magnetic field on the surface of the donor, heating its surface. And, if in the first quadrature in the phases around 0.355 P the magnetic pole on the surface of the donor is located above the plane of the orbit, then in the phases around 0.855 P the magnetic pole on the surface of the donor is below the plane of the orbit, or vice versa. The detection of these poles also depends on the inclination of the plane of the orbit. Not everything is clear in this part because the inclination of the orbit in current research is taken from i = 81° in Mennickent & Djurašević (2013) to i = 93.5° in Mourard et al. (2018). This is close to the binary orbital inclination i = 90°, and regardless of whether the pole of the magnetic field is in the upper or lower hemisphere on the donor surface, the observer, due to the projection of the rounded shape of the surface on the line of sight, must register certain deviations of the surface heating maximum from the 0.355 P phase. This is confirmed by the absolute spectrophotometry of Burnashev & Skulskij (1991) of 1974-1985. They showed that the observer starts to register the excess radiation (a hot spot on the donor surface) only from the 0.355 P phase directed along the axis of the magnetic field (see Figure 1 in Skulskyy (2020b)). The excess of this radiation disappears near the 0.50 P phase, demonstrating during the orbital phases (0.37-0.49) P the rapid variability of the absolute radiation flux in the H_α emission line and the continuum around this line (see Skulskyy, 2020b; Alexeev & Skulskij, 1989). The maximum of the excess of this radiation is really shifted from the 0.355 P phase and corresponds to the phases (0.43-0.47) P. Thus, in these phases, some surface heating on the donor surface may be formed due to nonstationary shock collisions of ionized gas, directed along the magnetic field lines to the magnetic field pole, the location of which is given by the spatial configuration of the magnetic field dipole. The phase range (0.43-0.47) P corresponds to the known minimum on the polarization curves for Beta Lyrae studied by Appenzeller & Hiltner (1967) and Lomax et al. (2012), which is interpreted as formed by collisions of gas flows with the accretion disk during the scattering of radiation by free electrons. This encourages the research of the reflection of the spatial configuration of the donor's magnetic field in the polarization observations.

References

Ak, H., Chadima, P., Harmanec, P., et al., New findings supporting the presence of a thick disc and bipolar jets in the β Lyrae system. 2007, *Astronomy and Astrophysics*, **463**, 233, DOI: 10.1051/0004-6361:20065536

Alduseva, V. Y. & Esipov, V. F., The line He I λ 10830 in β Lyr shell. 1969, *Astronomicheskii Zhurnal*, **46**, 113

Alexeev, G. N. & Skulskij, M. Y., Rapid variability of the spectrum of β Lyrae in the H_α region. 1989, *Bull. Spec. Astroph. Obs.*, **28**, 21

Appenzeller, I. & Hiltner, W. A., True polarization curves for Beta Lyrae. 1967, *Astrophysical Journal*, **149**, 353, DOI: 10.1086/149258

Bisikalo, D. V., Harmanec, P., Boyarchuk, A. A., Kuznetsov, O. A., & Hadrava, P., Circumstellar structures in the eclipsing binary β Lyr A. Gasdynamical modelling confronted with observations. 2000, *Astronomy and Astrophysics*, **353**, 1009

Burnashev, V. I. & Skulskij, M. Y., Absolute spectrophotometry of β Lyr. 1978, *Izv. Krymskoj Astrofiz. Obs.*, **58**, 64

Burnashev, V. I. & Skulskij, M. Y., H_α photometry and magnetic field of β lyrae. 1991, *Izv. Krymskoj Astrofiz. Obs.*, **83**, 108

Flora, U. & Hack, M., Spectrographic observations of β Lyr during the international campaign of 1971. 1975, *Astronomy and Astrophysics, Supplement*, **19**, 57

Girnyak, M. B., Skulskij, M. Y., Shanin, G. I., & Shcherbakov, A. G., The investigation of the emission line of He I λ 10830 Å in the spectrum of Beta Lyrae. 1978, *Izv. Krymskoj Astrofiz. Obs.*, **58**, 75

Harmanec, P. & Scholz, G., Orbital elements of β Lyrae after the first 100 years of investigation. 1993, *Astronomy and Astrophysics*, **279**, 131

Hoffman, J. L., Nordsieck, K. H., & Fox, G. K., Spectropolarimetric evidence for a bipolar flow in Beta Lyrae. 1998, *Astronomical Journal*, **115**, 1576, DOI: 10.1086/300274

Lomax, J. R., Hoffman, J. L., Elias, Nicholas M., I., Bastien, F. A., & Holenstein, B. D., Geometrical constraints on the hot spot in Beta Lyrae. 2012, *Astrophysical Journal*, **750**, 59, DOI: 10.1088/0004-637X/750/1/59

Mennickent, R. E. & Djurašević, G., On the accretion disc and evolutionary stage of β Lyrae. 2013, *Monthly Notices of the RAS*, **432**, 799, DOI: 10.1093/mnras/stt515

Morgan, T. H., Potter, A. E., & Kondo, Y., Complex infrared emission features in the spectrum of Beta Lyrae. 1974, *Astrophysical Journal*, **190**, 349, DOI: 10.1086/152883

Mourard, D., Brož, M., Nemravová, J. A., et al., Physical properties of β Lyrae A and its opaque accretion disk. 2018, *Astronomy and Astrophysics*, **618**, A112, DOI: 10.1051/0004-6361/201832952

Rucinski, S. M., Pigulski, A., Popowicz, A., et al., Light-curve instabilities of β Lyrae observed by the BRITE satellites. 2018, *Astronomical Journal*, **156**, 12, DOI: 10.3847/1538-3881/aac38b

Sahade, J., Huang, S. S., Struve, O., & Zebergs, V., The spectrum of Beta Lyrae. 1959, *Transactions of the American Philosophical Society*, **49**, 1

Shore, S. N. & Brown, D. N., Magnetically controlled circumstellar matter in the helium-strong stars. 1990, *Astrophysical Journal*, **365**, 665, DOI: 10.1086/169520

Skulskij, M. Y., Quantitative analysis of the spectrum of Beta Lyrae IV. Line identifications for the faint component and the mass of both stars. 1975, *Astronomicheskii Zhurnal*, **52**, 710

Skulskij, M. Y., The magnetic field of the Beta-Lyrae system. 1985, *Sov. Astron. Lett.*, **11**, 21

Skulskij, M. Y., Study of β Lyrae CCD spectra. Absorbtion lines, orbital elements and disk structure of the gainer. 1992, *Sov. Astron. Lett.*, **18**, 287

Skulskij, M. Y., Spectra of β Lyr. Matter transfer and circumstellar structures in presence of the donors magnetic field. 1993a, *Astron. Lett.*, **19**, 45

Skulskij, M. Y., Study of β Lyrae spectra - the Si II $\lambda\lambda$ 6347, 6371 doublet and the discovery of the cyclic variability of equivalent widths of lines of the loser's "magnetized" atmosphere. 1993b, *Astron. Lett.*, **19**, 19

Skulskij, M. Y., The spectrum of β Lyrae: the SiII $\lambda\lambda$ 6347, 6371 doublet in 1992 and its variation from season to season. 1993c, *Astron. Lett.*, **19**, 160

Skulskij, M. Y. & Plachinda, S. I., A study of the magnetic field of the bright component of β Lyr in the SiII $\lambda\lambda$ 6347, 6371 lines. 1993, *Pisma Astron. Zh.*, **19**, 517

Skulsky, M. Y. & Kos, E. S., On the dynamics of circumstellar gaseous structures and magnetic field of β Lyrae. 2011, in *Magnetic Stars. Proceedings of the International Conference, held in the Special Astrophysical Observatory of the Russian AS, August 27- September 1, 2010*, ed. I. Romanyuk & D. Kudryavtsev, 259–263

Skulskyy, M. Y., Formation of magnetized spatial structures in the Beta Lyrae system. I. Observation as a research background of this phenomenon. 2020a, *Contrib. Astron. Obs. Skalnaté Pleso*, **50**, 681, DOI: 10.31577/caosp.2020.50.3.681

Skulskyy, M. Y., Formation of magnetized spatial structures in the Beta Lyrae system. II. Observation as a research background of this phenomenon. 2020b, *Contrib. Astron. Obs. Skalnaté Pleso*, **50**, 717, DOI: 10.31577/caosp.2020.50.4.717

Struve, O., The Spectrum of β Lyrae. 1941, *Astrophysical Journal*, **93**, 104, DOI: 10.1086/144249

Umana, G., Maxted, P. F. L., Trigilio, C., et al., Resolving the radio nebula around Beta Lyrae. 2000, *Astronomy and Astrophysics*, **358**, 229

Zeilik, M., Heckert, P., Henson, G., & Smith, P., Infrared photometry of Beta Lyrae: 1977-1982. 1982, *Astronomical Journal*, **87**, 1304, DOI: 10.1086/113217

The GATE summer school

M. Skarka[1,2], J. Janík[2], E. Paunzen[2] and V. Glos[2]

[1] *Astronomical Institute of the Czech Academy of Sciences, Fričova 298, CZ-251 65 Ondřejov, Czech Republic (E-mail: skarka@asu.cas.cz)*

[2] *Department of Theoretical Physics and Astrophycis, Masaryk University, Kotlářská 2, CZ-611 37 Brno, Czech Republic*

Abstract. The education activities in the form of short and condensed courses such as summer schools are essential parts of the educational process of every scientist. Here we briefly describe the program and the organization of the GATE summer school that was held in a form of virtual meeting between August 8 and 15 in Brno, Czech Republic.

Key words: GATE summer school – General: editorial – Methods: data analysis

1. Introduction

In the time of large sky surveys and projects producing large amount of data, it is very important to know where to find the archived and freely available data, how to work with them and what tools and pipelines to use to work efficiently. However, without the knowledge of the physics underlying the studied phenomena, working with the data would be useless. The two recent most important satellites regarding the stellar astrophysics are *GAIA* (Gaia Collaboration et al., 2018) and *TESS* (Ricker et al., 2014). Our motivation to organize a summer school dedicated to these two missions was to provide the students with knowledge about the usage of the data produced by these satellites in a short time of the summer school.

We named the school *"GAIA & TESS: Tools for understanding the Local Universe"*, shortly *GATE summer school*[1]. It was foreseen as the second summer school under the ERASMUS+ project titled *"Per Aspera ad Astra Simul"* that secures mobility of students, teachers and researchers among institutes in the Czech Republic, Slovak Republic, and Canarias, Spain (Kabáth et al., 2019). The first summer school was organized in cooperation with the OPTICON consortium and was held in Stará Lesná in Slovak Republic at the AI SAV between 17 and 27 July, 2019 (Kabáth et al., 2019).

---

[1] https://gate.physics.muni.cz/

2. The organization of the school

The GATE summer school was organized by the Department of Theoretical Physics and Astrophysics, Masaryk university in Brno, Czech Republic (the main organizer) in cooperation with the Astronomical institute, AS CAS, Ondřejov, Czech Republic. Originally, the school was proposed for 30 students across the world working on six different topics in groups comprising five students under supervision of experienced scientists. The original date of the school (June 2020) had to be postponed to August due to the COVID-19 pandemic. This postponement resulted in the reduction to four projects due to the unavailability of tutors. In addition, 14 days before the start of the school, we were forced to go in a fully online regime because the in-person format was impossible to manage.

During July 2020, 20 students[2] from seven different countries were selected to participate on the school in the new dates of August 8 to 15. Finally, only 17 students of BSc to PhD stages were able to participate on the school. About 40 hours were dedicated to the work on four projects from the stellar astrophysics: Exoplanets (lead by Hannu Parviainen, IAC Tenerife, Spain), Stellar pulsations (lead by Paul Beck, University of Graz, Austria), Eclipsing binaries (lead by Kyle Conroy, Villanova University, United States) and Stellar flares (lead by Krisztian Vida, Konkoly Observatory, Hungary). The rest of the time was filled with lectures about the *TESS* and *GAIA* missions, as well as about *Kepler* (Borucki et al., 2010) and *BRITE* satellites (Weiss et al., 2014). There were also two hands-on sessions on *TESS* and *GAIA* data and a career session.

All the communication and lectures were online using Zoom and Slack. After the initial get in use, these tools appeared to be very efficient and easy to use. The lectures were recorded and are available at Youtube.com[3], the presentations are posted at the web page of the summer school. Despite the unpleasant situation, we managed to meet online at the conference party and have two hours of fun. The participants including the tutors are in Fig. 1.

3. The projects

The projects and the results are described in this CAOSP issue. Briefly, the exoplanet group revised the parameters of four transiting hot Jupiter planets by using `PyTransit` software (Parviainen, 2015) on the *TESS* data (Gajdoš et al., 2021). The binary group tested the robustness and accuracy of parameters using the soon to be released `PHOEBE 2.3` EB modeling package (Conroy et al., 2020) on the TESS data of AI Phe (Korth et al., 2021). Project on stellar flares was focused on search for flare stars in 136 open clusters by using *TESS* light curves and utilizing *GAIA* data (Maryeva et al., 2021). Finally, the asteroseismic group

---

[2]from 51 registered applicants

[3]`https://www.youtube.com/channel/UCHk-EY_tFtGKotKn9xt3PeA`

Figure 1. The conference photo of all participants of the GATE summer school including the main organizer and tutors.

worked on the global asteroseismic analysis of a heart-beat star KIC 5006817 based on the full *Kepler* data sample and *TESS* data (Merc et al., 2021).

4. Summary

We briefly summarized the GATE summer school devoted to *TESS* and *GAIA* missions held in August 8-15 in Brno, Czech Republic. The school was held in fully online regime. The students attended six lectures focused on the space missions, two hands-on sessions focused on *TESS* and *GAIA* data, one career session, and participated on an online version of a conference party. The lectures are available online on the web page of the summer school and on Youtube.com. Overall, the students, tutors and lecturers did a great job. The results of the students projects are summarized in (Gajdoš et al., 2021; Maryeva et al., 2021; Korth et al., 2021; Merc et al., 2021, this proceedings).

References

Borucki, W. J., Koch, D., Basri, G., et al., Kepler Planet-Detection Mission: Introduction and First Results. 2010, *Science*, **327**, 977, DOI: 10.1126/science.1185402

Conroy, K. E., Kochoska, A., Hey, D., et al., Physics of Eclipsing Binaries. V. General Framework for Solving the Inverse Problem. 2020, *Astrophysical Journal, Supplement*, **250**, 34, DOI: 10.3847/1538-4365/abb4e2

Gaia Collaboration, Brown, A. G. A., Vallenari, A., et al., Gaia Data Release 2. Summary of the contents and survey properties. 2018, *Astronomy and Astrophysics*, **616**, A1, DOI: 10.1051/0004-6361/201833051

Gajdoš, P., Maliuk, A., Vítková, M., & Parviainen, H., Improving light curve parameters of exoplanets based on TESS data. 2021, *Contrib. Astron. Obs. Skalnaté Pleso*, **51**, 68, DOI: 10.31577/caosp.2021.51.1.68

Kabáth, P., Korhonen, H., & Jones, D., Observational astrophysics: from proposals to publication. 2019, *Contributions of the Astronomical Observatory Skalnate Pleso*, **49**, 522

Korth, J., Moharana, A., Pešta, M., Czavalinga, D. R., & Conroy, K. E., Consequences of parameterization choice on eclipsing binary light curve solutions. 2021, *Contrib. Astron. Obs. Skalnaté Pleso*, **51**, 58, DOI: 10.31577/caosp.2021.51.1.58

Maryeva, O., Bicz, K., Caiyun, X., et al., Flare stars in nearby Galactic open clusters based on TESS data. 2021, *Contrib. Astron. Obs. Skalnaté Pleso*, **51**, 78, DOI: 10.31577/caosp.2021.51.1.78

Merc, J., Kalup, C., Rathour, R., Sánchez Arias, J., & Beck, P., Asteroseismology of the heartbeat star KIC 5006817. 2021, *Contrib. Astron. Obs. Skalnaté Pleso*, **51**, 45, DOI: 10.31577/caosp.2021.51.1.45

Parviainen, H., PYTRANSIT: fast and easy exoplanet transit modelling in PYTHON. 2015, *Monthly Notices of the RAS*, **450**, 3233, DOI: 10.1093/mnras/stv894

Ricker, G. R., Winn, J. N., Vanderspek, R., et al., Transiting Exoplanet Survey Satellite (TESS). 2014, in Society of Photo-Optical Instrumentation Engineers (SPIE) Conference Series, Vol. **9143**, *Space Telescopes and Instrumentation 2014: Optical, Infrared, and Millimeter Wave*, ed. J. Oschmann, Jacobus M., M. Clampin, G. G. Fazio, & H. A. MacEwen, 914320

Weiss, W. W., Rucinski, S. M., Moffat, A. F. J., et al., BRITE-Constellation: Nanosatellites for Precision Photometry of Bright Stars. 2014, *Publications of the ASP*, **126**, 573, DOI: 10.1086/677236

Asteroseismology of the heartbeat star KIC 5006817

J. Merc[1,2]**, Cs. Kalup**[3,4]**, R.S. Rathour**[5]**, J.P. Sánchez Arias**[6] **and P.G. Beck**[7,8]

[1] *Astronomical Institute, Faculty of Mathematics and Physics, Charles University, V Holešovičkách 2, 180 00 Prague, Czech Republic (E-mail: jaroslav.merc@student.upjs.sk)*

[2] *Institute of Physics, Faculty of Science, P.J. Šafárik University, Park Angelinum 9, 040 01 Košice, Slovak Republic*

[3] *Konkoly Observatory, Research Centre for Astronomy and Earth Sciences, Konkoly Thege 15-17, H-1121 Budapest, Hungary*

[4] *Department of Astronomy, Eötvös University, Pázmány Péter sétány 1/A, H-1171 Budapest, Hungary*

[5] *Nicolaus Copernicus Astronomical Centre, Polish Academy of Sciences, Bartycka 18, 00-716 Warszawa, Poland*

[6] *Astronomical Institute, Academy of Sciences of Czech Republic, Fričova 298, 251 65 Ondřejov, Czech Republic*

[7] *Institut für Physik, Universität Graz, NAWI Graz, Universitätsplatz 5/II, 8010 Graz, Austria*

[8] *Instituto de Astrofsica de Canarias, La Laguna, Tenerife, Spain*

Abstract. This paper summarizes the project work on asteroseismology at the ERASMUS+ GATE 2020 Summer school[1] on space satellite data. The aim was to do a global asteroseismic analysis of KIC 5006817, and quantify its stellar properties using the high-quality, state of the art space missions data. We employed the aperture photometry to analyze the data from the *Kepler* space telescope and the *Transiting Exoplanet Survey Satellite (TESS)*. Using the `lightkurve` Python package, we have derived the asteroseismic parameters and calculated the stellar parameters using the scaling relations. Our analysis of KIC 5006817 confirmed its classification as a heartbeat binary. The rich oscillation spectrum facilitate estimating power excess ($\nu_{\max}$) at 145.50±0.50 μHz and large frequency separation ($\Delta\nu$) to be 11.63±0.10 μHz. Our results showed that the primary component is a low-luminosity, red-giant branch star with a mass, radius, surface gravity and luminosity of 1.53±0.07 M$_\odot$, 5.91±0.12 R$_\odot$, 3.08±0.01 dex, and 19.66±0.73 L$_\odot$, respectively. The orbital period of the system is 94.83±0.05 d.

Key words: asteroseismology – stars: individual: KIC 5006817 – binaries: general

---

[1] *'GAIA & TESS: Tools for understanding the local Universe'*, 2020, August 7-16, Masaryk University, Brno, Czech Republic, `https://gate.physics.muni.cz/`

1. Introduction

Stellar masses and radii are the most fundamental parameters to describe a star. However, the mass and the radius of a star are difficult parameters to infer and are often found to have large uncertainties (for a recent review see, e.g. Serenelli et al., 2020, and references therein). Asteroseismology, the study of stellar oscillations, is a powerful technique to determine masses and radii with high accuracy as well as constrain the internal structure of a star (for a recent review see, e.g. Aerts, 2019, and references therein). A new generation of space telescopes, dedicated to obtaining photometric time series, unprecedented in photometric quality and time base, such as the NASA *Kepler* space telescope (Borucki et al., 2010), has lead to the dawn of a golden age of asteroseismology.

Such space photometric data provided the fuel for tremendous advances, particularly for the seismic investigation of stars in the advanced stellar evolution phases. Due to their extended outer convective envelopes, red-giant stars oscillate with convectively driven solar-like oscillations. Oscillation modes are classified by their restoring force. These stochastic oscillations are mainly high order pressure-modes, leading to a very regular, comb-like pattern in the frequency domain, well explained through theory (Tassoul, 1980). The identification and quantitative description of the patterns that these modes print in the periodogram allow to determine the fundamental parameters of red-giant stars through the scaling relations (Kjeldsen & Bedding, 1995; Kallinger et al., 2010). Seismically inferred masses and radii have been tested though comparison with dynamical masses of eclipsing binaries, hosting oscillating red-giant primary components (Frandsen et al., 2013). Following this approach, Gaulme et al. (2016) suggested an offset between seismic and dynamical masses of 15%.

Furthermore, such data led to the discovery of mixed-dipole modes (Beck et al., 2011; Bedding et al., 2011; Mosser et al., 2011), being not purely pressure modes that probe the outer convective envelope, but also couple with gravity modes probing the dense central regions of the star. With this echo from the core, it was possible to constrain the density and rotational gradient between the stellar surface and the core (Beck et al., 2012; Bedding et al., 2011). In the meantime, more than 30 000 oscillating red giants have been seismically investigated from *Kepler* photometry (Yu et al., 2018) and numerous sophisticated methods have been developed to exploit the complex frequency pattern of mixed modes (Mosser et al., 2015; Vrard et al., 2016; Buysschaert et al., 2016). Due to the giant's immense intrinsic luminosity and the unparalleled photometric quality of the data, asteroseismology even allows us probing stars in the galactic halo (Mathur et al., 2016).

The NASA *Kepler* spacecraft data also lead to the unexpected discovery of a new class of binary systems that show tidally induced flux modulations (Welsh et al., 2011; Thompson et al., 2012). These objects, first theorized by Kumar et al. (1995), are eccentric detached binary systems that leave a distinctive feature in their light curves, caused by large hydrostatic adjustment due to the

strong gravitational distortion they experience during the periastron passage (e.g. Remus et al., 2012). These stars are colloquially referred to as *heartbeat* stars.

In this article, we present an asteroseismic analysis of the non-eclipsing heartbeat star KIC 5006817. Beck et al. (2014) previously studied this system from fourteen quarters of *Kepler* data covering about 1 300 days. They found a mass of the primary component of $1.49 \pm 0.06 \, \mathrm{M}_\odot$, and an orbital period of 94.81 days. The extensive monitoring of the radial-velocity variations with the HERMES spectrograph (Raskin et al., 2011), mounted to the 1.2m MERCATOR telescope on La Palma, Canary Islands, confirmed the binary nature of KIC 5006817 and allowed them to constrain the system's eccentricity to be $e = 0.7$. Here, we repeat the analysis from the full and final dataset of the nominal *Kepler* mission, covering more than 1 500 days (17 quarters). We also analyze this system's latest data, obtained by the NASA *TESS* mission (Ricker et al., 2015).

2. Data and reduction

2.1. *Kepler*

With its 0.95 m telescope, the NASA *Kepler* spacecraft (Borucki et al., 2010) provided ~ 4 years of continuous observation with a resolution of 4 arcsec/pixel (field of view of 105 deg^2) in both long-cadence (30 min) and short-cadence (1 min) mode. Because the spacecraft had to be rotated in order to point the solar panels towards the Sun, the time series was split into 90-day-long segments, referred to as Quarters (Q). Our target KIC 5006817 was observed in all quarters (Q1 - Q17) and the commissioning phase Q0 in the long-cadence mode. We have therefore employed all available data in the analysis.

We have used the `lightkurve`[2] Python package (Lightkurve Collaboration et al., 2018; Dotson et al., 2019) to process the target pixel data of the downloaded data stamps (see Fig. 1). To extract the source's flux from the target pixel files, we employed the aperture photometry. The optimal aperture was defined using a threshold feature in the package. For the present analysis, we adopted the threshold to be 25 times the median flux level to minimize the flux coming from the field stars and the background. This criterion was applied for the data extraction from all individual *Kepler* quarters.

The package allowed us to remove the background signal from the light curve of the target. We have constructed a background model by selecting pixels that did not contain the target itself, any nearby bright sources, and potentially saturated pixels. Subsequently, the light curve went through a procedure of outliers removal, flattening, and normalization in each quarter individually. Finally, we stacked all the individual light curves to get the final one (Fig. 1).

---

[2] https://github.com/KeplerGO/lightkurve
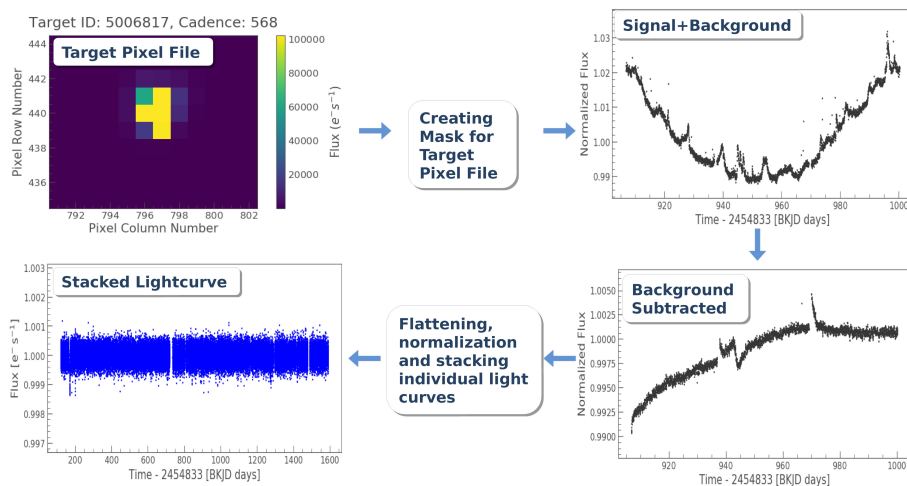
Figure 1. Analysis procedure for *Kepler* data. Top left panel shows target pixel file for *Kepler* Quarter 10. The top right panel shows the raw light curve with background and oscillation components. The bottom right panel shows the light curve after the background subtraction. The bottom left panel shows the full and final light curve, composed from the normalized light curves of the individual quarters.

There were several gaps of various length (minutes to days) in the data e.g., one missing long-cadence data point every ~ 3 days due to angular momentum dump, gaps of two days due to the data download window and successive reorientation of the satellite (every ~ 93 days), or other non-periodic instrumental problems, such as save-mode operation of the space craft. These regular gaps in the time domain lead to a complex alias-frequency pattern in the Fourier space (see e.g. García et al., 2014). To improve the spectral window, we filled the short-term gaps (few datapoints) in the data using the linear interpolation or by the Gaussian noise. Both methods gave us very similar results. This time-series data were used to obtain the periodogram to estimate asteroseismic parameters (Sect. 4).

2.2. Transiting Exoplanet Survey Satellite (*TESS*)

NASA *TESS* mission satellite (Ricker et al., 2015) hosts four refractor telescopes with an aperture of $0.1\,\mathrm{m}$, leading to a resolution of 21 arcseconds/pixel with a combined field of view of 2304 deg^2, with two observing modes. The full field of view is co-added on board the spacecraft to full-frame images, integrated for 30 minutes. For pre-selected targets, pixel stamps around the star are stored with a 2 min short-cadence. Our target has been observed only in the long-cadence
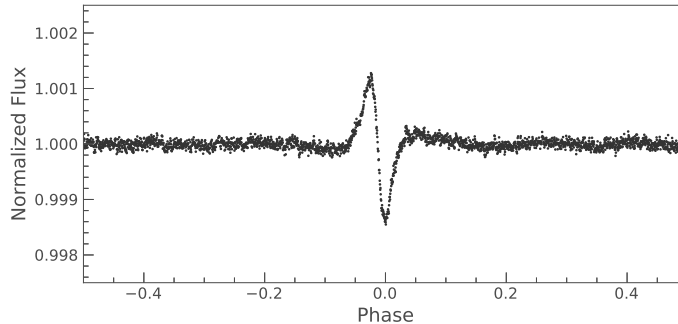
Figure 2. *Kepler* light curve of KIC 5006817 phased with the period of 94.83 d. The heartbeat feature caused by the gravitational distortion of the primary during the periastron passage is well visible.

mode for one *TESS* Sector 14, covering 27.5 days. We should note that the pixel scale of *TESS* is significantly larger than that of *Kepler*, resulting in the strong contamination of the light curve. Moreover, in the case of *TESS*, the source flux is significantly affected by the stray light from the Moon and the Earth.

The reduction procedure applied to *TESS* data was similar to *Kepler* data, discussed in the previous section. However, in addition to aperture photometry, we have employed an alternative approach to cope with the complicated background variations and contamination, using the algorithms implemented by András Pál with various tasks of the `FITSH` package (Pál, 2012). As we will discuss in Sect. 4.2, the target is too faint for a significant detection of the asteroseismic signal with *TESS*.

3. Binary analysis

KIC 5006817 is an eccentric binary system. Therefore, we have aimed to obtain the orbital period of the system using available photometric data. We have used the *Kepler* light curve, as the *TESS* data covers only short time interval of 27.5 days. For this task, the extracted *Kepler* light curve was flattened using an in-built function of the `lightkurve` package employing the Savitzky-Golay filter (Savitzky & Golay, 1964), in order to remove the long-term trends in the data. The size of the flattening window was set to ~ 17 days. Using this approach, we were able to preserve the heartbeat feature in the light curve, which was important for the following period analysis. We have used the Lomb-Scargle periodogram to obtain the periodogram and identify the system's orbital period to be 94.83±0.05 d. The phase-folded light curve with this period is shown in Fig. 2, the heartbeat feature is well visible. Our value of the orbital period is in

good agreement with the work of Beck et al. (2014), who obtained the value of 94.812±0.002 d.

4. Seismic analysis

4.1. *Kepler*

For the frequency analysis, we have used the light curves flattened with the size of the flattening window decreased to ~ 2 days in order to remove the heartbeat feature. This filter width is small enough to remove the tidally induced flux modulation, but preserves the oscillation signal whose average period is on the order of 1.5 hours. The individual light curves from all available quarters were then stacked together to produce the final dataset (see Sect. 2). The power spectral density (shown in Fig. 3) was calculated using the Lomb-Scargle method using a built-in function in the `lightkurve` package. To obtain the peak frequency of the excess of oscillation power $\nu_{\max}$, we have fitted the resulting periodogram by Gaussian envelope together with the power-law component to account for rotation and granulation and constant offset for the photon-noise background. To obtain the large frequency separation $\Delta\nu$, we divided the power spectral density by multi-component background model to normalize it and used the autocorrelation method (see e.g. Mosser & Appourchaux, 2009). Our resulting values are $\nu_{\max} = 145.50 \pm 0.50\,\mu\text{Hz}$ and $\Delta\nu = 11.63 \pm 0.10\,\mu\text{Hz}$. We assume similar uncertainties of the seismic parameters as Kallinger et al. (2018), as no uncertainties have been estimated using the methods presented above.

The asteroseismic parameters obtained above are connected with the astrophysical parameters of the star. The power excess $\nu_{\max}$ is proportional to the surface acceleration ($\log g$), while the large frequency separation $\Delta\nu$ is corresponding to the speed of sound and hence the mean density of the star. The mass and radius of the star are calculated using the following scaling relations (Kjeldsen & Bedding, 1995; Kallinger et al., 2010):

$$\frac{R_*}{R_\odot} = \frac{\nu_{\max}}{\nu_{\max}^\odot} \times \left(\frac{\Delta\nu}{\Delta\nu_\odot}\right)^{-2} \times \sqrt{\frac{T_{\text{eff}}}{T_{\text{eff}}^\odot}} \tag{1}$$

$$\frac{M_*}{M_\odot} = \left(\frac{R_*}{R_\odot}\right)^3 \times \left(\frac{\Delta\nu}{\Delta\nu_\odot}\right)^2 \tag{2}$$

$$\frac{L_*}{L_\odot} = \left(\frac{\nu_{\max}}{\nu_{\max}^\odot}\right)^2 \times \left(\frac{\Delta\nu}{\Delta\nu_\odot}\right)^{-4} \times \left(\frac{T_{\text{eff}}}{T_{\text{eff}}^\odot}\right)^5 \tag{3}$$

where R_*, M_*, and L_* are radius, mass, and luminosity of the studied star, respectively. For the calculation, we have adopted the $T_{\text{eff}} = 5000\,\text{K}$ obtained using the high-resolution spectroscopy by Beck et al. (2014). The solar values
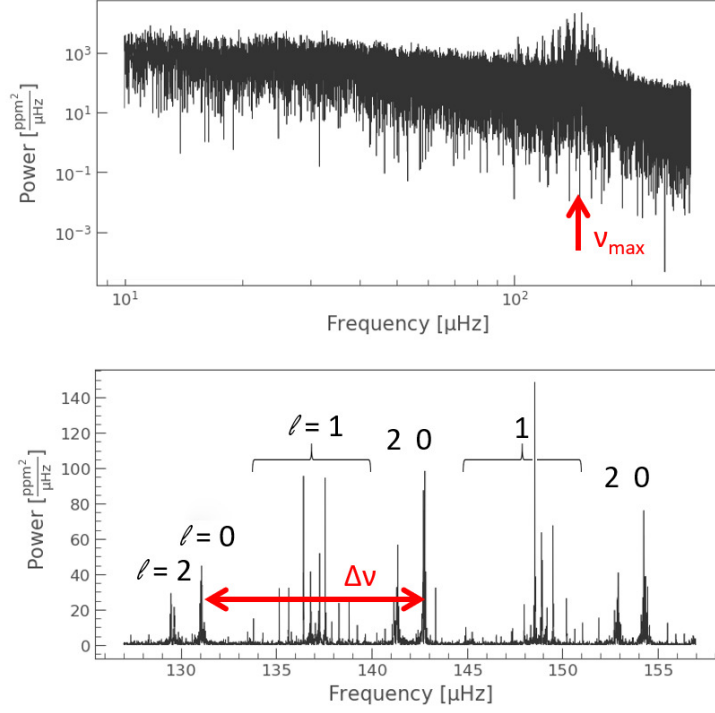
Figure 3. Asteroseismic parameters of KIC 5006817. The upper panel shows the Power Spectral Density of the *Kepler* light curve of KIC 5006817. The position of the peak frequency of the power excess $\nu_{\max}$ is shown by the red arrow. The lower panel shows a zoom into the power excess. A large frequency separation $\Delta\nu$ is shown by the red arrow. The spherical degree of the excited modes is indicated by ℓ.

are from Huber et al. (2011) and Prša et al. (2016). The obtained parameters are as follows: $\log g = 3.08 \pm 0.01$, $R_* = 5.91 \pm 0.12\,R_\odot$, $M_* = 1.53 \pm 0.07\,M_\odot$, $L_* = 19.66 \pm 0.73\,L_\odot$.

4.2. *TESS*

We have intended to repeat the same analysis as described in the previous section, also for data from the *TESS* satellite. The target was observed in a single sector with a 30 min cadence. We have extracted the light curve from the full-frame images using two independent methods, the aperture photometry and the differential image analysis (see Sect. 2.2). The signal to noise ratio of
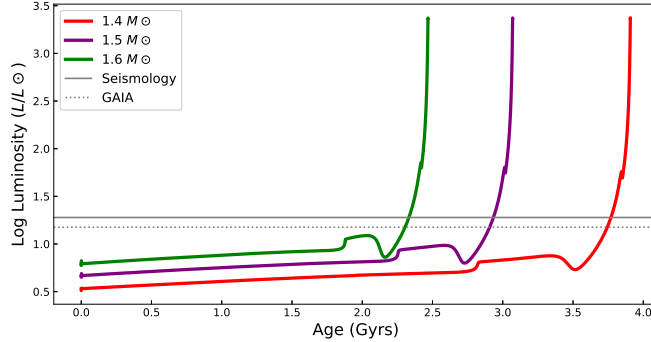
Figure 4. Luminosity-age diagram showing `MESA` evolutionary tracks of 1.4 (red), 1.5 (purple) and 1.6 $M_\odot$ (green) with solar composition. The asteroseismology and *Gaia* estimated luminosity marked by solid and dotted lines, respectively, are the adopted limits to estimate the age of KIC 5006817.

both resulting periodograms did not allow to reliably detect the oscillations and, therefore, to obtain the astrophysical parameters of the star. The target seems to be too faint (*V*-band magnitude 11.15±0.08; Hog et al., 2000) for this kind of analysis using the data obtained in 30 min cadence in a single sector. The first results on asteroseismology of the red giants using single *TESS* sectors by Aguirre et al. (2020) reported high signal-to-noise detections of the power excess of giants between 6th and 8th visual magnitude. For stars in the continuous viewing zone (Mackereth et al., 2020), this limit is lower due to the increased time base of one year.

5. Age of KIC 5006817

Based on the seismically determined mass, we calculated a grid of simple stellar evolutionary tracks, using the `MESA` code (*Modules for Experiments in Stellar Astrophysics*,Paxton et al., 2019, and references therein). The grid was computed for solar metallicity and stellar masses between 1.4, 1.5 and 1.6 $M_\odot$, which roughly corresponds to the one-sigma range of the mass uncertainty. The initial metal fraction composition and opacity profiles are used as per Asplund et al. (2009) prescription.

As it can be seen from Fig. 4, the red-giant primary of the system belongs to the low-luminosity red-giant stars and falls between two interesting evolutionary stages. KIC 5006817 has already passed the first dredge-up phase, when the convective envelope reaches its maximum penetration into the stellar structure. It still has to pass the phase of the luminosity bump, when the hydrogen-burning shell hits the metallicity discontinuity, left behind from the convective envelope when it started to move outwards after the first dredge-up.

Table 1. Comparison of our asteroseismic values with the literature.

	This work	Beck et al. (2014)	Yu et al. (2018)	Gaulme et al. (2020)
$\nu_{\max}$ [μHz]	145.50±0.50	145.9±0.5	145.48±0.83	146.44±0.26
$\Delta\nu$ [μHz]	11.63±0.10	11.64±0.01	11.620±0.017	11.68±0.05
M_* [$M_\odot$]	1.53±0.07	1.49±0.06	1.47±0.07	1.39±0.05
R_* [$R_\odot$]	5.91±0.12	5.84±0.009	5.83±0.10	5.67±0.08
L_* [$L_\odot$]	19.66±0.73	19±3	16.87±0.61	15.96±0.51
$\log g$ [dex]	3.08±0.01	3.08	3.07±0.01	3.07±0.01

Table 2. Comparison of our astrophysical values with the non-seimic values in the literature, the Cannon (Ness et al., 2016), the *Gaia* DR2 (Gaia Collaboration et al., 2018), and the StarHorse catalog (Anders et al., 2019).

	This work	Cannon	*Gaia* DR2	StarHorse
M_* [$M_\odot$]	1.53±0.07	1.59±0.015	-	$1.15^{+0.19}_{-0.14}$
R_* [$R_\odot$]	5.91±0.12	-	$5.46^{+0.116}_{-0.133}$	-
L_* [$L_\odot$]	19.66±0.73	-	14.971±0.563	-
$\log g$ [dex]	3.08±0.01	2.96±0.007	-	$3.00^{+0.07}_{-0.05}$

As a rough estimate for the age of the red giant, we report the range of the instrumental age of MESA models, when the evolutionary track for a given mass equals the luminosity of 19.66 and 14.971 solar luminosities, found from asteroseismology (Sect. 4.1) as well as from *Gaia* measurements (Gaia Collaboration et al., 2018), respectively (see Fig. 4). The difference between these two loci on the red-giant branch is very small as the red-giant branch is a phase of fast evolution. This indicates that the age of the system is somewhere between ∼2.3 and ∼3.7 Gyrs, assuming a 1.6 and 1.4 solar-mass star. We note that this is just a rough estimate, as the age of the model depends on details of the model and the included physics. The relatively large range originates from the different periods, the star spends on the main sequence. The duration of quiescent hydrogen-core burning is highly mass dependent, as nicely illustrated in Fig. 4.

6. Discussion

KIC 5006817 has been studied by several authors in the recent decade. In Table 1, we have compared our asteroseismic values and the calculated astrophysical parameters of the target with the values from the literature. The first comprehensive study of the star was performed by Beck et al. (2014) based on *Kepler* Q0 - Q14 measurements. We also mention an analysis focused on the character-

ization of the solar-like oscillations and granulation in 16 094 oscillating red giants of Yu et al. (2018), and a recent paper by Gaulme et al. (2020), in which the authors analyzed the asteroseismic and rotational parameters of about 4 500 relatively bright red giants observed by *Kepler*. As shown in Table 1, our results show good agreement with the literature within the uncertainties.

We have also shown (in Table 2) the comparison of the astrophysical parameters of KIC 50068187 (mass, radius, luminosity, and $\log g$) obtained in this work, with the non-seismic values from the literature. The data from *Gaia* DR2 (Gaia Collaboration et al., 2018) are based on the *Gaia* broadband photometry and the measured parallax, while values in the StarHorse catalog (Queiroz et al., 2020) are based, in addition to *Gaia* measurements, also on the photometry from 2MASS and *WISE*. *The Cannon* catalog (Ness et al., 2016) is based on the probabilistic model of stellar spectra and the spectra from the APOGEE survey. These independent approaches are also consistent with our values from asteroseismology.

7. Conclusions

In this work, we performed an asteroseismic analysis of the *Kepler* and *TESS* light curves of the heartbeat star KIC 5006817. Reasonable asteroseismic parameters, $\nu_{\max}$ of the power excess, and the large frequency separation $\Delta\nu$, were obtained only from *Kepler* data, as the target seemed to be too faint for significant detection of oscillations using a single *TESS* sector data obtained in 30 min cadence. Using the scaling relations, we calculated the mass of 1.5 $M_\odot$, radius 5.9 $R_\odot$, surface gravity 3.08 dex, and luminosity 19.7 $L_\odot$ for the primary. Analysis of the MESA evolutionary paths calculated for various masses confirmed that the red giant in KIC 5006817 is an RGB star. The heartbeat feature detected in the *Kepler* light curve allowed us to obtain the orbital period of 94.8 days.

References

Aerts, C., Probing the interior physics of stars through asteroseismology. 2019, *arXiv e-prints*, arXiv:1912.12300

Aguirre, V. S., Stello, D., Stokholm, A., et al., Detection and Characterization of Oscillating Red Giants: First Results from the TESS Satellite. 2020, *Astrophysical Journal, Letters*, **889**, L34, DOI: 10.3847/2041-8213/ab6443

Anders, F., Khalatyan, A., Chiappini, C., et al., Photo-astrometric distances, extinctions, and astrophysical parameters for Gaia DR2 stars brighter than G = 18. 2019, *Astronomy and Astrophysics*, **628**, A94, DOI: 10.1051/0004-6361/201935765

Asplund, M., Grevesse, N., Sauval, A. J., & Scott, P., The chemical composition of the Sun. 2009, *Annual review of astronomy and astrophysics*, **47**

Beck, P. G., Bedding, T. R., Mosser, B., et al., Kepler Detected Gravity-Mode Period Spacings in a Red Giant Star. 2011, *Science*, **332**, 205, DOI: 10.1126/science.1201939

Beck, P. G., Hambleton, K., Vos, J., et al., Pulsating red giant stars in eccentric binary systems discovered from Kepler space-based photometry. A sample study and the analysis of KIC 5006817. 2014, *Astronomy and Astrophysics*, **564**, A36, DOI: 10.1051/0004-6361/201322477

Beck, P. G., Montalban, J., Kallinger, T., et al., Fast core rotation in red-giant stars as revealed by gravity-dominated mixed modes. 2012, *Nature*, **481**, 55, DOI: 10.1038/nature10612

Bedding, T. R., Mosser, B., Huber, D., et al., Gravity modes as a way to distinguish between hydrogen- and helium-burning red giant stars. 2011, *Nature*, **471**, 608, DOI: 10.1038/nature09935

Borucki, W. J., Koch, D., Basri, G., et al., Kepler Planet-Detection Mission: Introduction and First Results. 2010, *Science*, **327**, 977, DOI: 10.1126/science.1185402

Buysschaert, B., Beck, P. G., Corsaro, E., et al., Testing the asymptotic relation for period spacings from mixed modes of red giants observed with the Kepler mission. 2016, *Astronomy and Astrophysics*, **588**, A82, DOI: 10.1051/0004-6361/201527055

Dotson, J., Barentsen, G., Hedges, C. L., et al., Lightkurve v1. 0: Kepler, K2, and TESS time series analysis in Python. 2019, *AAS*, **233**, 445

Frandsen, S., Lehmann, H., Hekker, S., et al., KIC 8410637: a 408-day period eclipsing binary containing a pulsating giant star. 2013, *A&A*, **556**, A138, DOI: 10.1051/0004-6361/201321817

Gaia Collaboration, Brown, A. G. A., Vallenari, A., et al., Gaia Data Release 2. Summary of the contents and survey properties. 2018, *Astronomy and Astrophysics*, **616**, A1, DOI: 10.1051/0004-6361/201833051

García, R. A., Mathur, S., Pires, S., et al., Impact on asteroseismic analyses of regular gaps in Kepler data. 2014, *Astronomy and Astrophysics*, **568**, A10, DOI: 10.1051/0004-6361/201323326

Gaulme, P., Jackiewicz, J., Spada, F., et al., Active red giants: Close binaries versus single rapid rotators. 2020, *Astronomy and Astrophysics*, **639**, A63, DOI: 10.1051/0004-6361/202037781

Gaulme, P., McKeever, J., Jackiewicz, J., et al., Testing the Asteroseismic Scaling Relations for Red Giants with Eclipsing Binaries Observed by Kepler. 2016, *Astrophysical Journal*, **832**, 121, DOI: 10.3847/0004-637X/832/2/121

Hog, E., Fabricius, C., Makarov, V. V., et al. 2000, The Tycho-2 catalogue of the 2.5 million brightest stars, Tech. rep., NAVAL OBSERVATORY WASHINGTON DC

Huber, D., Bedding, T. R., Stello, D., et al., Testing Scaling Relations for Solar-like Oscillations from the Main Sequence to Red Giants Using Kepler Data. 2011, *Astrophysical Journal*, **743**, 143, DOI: 10.1088/0004-637X/743/2/143

Kallinger, T., Beck, P. G., Stello, D., & Garcia, R. A., Non-linear seismic scaling relations. 2018, *Astronomy and Astrophysics*, **616**, A104, DOI: 10.1051/0004-6361/201832831

Kallinger, T., Mosser, B., Hekker, S., et al., Asteroseismology of red giants from the first four months of Kepler data: Fundamental stellar parameters. 2010, *Astronomy and Astrophysics*, **522**, A1, DOI: 10.1051/0004-6361/201015263

Kjeldsen, H. & Bedding, T. R., Amplitudes of stellar oscillations: the implications for asteroseismology. 1995, *Astronomy and Astrophysics*, **293**, 87

Kumar, P., Ao, C. O., & Quataert, E. J., Tidal Excitation of Modes in Binary Systems with Applications to Binary Pulsars. 1995, *ApJ*, **449**, 294, DOI: 10.1086/176055

Lightkurve Collaboration, Cardoso, J. V. d. M., Hedges, C., et al. 2018, Lightkurve: Kepler and TESS time series analysis in Python, Astrophysics Source Code Library

Mackereth, J. T., Miglio, A., Elsworth, Y., et al. 2020, Prospects for Galactic and stellar astrophysics with asteroseismology of giant stars in the TESS Continuous Viewing Zones and beyond, submitted to MNRAS

Mathur, S., García, R. A., Huber, D., et al., Probing the Deep End of the Milky Way with Kepler: Asteroseismic Analysis of 854 Faint Red Giants Misclassified as Cool Dwarfs. 2016, *Astrophysical Journal*, **827**, 50, DOI: 10.3847/0004-637X/827/1/50

Mosser, B. & Appourchaux, T., On detecting the large separation in the autocorrelation of stellar oscillation times series. 2009, *Astronomy and Astrophysics*, **508**, 877, DOI: 10.1051/0004-6361/200912944

Mosser, B., Barban, C., Montalbán, J., et al., Mixed modes in red-giant stars observed with CoRoT. 2011, *Astronomy and Astrophysics*, **532**, A86, DOI: 10.1051/0004-6361/201116825

Mosser, B., Vrard, M., Belkacem, K., Deheuvels, S., & Goupil, M. J., Period spacings in red giants. I. Disentangling rotation and revealing core structure discontinuities. 2015, *Astronomy and Astrophysics*, **584**, A50, DOI: 10.1051/0004-6361/201527075

Ness, M., Hogg, D. W., Rix, H. W., et al., Spectroscopic Determination of Masses (and Implied Ages) for Red Giants. 2016, *Astrophysical Journal*, **823**, 114, DOI: 10.3847/0004-637X/823/2/114

Pál, A., FITSH–a software package for image processing. 2012, *Monthly Notices of the Royal Astronomical Society*, **421**, 1825

Paxton, B., Smolec, R., Schwab, J., et al., Modules for experiments in stellar astrophysics (MESA): Pulsating variable stars, rotation, convective boundaries, and energy conservation. 2019, *The Astrophysical Journal Supplement Series*, **243**, 10

Prša, A., Harmanec, P., Torres, G., et al., Nominal Values for Selected Solar and Planetary Quantities: IAU 2015 Resolution B3. 2016, *Astronomical Journal*, **152**, 41, DOI: 10.3847/0004-6256/152/2/41

Queiroz, A. B. A., Anders, F., Chiappini, C., et al., From the bulge to the outer disc: StarHorse stellar parameters, distances, and extinctions for stars in APOGEE DR16 and other spectroscopic surveys. 2020, *Astronomy and Astrophysics*, **638**, A76, DOI: 10.1051/0004-6361/201937364

Raskin, G., van Winckel, H., Hensberge, H., et al., HERMES: a high-resolution fibre-fed spectrograph for the Mercator telescope. 2011, *A&A*, **526**, A69, DOI: 10.1051/0004-6361/201015435

Remus, F., Mathis, S., & Zahn, J. P., The equilibrium tide in stars and giant planets. I. The coplanar case. 2012, *Astronomy and Astrophysics*, **544**, A132, DOI: 10.1051/0004-6361/201118160

Ricker, G. R., Winn, J. N., Vanderspek, R., et al., Transiting Exoplanet Survey Satellite (TESS). 2015, *Journal of Astronomical Telescopes, Instruments, and Systems*, **1**, 014003, DOI: 10.1117/1.JATIS.1.1.014003

Savitzky, A. & Golay, M. J., Smoothing and differentiation of data by simplified least squares procedures. 1964, *Analytical chemistry*, **36**, 1627

Serenelli, A., Weiss, A., Aerts, C., et al., Weighing stars from birth to death: mass determination methods across the HRD. 2020, *arXiv e-prints*, arXiv:2006.10868

Tassoul, M., Asymptotic approximations for stellar nonradial pulsations. 1980, *Astrophysical Journal, Supplement*, **43**, 469, DOI: 10.1086/190678

Thompson, S. E., Everett, M., Mullally, F., et al., A Class of Eccentric Binaries with Dynamic Tidal Distortions Discovered with Kepler. 2012, *Astrophysical Journal*, **753**, 86, DOI: 10.1088/0004-637X/753/1/86

Vrard, M., Mosser, B., & Samadi, R., Period spacings in red giants. II. Automated measurement. 2016, *Astronomy and Astrophysics*, **588**, A87, DOI: 10.1051/0004-6361/201527259

Welsh, W. F., Orosz, J. A., Aerts, C., et al., KOI-54: The Kepler Discovery of Tidally Excited Pulsations and Brightenings in a Highly Eccentric Binary. 2011, *Astrophysical Journal, Supplement*, **197**, 4, DOI: 10.1088/0067-0049/197/1/4

Yu, J., Huber, D., Bedding, T. R., et al., Asteroseismology of 16,000 Kepler Red Giants: Global Oscillation Parameters, Masses, and Radii. 2018, *Astrophysical Journal, Supplement*, **236**, 42, DOI: 10.3847/1538-4365/aaaf74

Consequences of parameterization choice on eclipsing binary light curve solutions

J. Korth[1], A. Moharana[2], M. Pešta[3], D.R. Czavalinga[4] and K.E. Conroy[5]

[1] *Rheinisches Institut für Umweltforschung, Abteilung Planetenforschung an der Universität zu Köln, Universität zu Köln, Aachenerstrae 209, 50931 Köln, (E-mail: judithkorth@gmail.com)*

[2] *Nicolaus Copernicus Astronomical Center, Polish Academy of Sciences, ul. Rabiańska 8, 87-100 Toruń, Poland, (E-mail: ayushm@ncac.torun.pl)*

[3] *Institute of Theoretical Physics, Charles University, V Holešovičkách 2, 180 00 Praha 8, Czech Republic, (E-mail: pestamilan@gmail.com)*

[4] *Institute of Physics, University of Szeged, 6720 Szeged, Hungary, (E-mail: czdonat@titan.physx.u-szeged.hu)*

[5] *Department of Astrophysics and Planetary Science, Villanova University, 800 East Lancaster Avenue, Villanova, PA 19085, USA*

Abstract. Eclipsing Binaries (EBs) are known to be the source of most accurate stellar parameters, which are important for testing theories of stellar evolution. With improved quality and quantity of observations using space telescopes like *TESS*, there is an urgent need for accuracy in modeling to obtain precise parameters. We use the soon to be released `PHOEBE 2.3` EB modeling package to test the robustness and accuracy of parameters and their dependency on choice of parameters for optimization.

Key words: Stars: binaries: eclipsing – stars: fundamental parameters – methods: numerical

1. Introduction

It is well known that eclipsing binaries (EBs) provide highly accurate observations of stellar parameters, which is important for testing theories of star evolution. Thanks to the increasingly more precise photometry of the past and recent space missions (e.g. *Kepler* (Borucki, 2016) and the Transiting Exoplanet Survey Satellite (*TESS*;Ricker et al., 2014)), it is now possible to observe and study EBs in details never seen before (e.g. reflection from the companion, lensing, or Doppler beaming). To understand the observations, one needs to employ

models capable of making predictions with sufficient precision, so that it is possible to compare the observations with predicted theoretical values. A popular example of such software is PHOEBE (Prša et al., 2016; Horvat et al., 2018; Jones et al., 2020), a robust Python package for modeling of EB systems. The latest release provides users with control over a large number of orbital and physical parameters, which allows them to generate synthetic light curves and radial velocities of the binary system. One can also take advantage of various built-in or imported solvers (e.g. emcee) and optimizers (e.g. Nelder-Mead) to solve the inverse problem—for a comprehensive introduction to the inverse problem using PHOEBE see Conroy et al. (2020).

For the purpose of this paper, we use the soon to be released version 2.3 of PHOEBE to try and reproduce the results from the article by Maxted et al. (2020), which examines a number of various methods to accurately estimate the masses and radii for the stars in the binary system AI Phoenicis (AI Phe). This system, which contains two well-separated, sharp-lined stars of comparable luminosity, was first identified as an EB by Strohmeier (1972). It is an excellent target for model testing as it is relatively bright ($V = 8.6\,\mathrm{mag}$), has a long orbital period ($P \approx 24.59\,\mathrm{days}$), and does not show any distinct spots nor flares associated with increased magnetic activity of the components (e.g., Kirkby-Kent et al., 2016; Maxted et al., 2020).

To compare the results by Maxted et al. (2020), we first carried out a number of runs with varying underlying physical models, free parameters, and their initial values (see Section 2). This further motivated us to design a controlled experiment in order to systematically analyze the effect of parameterization choice on the final light curve resulting from the model (Section 3). Finally, in Section 4, we compare our results from the controlled experiment with the Maxted et al. (2020) values, and we discuss our findings regarding the precision of the employed model.

2. Observations and Modeling Set-up

The photometric data of AI Phe used in the subsequent analyses were obtained under the *TESS* Guest Investigator Program (G011130, P.I. Maxted; G011083, P.I. Helminiak; G011154, P.I. Pra) during Sector 2 of the *TESS* mission observed in the 2-min cadence mode (TIC 102069549). The Sector was observed for 27 days from 2458354.113259 BJD to 2458381.517643 BJD (covering both the primary and secondary eclipse), and the data were reduced by the *TESS* data processing pipeline developed by the Science Processing Operations Center (SPOC; Jenkins et al., 2016). In our analyses, we used the Pre-search Data Conditioning Simple Aperture Photometry (PDCSAP) light curve, which was additionally detrended by fitting a chain of 5th order Legendre polynomials (Maxted et al., 2020, Section 2.6).

To get a sense of the effect of parameterization on the resulting values, we independently solved the inverse problem for AI Phe by using a separate model with its own set of free parameters and approximation of physical phenomena (e.g. limb-darkening law, reflection, etc.). Following the approach from Maxted et al. (2020), we initialized the parameters of the models with their estimates from Kirkby-Kent et al. (2016), which are summarized in Table 1.

Table 1. A list of the parameters of the binary system AI Phe that were adopted from Kirkby-Kent et al. (2016).

Parameters	Values
P (days)	24.592483
q	1.0417
e	0.1821
$\omega(^o$)	110.73
$i(^o$)	88.502
M_1 (($M_\odot$)	1.1973
M_2 (($M_\odot$)	1.2473
R_1 (($R_\odot$))	1.835
R_2 (($R_\odot$))	2.912
T_1 (K)	6310
T_2 (K)	5237.3

The initialized free parameters were used as input to the Nelder-Mead algorithm (Nelder & Mead, 1965) in order to refine the estimates. These estimates then served as a starting point for initial distributions (either Gaussian or uniform) of the free parameters entering the Markov Chain Monte Carlo (MCMC) algorithm implemented in the `emcee` solver (Foreman-Mackey et al., 2013), which we used to obtain posterior distributions of the relevant parameters. Furthermore, we used the following software: `Python` (Van Rossum & Drake, 2009), and the `Python` libraries `Matplotlib` (Hunter, 2007) and `numpy` (van der Walt et al., 2011).

Unfortunately, the individual runs did not yield satisfactory results as the obtained values showed a wide spread. Due to the different choices of parameterization and the large numbers of parameters, it was not possible to associate the observed variation with a specific parameter or a set of parameters. Therefore, we decided to design a controlled experiment, in which we defined a "nominal" run and then we examined the effect of altering the parameters one at a time. For more information see the following section.

3. Controlled Experiment

The "nominal" run (which we shall denote "Run A") served as a benchmark for all the other runs ("B" through "K"), which we systematically varied from Run A in a controlled fashion—that is, for each run, we altered one aspect of the "nominal" set-up and kept the rest unchanged. For the definitions of Runs B–K, see Table 2.

Table 2. A list of the individual runs and their differences from the "nominal" run.

Run	Description
A	The "nominal" run
B	Logarithmic limb darkening law
C	Sample/interpolate in phase-space
D	Marginalization over albedos
E	Marginalization over gravity darkening parameters
F	Marginalization over gravity darkening parameters from Claret & Bloemen (2011)
G	Marginalization over noise nuissance parameter
H	Marginalization over parameters q and a using radial velocities posteriors from Gallenne et al. (2019) on q and $a \sin i$
I	Meshes on binary surfaces to estimate L_{pb}
J	*TESS* light curve without detrending (PDCSAP)
K	Masking the out-of-eclipse points

Run A uses the binary star model ELLC (for more information see Maxted, 2016) with the quadratic limb-darkening law in the "lookup" mode (automatic querying of coefficients from tables based on mean stellar values), and uses the Stefan-Boltzmann approximation in the determination of the passband luminosity, L_{pb}, which is needed to scale the fluxes and estimate the surface-brightness ratio. Similar to our initial test runs, we initialized the parameters with values from Kirkby-Kent et al. (2016), and then used the Nelder-Mead algorithm to refine the estimates. After that, we used the `emcee` solver to sample over the radii, R_1 and R_2, (for the primary and secondary component), the eccentricity, e, along with the argument of pericenter, ω_0, (parameterized as $e \sin \omega_0$ and $e \cos \omega_0$), the time of the primary eclipse, T_0, the third light, l_3, L_{pb}, the ratio of the effective temperature of the secondary and primary component, $T_{\mathrm{secondary}}/T_{\mathrm{primary}}$, and the orbital inclination, i, to get an estimate for their uncertainties. We present the obtained results in Fig. 1.
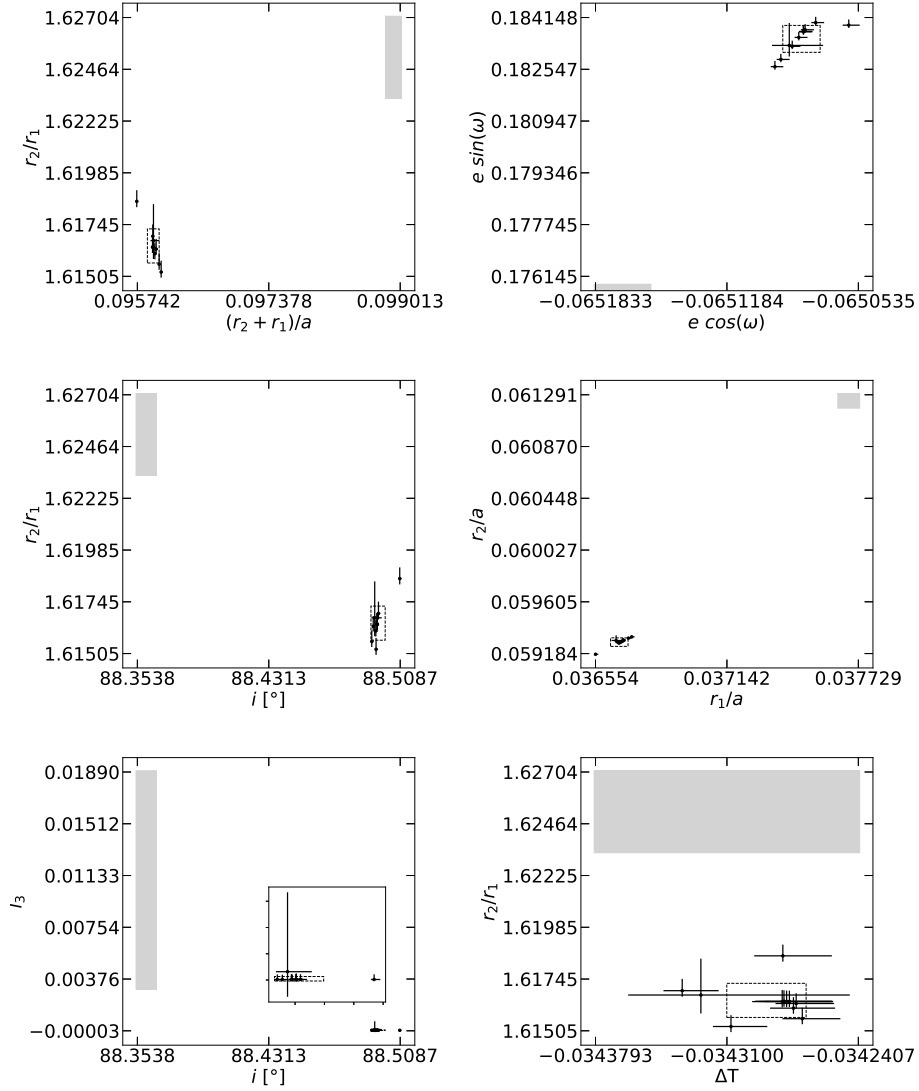
Figure 1. A comparison between the parameters resulting from Runs A–K and those obtained by Maxted et al. (2020). The filled rectangle represents the 1-σ spread around the average of the runs from the Maxted et al. paper (see Table 3), while the dotted box shows the same for our controlled runs. The inner box in the l_3 vs i plot represents a zoomed-in view on the parameter distribution.

4. Discussion of Results

Analysis of Runs A–K shows a rather limited spread of the obtained values, with the individual parameters lying within each other's uncertainties (see Fig. 1). Seeing that the parameters have a fairly small effect on the final results, this implies that the high variation of our initial runs was most likely not caused by any specific parameter but rather by a combined effect of various parameterization choices. That said, it is still clear that the choices made in Table 2 do influence the final results.

As for the runs presented in Maxted et al. (2020), each of them employs a distinct combination of the underlying physical model, optimization method and parameterization (see Table 3). In principle, to properly compare our results with those obtained by Maxted et al. (2020), the initial set-ups should also be compared so that the effect of initial configuration choice can be distinguished from other effects. Although we compare our results with all the runs listed in Table 3 (see Fig. 1), we shall inspect in detail only the initial set-ups for Runs A and S by Maxted, as they utilize the same physical binary model (`ellc`) and optimization method (`emcee`) as our runs. Our runs use a wrapper for mapping of `PHOEBE` parameterization onto `ellc`), and thus they minimize the effect of choice (there is still the freedom of parameterization) and can serve as a "benchmark" for our results. Moreover, Runs A and S by Maxted use essentially the same initial set-ups, therefore it suffices to examine only the former (which additionally corrects for instrumental systematic variations). To avoid confusion, we shall prefix the runs by Maxted et al. (2020) with "M-" (e.g. Run A by Maxted becomes Run M-A) in the rest of the section.

For the sake of simplicity, we shall compare the parameterization of Run M-A only with our "nominal" Run A, which is assumed to be representative of the other runs (for their definitions, see Table 2). In Table 4, we compare the free parameters entering the `emcee` algorithm in the two runs. Apart from working with mostly disjunct (but correlated) sets of free parameters, the runs also differ in the limb-darkening law (power-2 for Run M-A and quadratic for Run A) and the treatment of the stellar masses. Run A adopts the values $1.1973\,M_\odot$ and 1.0417 from Kirkby-Kent et al. (2016) for the mass of the primary component and the ratio of the masses of the secondary and primary component, respectively. In addition, the stellar masses are held constant at the Kirkby-Kent values as they have minimal effect on the light curve. In contrast, Run M-A uses the `emcee` posterior distributions of the free parameters together with observed radial velocities of the binary system to get an estimate for the masses. Finally, both runs hold the semi-major axis constant, with Run M-A assuming the value of $47.868\,R_\odot$ and Run A keeping it equal to $47.941\,R_\odot$.

Coming back to the general case, we expected our results to agree with those obtained by Maxted et al. (2020) within the reported uncertainties despite the

Table 3. An overview of the various runs analysed in the paper by Maxted et al. (2020). The table was adopted from page 6 of the mentioned paper.

Run	Investigator	Model	Optimization	Limb-darkening	Detrending	Notes
A	Maxted	`ellc`	`emcee`	power-2	`celerite`	
B	Helminiak	`JKTEPOB`	L-M	quadratic	sine+poly	Monte Carlo error estimated
C	Torres	EB	`emcee`	quadratic	spline	Quadratic l.d. coeffs. fixed
D	"	"	"	"	"	
E	Graczyk	WD2007	L-M	logarithmic	–	Fixed l.d. coefficients
F	Johnston	`PHOEBE 1.0`	`emcee`	square-root	–	
G	Pra	`PHOEBE 2.1`	MCMC	grid	legendre	
H	Orosz	ELC	DE-MCMC	logarithmic	polynomial	
I	Orosz	"	"	square-root	"	
J	Orosz	"	"	quadratic	"	
K	Southworth	`JKTEBOP`	L-M	quadratic	polynomial	
L	Southworth	`JKTEBOP`	L-M	cubic	polynomial	
S	Maxted	`ellc`	`emcee`	power-2	`celerite`	Same as Run A with SAP light curve

Table 4. A list of the free parameters entering the `emcee` algorithm in Runs M-A and A. The "Nelder-Mead" column marks the parameters which were optimized before running `emcee`, in order to speed-up the convergence of the posterior distributions.

Parameter	Description	Run M-A	Run A	
		emcee	Nelder-Mead	emcee
$e \cos \omega$			✓	✓
$e \sin \omega$			✓	✓
f	Flux scaling factor	✓		
f_c	$\sqrt{e} \cos \omega$	✓		
f_s	$\sqrt{e} \sin \omega$	✓		
$h_{1,\mathrm{F}}, h_{2,\mathrm{F}}$	Parameters of the power-2 limb darkening law for star 1	✓		
$h_{1,\mathrm{K}}, h_{2,\mathrm{K}}$	Parameters of the power-2 limb darkening law for star 2	✓		
i	Orbital inclination	✓	✓	✓
k	Ratio of the radii	✓		
l_3	Third light	✓		✓
L_{pb}	Passband luminosity			✓
r_{sum}	Sum of the fractional radii	✓		
R_1	Radius of the primary star		✓	✓
R_2	Radius of the secondary star		✓	✓
σ_f	Standard error per observation	✓		
S_{T}	Surface brightness ratio averaged over the stellar disks in the TESS band	✓		
T_0	Time of primary eclipse	✓	✓	✓
$T_{\mathrm{secondary}}/T_{\mathrm{primary}}$	Ratio of the effective temperatures		✓	✓

differences in the initial set-ups of the runs. However, Fig. 1 shows that this is not the case as none of the results from Runs AK lies in the 1-sigma spread of the Maxted et al. (2020) values. As to the reason behind this discrepancy, multiple explanations present themselves. First, due to time and computational

constraints, we stopped our `emcee` runs after appearing flat (converged to a single value) for about 1500 iterations compared to ∼10000 iterations for the runs in Maxted et al. (2020). Thus, there is a slight possibility that the runs might yet "jump" and converge to some other values. All of our runs, however, were treated consistently with each other, and still exhibit the influence of a number of decisions in the fitting process on the final results. Next, the mapping between the `PHOEBE` and `ellc` parameterizations includes several assumptions and approximations, which leads to residuals between the two forward models (see Fig. 2). This suggests that the offset between the two sets of results might be caused by not employing the native `PHOEBE` backend.
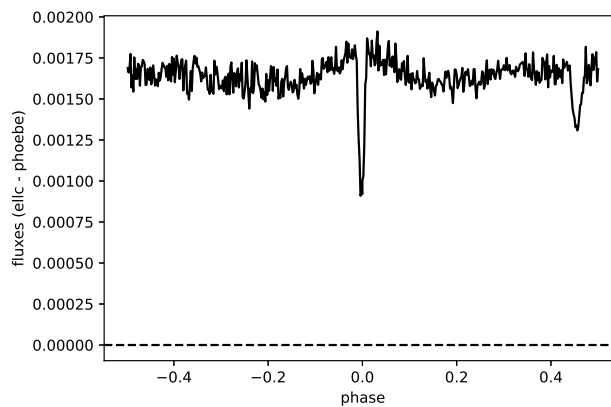
Figure 2. Residuals between the `ellc` and `PHOEBE` forward models for the nominal case. This shows the influence of the approximations in mapping between the parameterization of the different codes and likely explains the offset between the results from our controlled sample and those in Maxted et al. (2020).

5. Conclusions

In this work, we tried to fit the parameters of AI Phoenicis from the *TESS* light curve and to reproduce the values estimated by Maxted et al. (2020). First, we independently modeled the light curves with individual sets of free parameters and their approximations, e.g., difference between initialized parameters of binary masses, radius, effective temperatures of the stars, or model of limb darkening, reflections etc. Since our independent models did not lead to the same results for the system parameters of AI Phe, we designed a controlled experiment to systematically analyze the effect of the parameterization.

The parameters obtained from different runs were expected to be distributed in a parameter space as found in Maxted et al. (2020) but we find our results to be quite different in comparison to the accuracy that has been found before. We suspect the discrepancy may be reconciled by running `emcee` for substantially longer to allow further convergence and to switch to the native `PHOEBE` forward model to avoid the assumptions and approximations in the translation between parameterizations. Our results do, however, show the importance of several different choices in the fitting process on the final parameter values and their uncertainties.

Acknowledgements.

References

Borucki, W. J., KEPLER Mission: development and overview. 2016, *Reports on Progress in Physics*, **79**, 036901, DOI: 10.1088/0034-4885/79/3/036901

Claret, A. & Bloemen, S., Gravity and limb-darkening coefficients for the Kepler, CoRoT, Spitzer, uvby, UBVRIJHK, and Sloan photometric systems. 2011, *Astronomy and Astrophysics*, **529**, A75, DOI: 10.1051/0004-6361/201116451

Conroy, K. E., Kochoska, A., Hey, D., et al., Physics of Eclipsing Binaries. V. General Framework for Solving the Inverse Problem. 2020, *arXiv e-prints*, arXiv:2006.16951

Foreman-Mackey, D., Hogg, D. W., Lang, D., & Goodman, J., emcee: The MCMC Hammer. 2013, *Publications of the Astronomical Society of the Pacific*, **125**, 306, DOI: 10.1086/670067

Gallenne, A., Pietrzyński, G., Graczyk, D., et al., The Araucaria project: High-precision orbital parallax and masses of eclipsing binaries from infrared interferometry. 2019, *Astronomy and Astrophysics*, **632**, A31, DOI: 10.1051/0004-6361/201935837

Horvat, M., Conroy, K. E., Pablo, H., et al., Physics of Eclipsing Binaries. III. Spin–Orbit Misalignment. 2018, *The Astrophysical Journal Supplement Series*, **237**, 26, DOI: 10.3847/1538-4365/aacd0f

Hunter, J. D., Matplotlib: A 2D graphics environment. 2007, *Computing in Science & Engineering*, **9**, 90, DOI: 10.1109/MCSE.2007.55

Jenkins, J. M., Twicken, J. D., McCauliff, S., et al., The TESS science processing operations center. 2016, in Society of Photo-Optical Instrumentation Engineers (SPIE) Conference Series, Vol. **9913**, *Software and Cyberinfrastructure for Astronomy IV*, 99133E

Jones, D., Conroy, K. E., Horvat, M., et al., Physics of Eclipsing Binaries. IV. The Impact of Interstellar Extinction on the Light Curves of Eclipsing Binaries. 2020, *The Astrophysical Journal Supplement Series*, **247**, 63, DOI: 10.3847/1538-4365/ab7927

Kirkby-Kent, J. A., Maxted, P. F. L., Serenelli, A. M., et al., Absolute parameters for AI Phoenicis using WASP photometry. 2016, *Astronomy and Astrophysics*, **591**, A124, DOI: 10.1051/0004-6361/201628581

Maxted, P. F. L., ellc: A fast, flexible light curve model for detached eclipsing binary stars and transiting exoplanets. 2016, *Astronomy and Astrophysics*, **591**, A111, DOI: 10.1051/0004-6361/201628579

Maxted, P. F. L., Gaulme, P., Graczyk, D., et al., The TESS light curve of AI Phoenicis. 2020, *Monthly Notices of the RAS*, **498**, 332, DOI: 10.1093/mnras/staa1662

Nelder, J. A. & Mead, R., A Simplex Method for Function Minimization. 1965, *The Computer Journal*, **7**, 308, DOI: 10.1093/comjnl/7.4.308

Prša, A., Conroy, K. E., Horvat, M., et al., PHYSICS OF ECLIPSING BINARIES. II. TOWARD THE INCREASED MODEL FIDELITY. 2016, *The Astrophysical Journal Supplement Series*, **227**, 29, DOI: 10.3847/1538-4365/227/2/29

Ricker, G. R., Winn, J. N., Vanderspek, R., et al., Transiting Exoplanet Survey Satellite (TESS). 2014, in Society of Photo-Optical Instrumentation Engineers (SPIE) Conference Series, Vol. **9143**, *Space Telescopes and Instrumentation 2014: Optical, Infrared, and Millimeter Wave*, ed. J. Oschmann, Jacobus M., M. Clampin, G. G. Fazio, & H. A. MacEwen, 914320

Strohmeier, W., Three New Bright Eclipsing Binaries. 1972, *Information Bulletin on Variable Stars*, **665**, 1

van der Walt, S., Colbert, S. C., & Varoquaux, G., The NumPy Array: A Structure for Efficient Numerical Computation. 2011, *Computing in Science Engineering*, **13**, 22, DOI: 10.1109/MCSE.2011.37

Van Rossum, G. & Drake, F. L. 2009, *Python 3 Reference Manual* (Scotts Valley, CA: CreateSpace)

Improving light curve parameters of exoplanets based on *TESS* data

P. Gajdoš[1]**, A. Maliuk**[2]**, M. Vítková**[3] **and H. Parviainen**[4,5]

[1] *Institute of Physics, Faculty of Science, Pavol Jozef Šafárik University,*
040 01 Košice, Slovakia (E-mail: pavol.gajdos@student.upjs.sk)

[2] *Astronomical Institute of the Slovak Academy of Sciences*
059 60 Tatranská Lomnica, The Slovak Republic(E-mail: amaliuk@ta3.sk)

[3] *Department of Theoretical Physics and Astrophycis, Masaryk University,*
Kotlářská 2, 611 37 Brno, Czech Republic (E-mail: 474624@mail.muni.cz)

[4] *Instituto de Astrofísica de Canarias (IAC), 38205 La Laguna, Tenerife,*
Spain

[5] *Departamento de Astrofísica, Universidad de La Laguna (ULL), 38206, La*
Laguna, Tenerife, Spain

Abstract. We revise parameters of four transiting hot Jupiter planets discovered by ground-based surveys. We use follow-up observations carried by *TESS* mission together with `PyTransit` software. Space telescopes like *TESS* provide better coverage and photometry precision than ground-based telescopes. `PyTransit` is fast and user-friendly exoplanet transit light curve modelling package, implementing optimised versions of the Gimenéz and the Mandel & Agol transit models. After applying `PyTransit` to *TESS* data, our results show an improvement in the exoplanets parameters estimation.
Key words: Methods: data analysis – Techniques: photometric – Stars: planetary systems – Stars: individual: HAT-P-5, HATS-33, HATS-24

1. Introduction

Extrasolar planets are exotic substellar objects which were discovered only recently. This field of research is evolving quickly and opening new possibilities, surprises and challenges.

There are different methods for detecting exoplanets. The major part of exoplanets was discovered using transit and radial velocity methods. Transit photometry is based on decreasing of stellar brightness while exoplanet moves across the disc of the host star. Planets that eclipse their host star during their orbit are key objects for the study of exoplanetary systems. Our main goal is to improve the precision of known exoplanet parameters using new data from the Transiting Exoplanet Survey Satellite (*TESS*).

The *TESS*, launched in 2018, was designed as all-sky space survey searching for exoplanets orbiting the bright stars – brighter than 12 mag (Ricker et al.,

2014). The spacecraft consists of four 100-mm telescopes (f/1.4) with four CCD cameras each with resolution 4 Mpx. The complete field of view is 24×96 degrees. *TESS* uses the broad bandpass filter ($600 - 1000\,$nm) which is centred on the traditional I_C filter. During the primary mission (from July 2018 to July 2020), the nearly whole sky was observed in 26 sectors. Each sector is 27.4-days long. Every 30 minutes, the full-frame image was obtained. For selected targets, the short-cadence data is available. They are collected every 2 minutes.

Up to date (24 September 2020)[1], 74 confirmed planets and more than 2300 candidates were discovered by *TESS*. The first exoplanet discovered by *TESS* is Super-Earth π Mensae c (Huang et al., 2018). At the beginning of 2020, the discovery of the first Earth-sized exoplanet in the habitable zone TOI-700 d was reported (Gilbert et al., 2020). Vanderburg et al. (2020) recently, in September 2020, presented the planet candidate (TIC 267574918) transiting a white dwarf. Many of exoplanets discovered by other missions were already observed by *TESS* with very high precision which allows us to analyse these planets in more details. Compared with most of the ground-based surveys, *TESS* provides much better coverage and photometry precision. This allows us to collect more reliable data about known exoplanets.

In this report, we summarised our results obtained during "GAIA & TESS: Tools for understanding of the Local Universe" summer school. We used the data obtained by the *TESS* mission to study transiting exoplanets. Our main task was to study the already known transiting exoplanets using the *TESS* data and compare the obtained values of parameters with the literature.

2. Transit Modelling

During our work on exoplanet characterisation, we used `PyTransit` software created by Parviainen (2015). PyTransit is a package for exoplanet transit light curve modelling. `PyTransit` combines a Bayesian approach to inference with Markov chain Monte Carlo (MCMC) sampling for the posterior estimation. This allows improving characterisation of model parameters uncertainties. The package includes necessary utility routines to calculate circular or elliptic orbits, transit durations, eclipse centres etc. `PyTransit` needs normalised de-trended light curve for work. Some small additional trend and/or stellar variability could be removed using gaussian processes (Foreman-Mackey et al., 2017) during the fitting. Initial distributions of prior parameters (orbital period, time of primary transit, transit depth) are also required. The package can use Giménez (2006), Mandel & Agol (2002), Maxted & Gill (2019) or RoadRunner (Parviainen, 2020) transits models with various limb darkening laws.

The Bayesian approach allows finding posterior probability density of target parameters if likelihood function and prior density are known. This method can be implied iteratively after each new piece of data arrives. This allows us to

---

[1]https://exoplanetarchive.ipac.caltech.edu/

use known exoplanet parameters from the literature as priors for `PyTransit`. From previous studies, we use transit depth, orbital period and time of primary transit as initial values which were optimized with other parameters during the fitting.

In this work, we use Mandel & Agol transit model with quadratic limb darkening law as the most common one. Limb darkening coefficients were optimised by `PyTransit`. We assume that the shapes of the planet and star are spherical and orbits are circular. The algorithm operates by phase-folding data over a range of trial parameters (transit depth, orbital period, time of primary transit, impact parameter, stellar density and limb darkening coefficients). It calculates the χ^2 statistic of the phase-folded light curve between the data points of the respective transit model and the observed values. Then the global χ^2 minimum is used. Markov chain Monte Carlo methods create samples from a continuous random variable, with probability density proportional to a known function. Creating synthetic light curves with this method and running the model fitting on them gives us a reliable estimation of uncertainties of parameters of our model. Finally, we calculated the values of some common planetary parameters (semi-major axis, radius ratio, planet radius and inclination) from the obtained values of optimized parameters (mentioned above).

3. Studied systems

For the purpose of this study, we selected three transiting exoplanets (see Tab. 1) discovered by ground-based projects HAT (Hungarian Automated Telescope Network; Bakos et al., 2004) and HAT South (Bakos et al., 2013). These targets were already observed by *TESS* mission and have not been studied using these data, yet. The selected planets belong to the category of hot Jupiter planets. These are Jupiter-size planets orbit the parent star on very close orbits with periods of only a few days.

3.1. HAT-P-5 b

The hot Jupiter HAT-P-5 b was discovered by HATNet project in 2005 and confirmed in 2007 by Bakos et al. (2007). This exoplanet was named by Slovak citizens in IAU campaign "NameExoWorlds" (Penteado et al., 2019). The name of the planet is Kráľomoc and parent star is Chasoň. The names come from Slavic mythology. The parent star is a sun-like star with effective temperature $5960 \pm 100\,\mathrm{K}$, radius $1.12 \pm 0.09\,\mathrm{R_\odot}$ and mass $1.04 \pm 0.29\,\mathrm{M_\odot}$ (Stassun et al., 2017). Its distance is $306.0 \pm 1.8\,\mathrm{pc}$ (Gaia Collaboration, 2018). Parameters of the planet are listed in Tab. 1. Southworth et al. (2012) studied HAT-P-5 using ground-based follow-up observations. They obtained similar results to Bakos et al. (2007).
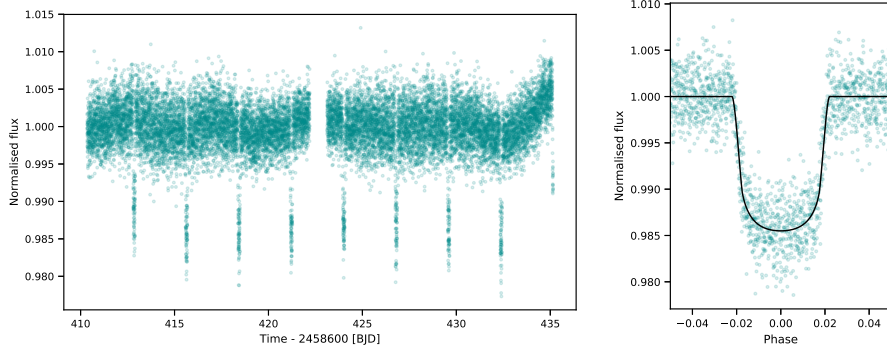
Figure 1. *TESS* light-curve (*left*) and phase curve (*right*) of HAT-P-5 b. Black curve corresponds to model created with `PyTransit`.
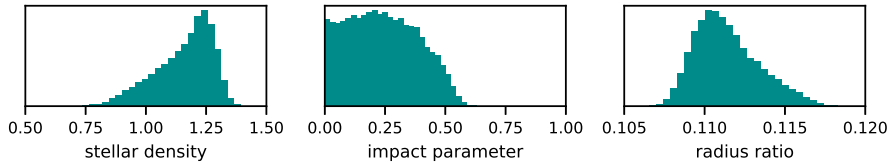
Figure 2. Posterior distributions of fitted parameters of HAT-P-5 b transit.

TESS mission observed HAT-P-5 in Sector 26 (from 8 June to 4 July 2020). The nine transit events were observed (see Fig. 1). However, the last transit was observed only partially – only ingress part.

We obtained asymmetric posterior distributions of more fitted parameters from MCMC sampling (Fig. 2). These distributions are not normal (Gaussian). Therefore, we had to calculate the separate values of the upper and lower uncertainties of these parameters. We could also put only the upper limit on the impact parameter (< 0.485) for the same reason. Except for this, the obtained values of parameters (Tab. 2) agree with the values from the literature (Tab. 1).

3.2. HATS-24 b

HATS-24 b was discovered by HATSouth project in 2017 (Bento et al., 2017). HATSouth survey is a network of 6 astrograph telescope systems designed to detect transiting exoplanets in orbit around relatively bright stars visible from the Southern hemisphere (Bakos et al., 2013). The exoplanet is orbiting F-dwarf star with mass $1.218 \pm 0.036\,\mathrm{M_\odot}$, radius $1.194\,^{+0.066}_{-0.041}\,\mathrm{R_\odot}$ and effective temper-

ature $6346 \pm 81\,\mathrm{K}$ (Bento et al., 2017). HATS-24b is high-mass hot Jupiter and main parameters are listed in Tab. 1.
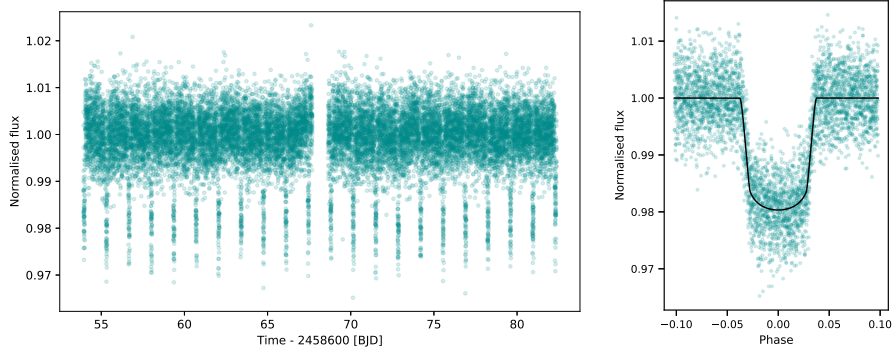
Figure 3. *TESS* light-curve (*left*) and phase curve (*right*) of HATS-24 b. Black curve corresponds to model created with `PyTransit`.
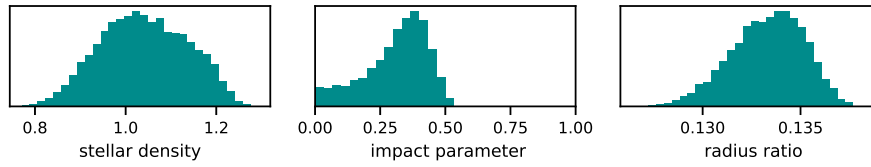
Figure 4. Posterior distributions of fitted parameters of HATS-24 b transit.

TESS observed HATS-24 b in 13$^{\mathrm{th}}$ sector and detected 22 transits. Data from *TESS* are shown in Fig. 3. Using this data we tried to improve parameters. We used `PyTransit` for fitting and we obtained almost symmetric posterior distributions of fitted parameters (see Fig. 4). In Tab. 2 are listed obtained values from our MCMC fitting. Our results are in good agreement with the values from the literature.

3.3. HATS-33 b

HATS-33 b was discovered by de Val-Borro et al. (2016) in the boundaries of the *HATSouth* survey. HATS-33 b planet was classified as typical hot Jupiter with period 2.549 d and radius $1.23\,\mathrm{R_{Jup}}$. Main parameters of the planet are listed in Tab. 1.
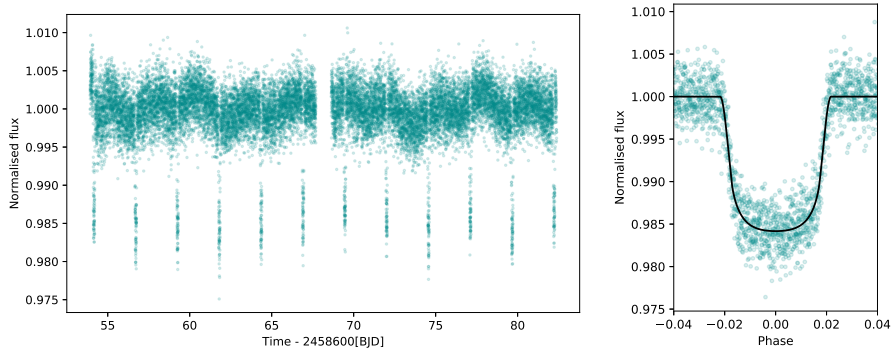
Figure 5. *TESS* light-curve (*left*) and phase curve (*right*) of HATS-33 b. Black curve corresponds to model created with `PyTransit`.
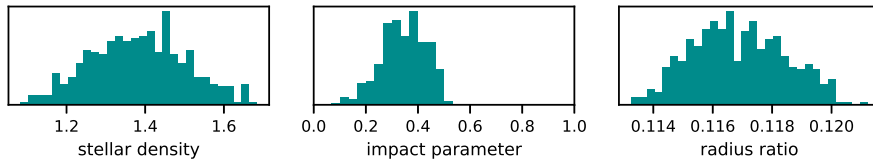
Figure 6. Posterior distributions of fitted parameters of HATS-33 b transit.

The host star is a sun-like star with effective temperature 5659 ± 85 K, radius 1.022 ± 0.05 $R_\odot$ and mass 1.062 ± 0.032 $M_\odot$ (de Val-Borro et al., 2016). HATS-33 b was observed by *TESS* in 13th sector. With this new data, we tried to improve exoplanet parameters. The model of transit created with `PyTransit` is displayed in Fig. 5. New parameters of exoplanet are listed in Tab. 2. We obtained almost symmetric posterior distributions of most of the fitted parameters from MCMC sampling (Fig. 6). These distributions are close to normal (Gaussian). `PyTransit` allowed us to obtain 10 times better precision for the orbital period and 5 times better precision for radius ratio. In general, obtained values of parameters (Tab. 2) are in good agreement with the values from the literature.

4. Summary

We used photometric data collected by space mission *TESS* to redetermine the basic parameters of three exoplanets HAT-P-5 b, HATS-33 b and HATS-24 b. *TESS* provides data with high precision and high cadence. It allows to

Table 1. Parameters of exoplanets and parent stars from literature: $R_\star$ - radius of the star, $M_\star$ - mass of the star, $T_{\rm eff}$ - effective temperature of the star, t_c - transit epoch (BJD - 2450000), p - orbital period, Δ - transit depth, b - impact parameter, $\rho_\star$ - stellar density, q_1, q_2 - coefficients of quadratic limb-darkening (given by Claret 2017), a - semi-major axis, i - orbital inclination, k - radius ratio, r_p - planet radius.

	HAT-P-5 b [1,2]	HATS-24 b [3,4]	HATS-33 b [5]
$R_\star$ [$R_\odot$]	1.12 ± 0.09	$1.194\,^{+0.066}_{-0.041}$	1.022 ± 0.05
$M_\star$ [$M_\odot$]	1.04 ± 0.29	1.218 ± 0.036	1.062 ± 0.032
$T_{\rm eff}$ [K]	5960 ± 100	6346 ± 81	5659 ± 85
t_c [BJD]	$4241.7766 \pm 2 \cdot 10^{-4}$	$7948.709321 \pm 4 \cdot 10^{-5}$	$6497.23181 \pm 5 \cdot 10^{-4}$
p [d]	$2.7884910 \pm 2.5 \cdot 10^{-5}$	$1.3484954 \pm 1.3 \cdot 10^{-6}$	$2.5495551 \pm 6.1 \cdot 10^{-6}$
Δ [%]	1.240 ± 0.013	1.638 ± 0.004	1.530 ± 0.198
b [$R_\star$]	0.425 ± 0.048	—	0.33 ± 0.12
$\rho_\star$ [g/cm^3]	1.03 ± 0.18	—	1.42 ± 0.17
q_1	0.275	0.240	0.342
q_2	0.294	0.299	0.260
a [$R_\star$]	7.50 ± 0.19	4.561 ± 0.029	7.843 ± 0.078
a [au]	0.04075 ± 0.00076	0.02380 ± 0.00100	0.03727 ± 0.00037
i [°]	86.75 ± 0.44	85.97 ± 0.26	87.62 ± 0.92
k [—]	0.1106 ± 0.0006	0.12801 ± 0.00017	0.1237 ± 0.0080
r_p [$R_{\rm jup}$]	1.260 ± 0.050	1.395 ± 0.057	$1.230\,^{+0.112}_{-0.081}$

Source: (1) Bakos et al. (2007), (2) Stassun et al. (2017), (3) Bento et al. (2017), (4) Oliveira et al. (2019), (5) de Val-Borro et al. (2016).

Table 2. New parameters of exoplanets. For detail description see Table 1.

	HAT-P-5 b	HATS-24 b	HATS-33 b
t_c [BJD]	$5432.4551 \pm 5 \cdot 10^{-4}$	$7038.47339 \pm 3.7 \cdot 10^{-4}$	$6497.2318 \pm 5 \cdot 10^{-4}$
p [d]	$2.7884732 \pm 4 \cdot 10^{-7}$	$1.34849750 \pm 3.3 \cdot 10^{-7}$	$2.549564 \pm 6.2 \cdot 10^{-7}$
Δ [%]	$1.235\,^{+0.054}_{-0.036}$	1.779 ± 0.051	1.346 ± 0.035
b [$R_\star$]	< 0.485	0.34 ± 0.12	0.35 ± 0.08
$\rho_\star$ [g/cm^3]	$1.18\,^{+0.09}_{-0.16}$	1.039 ± 0.096	1.38 ± 0.12
q_1	0.482 ± 0.235	0.170 ± 0.152	0.565 ± 0.210
q_2	$0.170\,^{+0.214}_{-0.104}$	0.299 ± 0.264	0.144 ± 0.130
a [$R_\star$]	$7.86\,^{+0.20}_{-0.36}$	4.64 ± 0.14	7.85 ± 0.28
a [au]	$0.04097\,^{+0.00097}_{-0.00189}$	0.02576 ± 0.00078	0.03731 ± 0.00133
i [°]	> 86.16	85.82 ± 1.58	87.55 ± 1.03
k [—]	$0.1111\,^{+0.0028}_{-0.0017}$	0.1334 ± 0.0019	0.1160 ± 0.0015
r_p [$R_{\rm jup}$]	$1.211\,^{+0.026}_{-0.018}$	1.550 ± 0.022	1.154 ± 0.015

characterise the transiting planets in more details than from ground-based observations. Time span of one *TESS* sector is only 27.4 days but it includes several transits of short-period planet such as hot Jupiters. The exposure time of *TESS* data (2 min) is short enough, therefore the brightness of the occulted star does not change significantly during this time and the shape of transit is not deformed.

We confirmed the basic parameters of studied planets given in the literature. We improved the values of many of them. We used MCMC method to estimate their uncertainties which are very reliable. In the case of HAT-P-5 b, we obtained very asymmetric posterior distributions of a few parameters. And for the impact parameter, we could only put an upper limit of it. In other studied planets, the distributions were close to normal (Gaussian) distribution. Obtained values of limb-darkening coefficients do not fully agree with the values calculated by Claret (2017). One reason for these differences could be the large step of stellar parameters in the calculated values. Our coefficients have also large uncertainties. We observed the strong correlations between coefficients q_1 and q_2 which could affect our results. However, another explanation of our large uncertainties may be the fact that even a large change of limb-darkening coefficients has minimal effect on the shape of transit.

Our results show that TESS data should be used to study already discovered transiting exoplanets to improve their parameters.

References

Bakos, G., Noyes, R. W., Kovács, G., et al., Wide-Field Millimagnitude Photometry with the HAT: A Tool for Extrasolar Planet Detection. 2004, *Publications of the ASP*, **116**, 266, DOI: 10.1086/382735

Bakos, G. Á., Csubry, Z., Penev, K., et al., HATSouth: A Global Network of Fully Automated Identical Wide-Field Telescopes. 2013, *Publications of the ASP*, **125**, 154, DOI: 10.1086/669529

Bakos, G. Á., Shporer, A., Pál, A., et al., HAT-P-5b: A Jupiter-like Hot Jupiter Transiting a Bright Star. 2007, *Astrophysical Journal, Letters*, **671**, L173, DOI: 10.1086/525022

Bento, J., Schmidt, B., Hartman, J. D., et al., HATS-22b, HATS-23b and HATS-24b: three new transiting super-Jupiters from the HATSouth project. 2017, *Monthly Notices of the RAS*, **468**, 835, DOI: 10.1093/mnras/stx500

Claret, A., Limb and gravity-darkening coefficients for the TESS satellite at several metallicities, surface gravities, and microturbulent velocities. 2017, *Astronomy and Astrophysics*, **600**, A30, DOI: 10.1051/0004-6361/201629705

de Val-Borro, M., Bakos, G. Á., Brahm, R., et al., HATS-31b through HATS-35b: Five Transiting Hot Jupiters Discovered By the HATSouth Survey. 2016, *Astronomical Journal*, **152**, 161, DOI: 10.3847/0004-6256/152/6/161

Foreman-Mackey, D., Agol, E., Ambikasaran, S., & Angus, R., Fast and Scalable Gaussian Process Modeling with Applications to Astronomical Time Series. 2017, *Astronomical Journal*, **154**, 220, DOI: 10.3847/1538-3881/aa9332

Gaia Collaboration, Gaia Data Release 2. Summary of the contents and survey properties. 2018, *Astronomy and Astrophysics*, **616**, A1, DOI: 10.1051/0004-6361/201833051

Gilbert, E. A., Barclay, T., Schlieder, J. E., et al., The First Habitable-zone Earth-sized Planet from TESS. I. Validation of the TOI-700 System. 2020, *Astronomical Journal*, **160**, 116, DOI: 10.3847/1538-3881/aba4b2

Giménez, A., Equations for the analysis of the light curves of extra-solar planetary transits. 2006, *Astronomy and Astrophysics*, **450**, 1231, DOI: 10.1051/0004-6361:20054445

Huang, C. X., Burt, J., Vanderburg, A., et al., TESS Discovery of a Transiting Super-Earth in the pi Mensae System. 2018, *Astrophysical Journal, Letters*, **868**, L39, DOI: 10.3847/2041-8213/aaef91

Mandel, K. & Agol, E., Analytic Light Curves for Planetary Transit Searches. 2002, *Astrophysical Journal, Letters*, **580**, L171, DOI: 10.1086/345520

Maxted, P. F. L. & Gill, S., qpower2: A fast and accurate algorithm for the computation of exoplanet transit light curves with the power-2 limb-darkening law. 2019, *Astronomy and Astrophysics*, **622**, A33, DOI: 10.1051/0004-6361/201834563

Oliveira, J. M., Martioli, E., & Tucci-Maia, M., First Observation of a Planetary Transit with the SPARC4 CCD: Improved Parameters for HATS-24b. 2019, *Research Notes of the American Astronomical Society*, **3**, 35, DOI: 10.3847/2515-5172/ab06c7

Parviainen, H., PYTRANSIT: fast and easy exoplanet transit modelling in PYTHON. 2015, *Monthly Notices of the RAS*, **450**, 3233, DOI: 10.1093/mnras/stv894

Parviainen, H., RoadRunner: a fast and flexible exoplanet transit model. 2020, *Monthly Notices of the RAS*, **499**, 1633, DOI: 10.1093/mnras/staa2901

Penteado, E. M., Rivero-Gonzalez, J., & Downer, B., IAU100 NameExoWorlds: A Call to Promote Global Citizenship. 2019, *Communicating Astronomy with the Public Journal*, **26**, 5

Ricker, G. R., Winn, J. N., Vanderspek, R., et al., Transiting Exoplanet Survey Satellite (TESS). 2014, in Society of Photo-Optical Instrumentation Engineers (SPIE) Conference Series, Vol. **9143**, *Space Telescopes and Instrumentation 2014: Optical, Infrared, and Millimeter Wave*, 914320

Southworth, J., Mancini, L., Maxted, P. F. L., et al., Physical properties and radius variations in the HAT-P-5 planetary system from simultaneous four-colour

photometry. 2012, *Monthly Notices of the RAS*, **422**, 3099, DOI: 10.1111/j.1365-2966.2012.20828.x

Stassun, K. G., Collins, K. A., & Gaudi, B. S., Accurate Empirical Radii and Masses of Planets and Their Host Stars with Gaia Parallaxes. 2017, *Astronomical Journal*, **153**, 136, DOI: 10.3847/1538-3881/aa5df3

Vanderburg, A., Rappaport, S. A., Xu, S., et al., A Giant Planet Candidate Transiting a White Dwarf. 2020, *Nature*, **585**, 363, DOI: 10.1038/s41586-020-2713-y

Flare stars in nearby Galactic open clusters based on *TESS* data

O. Maryeva[1,2], **K. Bicz**[3], **C. Xia**[4], **M. Baratella**[5], **P. Čechvala**[6] **and K. Vida**[7]

[1] *Astronomical Institute of the Czech Academy of Sciences*
251 65 Ondřejov, The Czech Republic(E-mail: olga.maryeva@asu.cas.cz)

[2] *Lomonosov Moscow State University, Sternberg Astronomical Institute,*
Universitetsky pr. 13, 119234, Moscow, Russia

[3] *Astronomical Institute, University of Wrocław, Kopernika 11, 51-622*
Wrocław, Poland

[4] *Department of Theoretical Physics and Astrophysics, Faculty of Science,*
Masaryk University, Kotlářská 2, 611 37 Brno, Czech Republic

[5] *Dipartimento di Fisica e Astronomia Galileo Galilei, Vicolo Osservatorio 3,*
35122, Padova, Italy, (E-mail: martina.baratella.1@phd.unipd.it)

[6] *Department of Astronomy, Physics of the Earth and Meteorology, Faculty of*
Mathematics, Physics and Informatics,
Comenius University in Bratislava, Mlynská dolina F-2, 842 48 Bratislava,
Slovakia

[7] *Konkoly Observatory, Research Centre for Astronomy and Earth Sciences,*
H-1121 Budapest, Konkoly Thege Miklós út 15-17, Hungary

Abstract. The study is devoted to search for flare stars among confirmed members of Galactic open clusters using high-cadence photometry from *TESS* mission. We analyzed 957 high-cadence light curves of members from 136 open clusters. As a result, 56 flare stars were found, among them 8 hot B-A type objects. Of all flares, 63 % were detected in sample of cool stars ($T_{\text{eff}} < 5000$ K), and 29 % – in stars of spectral type G, while 23 % in K-type stars and approximately 34% of all detected flares are in M-type stars. Using the `FLATW'RM` (FLAre deTection With Ransac Method) flare finding algorithm, we estimated parameters of flares and rotation period of detected flare stars. The flare with the largest amplitude appears on the M3 type EQ Cha star. Statistical analysis did not reveal any direct correlation between ages, rotation periods and flaring activity.

Key words: Galaxy: open clusters and associations: general – stars: flare – stars: activity – space mission: TESS

1. Introduction

Flare stars – stars having detected at least one very short flare in their light curve – are a widely known type of objects in astrophysics. The physical mechanisms leading to the appearance of flares are associated with convective atmospheres, such as in G–M type stars on the main sequence. Thus most of the stars in our Galaxy are potentially flare stars.

In the middle of 20th century, only six flare stars were known (Lippincott, 1952). Since then, a huge progress was made in the field of detecting stellar flares. The interest of astronomers to these objects is associated not only with the incompletely studied mechanisms of formation of flares, but also with the possible influence of flares on habitable zone of potential exoplanets. The *Kepler* mission had a significant impact on the study of flare stars. As a result,
The Kepler Catalog of Stellar Flares with more than 4000 detected flare stars was made by Davenport (2016). And even more significant impact can be expected from the ongoing *Transiting Exoplanet Survey Satellite (TESS)* mission, which already covered full celestial sphere. *TESS* satellite is a space-borne telescope, whose main objective is the detection and study of exoplanets using the technique of transits. However, its database of a high-cadence (2 minute effective sampling) light curves for hundreds of thousands of objects, as well as sequences of Full Frame Images (30 minutes effective sampling), may also provide an invaluable resource for the study of many other kinds of astrophysical objects, including flare stars.

Stellar flares are explosive magnetic reconnection events in a stars magnetosphere (Günther et al., 2020) emitting energy through radio wavelength, X-ray, UV, optical and IR band (Lawson et al., 2019). They show a sharp rise in intensity followed by an exponential decay. Duration of these flares is typically within few minutes to hours (Doyle et al., 2018). The presence of flares indicates magnetic activity in the stellar magnetosphere. Since the magnetic activity is strongly related to the strength of the magnetic field, fast-rotating young stars are typically more active. The magnetic activity also changes over time, so one would expect the frequency and power of flares to change as well. However, it is hard to investigate these changes in G-M type stars due to their long lifetime and slow evolution on the main sequence.

There are several possible ways to estimate the age of such late type stars, such as method based on the rotation period (gyrochronology, Barnes 2007), or spatial motion (kinematic group membership). But probably the most effective and affordable one is by means of estimating an age of a parent cluster. Therefore, the aim of this study is to evaluate the effect of stellar age on the activity of flare stars in Galactic open clusters.

Open clusters are groups of stars loosely held together by their mutual gravitational attraction and formed from the same interstellar molecular cloud. Therefore the age, distance and chemical properties of members in open clusters are approximately identical. This means that the chemical composition of open

clusters also reflects a real composition of individual members (Netopil et al., 2015).

In this paper, we combine the high temporal resolution light curves acquired by *TESS* satellite with the cluster membership data based on *Gaia* DR2 (Cantat-Gaudin et al., 2018a). This allows us to reliably select the members of Galactic open clusters with known age and distance, examine their variability and extract the ones with prominent stellar flares for further statistical analysis.

The paper is organized as follows. In Section 2, we briefly describe a methodology of selection of cluster members having *TESS* light curves available and the methodology of flare detection and characterisation. In Section 3, we present statistical analysis of detected flares. A conclusion of this study is given in Section 4.

2. Selection of flare stars

The first step of our work was the selection of stars belonging to open clusters and being *TESS* targets with high temporal resolution light curves available. To do it, we took a list of Galactic open clusters from Cantat-Gaudin et al. (2018a) and selected the ones closer than 2 kpc from the Sun. Such distance cut-off allows us to discard the clusters where G0V and later type of dwarfs, the most interesting for flare stars statistics, are below *TESS* detection limit due to their intrinsic faintness. Then, we used the list of members from Cantat-Gaudin et al. (2018a) for all selected clusters and checked the availability of *TESS* light curves for every object. As a result, we acquired 859 light curves for stars located in 136 open clusters. We also considered nearby cluster Melote 111 (or Coma Star cluster) with 98 light curves available. Basic parameters of these clusters (age, number of members, distance) are summarized in Table 2, along with the numbers of available light curves and detected flares for them.

As the next step, we performed a visual inspection of all these light curves and discarded the ones without any flares, thus significantly reduced the number of light curves. Then we performed an automated detection and characterisation of the flares using `FLATW'RM` (FLAre deTection With Ransac Method) code (Vida & Roettenbacher, 2018). This code uses a machine-learning algorithm to give a robust model of the light curves in order to detect flare events and uses a voting system implemented to keep false positive detections to a minimum. `FLATW'RM` detects flares and reports the times the flare starts and ends, the time of maximum flux and the maximum percent increase of flux over the light curve around the flare, along with estimated flare energy, either from the raw light curve or by fitting an analytic flare model. It also gives a crude estimation of the period of the underlying light curve, assuming that it is periodic and using the position of the strongest peak in the Lomb-Scargle periodogram.

Figure 1 illustrates the Hertzsprung–Russell (H–R) diagram of several clusters from our analysis with locations of found flare stars and cluster members

with *TESS* high temporal resolution light curves available. We also plotted the isochrones calculated using `PARSEC` (Chen et al., 2014) for metallicities Z=0.017 and Z=0.020 updated to the latest transmission curve calibrated on *Gaia* DR2 data (Evans et al., 2018)[1]. The figure shows that the majority of the found flare stars have masses between $0.5 - 2$ $M_\odot$. Figure 2 presents several clusters where no flare star was detected.
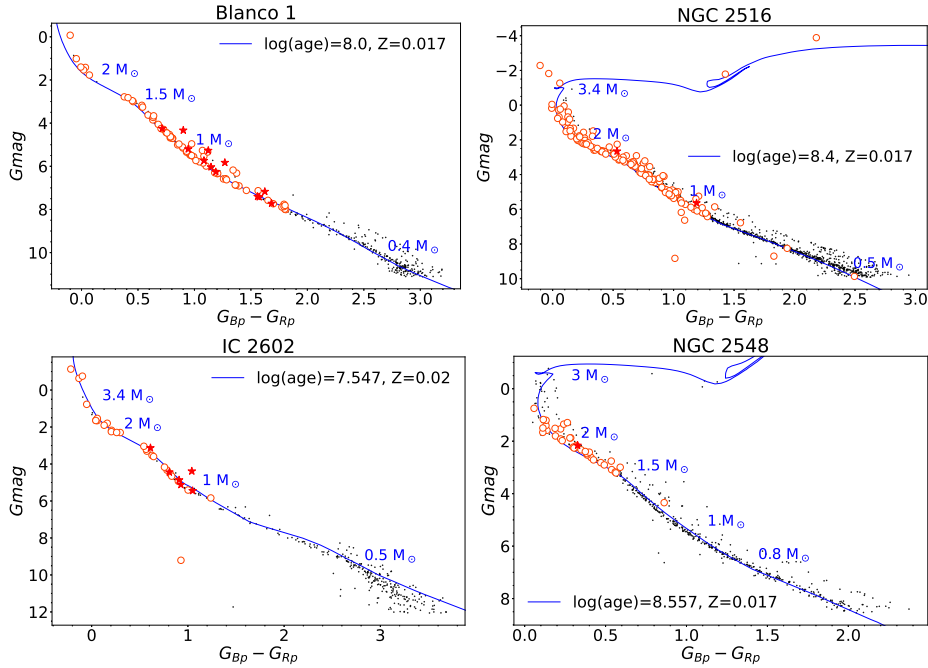
Figure 1. H–R diagram for Blanco 1, NGC 2516, IC 2602 and NGC 2548 clusters based on *Gaia* photometric data and compared with the PARSEC isochrones (see text for details). Red circles are TESS objects without flares, while red stars – with flares.

It is important to note that two of the clusters – ASCC 19 and Gulliver 6 – are located very close on the sky and also on similar distance. Due to this, the star HD 290527 is considered as a member of both clusters simultaneously (Cantat-Gaudin et al., 2018a). On the other hand, the star HD 290674 is considered to be a member of Gulliver 6 according to Cantat-Gaudin et al. (2018a) and a member of ASCC 19 – according to Cantat-Gaudin et al. (2018b). This leads to the ambiguities of the ages for these stars.

―――――――――――――

[1]`PARSEC` isochrones in *Gaia* DR2 passbands are available at `http://stev.oapd.inaf.it/cgi-bin/cmd`
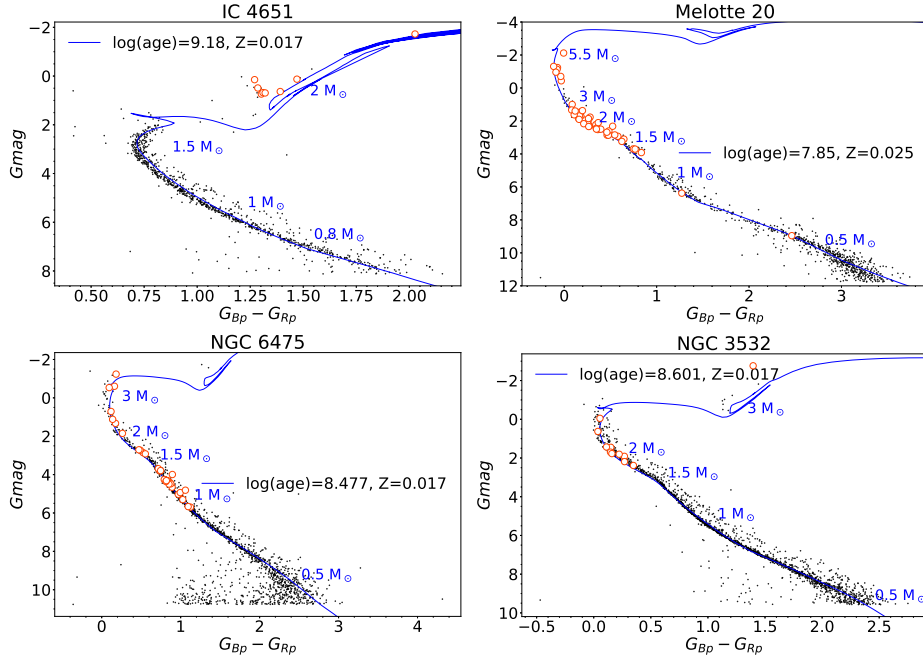
Figure 2. H–R diagram for IC 4651, Melotte 20, NGC 6475 and NGC 3532 clusters based on *Gaia* photometric data and compared with `PARSEC` isochrones. Red circles are TESS objects without flares.

A full list of flare stars we found is given in Table 1. Specified spectral types are taken from the SIMBAD database. As well as spectral types are not known for all star, 5th column gives effective temperatures T_{eff} according to *Gaia* DR2 (Gaia Collaboration et al., 2016, 2018). The 6th column contains the number of flares detected during the period of observations, while the last column is the period of rotation. Both values were estimated using `FLATW'RM`. The code estimates the periods based on the strongest peak in the Lomb-Scargle periodogram, and thus may provide bogus or halved periods in some cases. Therefore we also checked all measured period values by eye and corrected them where necessary so that they clearly correspond to the main periodic components. For one of the stars in our sample – EO Cha – the determined period is close to total duration of observations and might be caused by systematic effects in the data. However, our value is in agreement with the one reported in AAVSO VSX database[2], and thus we decided to keep it in our analysis.

---

[2]American Association of Variable Star Observers Variable Star Index is available in `https://www.aavso.org/vsx/`

Table 1. List of flare stars selected in this work. Spectral types are taken from the SIMBAD database. T_{eff} is temperature taken from *Gaia* DR2 (Gaia Collaboration et al., 2016, 2018). Numbers of flares (N_{fl}) and rotation periods (P_{rot}) are estimated as described in Section 2.

Cluster	*Gaia* DR2 ID	Name	Sp. type	T_{eff}	N_{fl}	P_{rot} [days]
ASCC 19[a]	3220225706694228096	HD 290527	A3	7470	3	6.69
ASCC 21	3236083864117227264	HD 36030	B9V	9777	1	–
Alessi 13	4861032719915154176	–	–	3922	1	2.27
Alessi 13	4860643905115917312	CD-36 1309	F8	5922	4	1.20
Alessi 13	4854771001195018752	CD-37 1263	G5	5637	5	2.06
Blanco 1	2320842551136015872		K4-5V	4954	1	5.55
Blanco 1	2320838943363481984	–	K5.3	4296	5	2.17
Blanco 1	2320874054720005248	–	F-K	4131	1	5.84
Blanco 1	2320933157765826560	CD-30 19826	F-K	5496	3	1.03
Blanco 1	2320596123092361088	–	F-K	5031	2	0.34
Blanco 1	2320862200611102848	–	F-K	5499	7	2.34
Blanco 1	2320860074602561408	–	F-K	4987	2	0.41
Blanco 1	2320881377640416640	–	F-K	4301	3	1.18
Blanco 1	2320869897192498432	CD-30 19800	F8	6070	1	2.65
Blanco 1	2320795031617857152		F-K	4977	3	3.15
Blanco 1	2320872650266808192	–	F-K	4873	3	4.14
Blanco 1	2320847533296914560	–	F-K	4579	4	6.47
Gulliver 6	3217389348947353728	HD 290674	A0	9034	1	6.41
IC 2602	5239841340702856960	HD 93405	F3/5V	6383	5	0.75
IC 2602	5239660372284736896	–	-	5362	4	3.80
IC 2602	5239626420542800512	V570 Car	G9Ve	5071	2	1.21
IC 2602	5239498744077038976	HD 310131	G6V	5583	2	0.62
IC 2602	5253546997989686912	HD 307772	G7Ve	5161	3	0.32
IC 2602	5251470948229949568	–	–	5768	1	3.02
Mamajek 1	5209082129256747008	EG Cha	K4Ve	4365	8	4.35
Mamajek 1	5209135352491538432	EO Cha	M0	4089	3	22.26
Mamajek 1	5209038423669475712	EL Cha	M2	3526	6	1.84
Mamajek 1	5215178848217868288	–	M3	3673	2	2.96
Mamajek 1	5209118305765620096	EQ Cha	M3	3367	14	1.25
NGC 1662	3294740954034417792	–	–	4454	1	–
NGC 1662	3295557822453425792	–	–	4447	1	–
NGC 2422	3030122727536859008	–	–	4826	1	6.97
NGC 2451A	5538425822158520576	–	–	3761	2	0.52

Table 1. Continued.

Cluster	*Gaia* DR2 ID	Name	Sp. type	T_{eff}	N_{fl}	P_{rot} [days]
NGC 2451B	5538722449779987072	–	–	4438	1	0.50
NGC 2451B	5538818176010943488	–	–	5326	5	1.95
NGC 2516	5290732721731067136	–	–	4882	2	2.07
NGC 2516	5290719115275116288	–	A7III	7038	1	1.02
NGC 2548	3064487035741401984	–	A2/4	8160	1	0.80
NGC 6281	5976330585929049600	V948 Sco	ApSi	8553	1	1.64
Platais 8	5305106426785000448	CPD-55 1885	G5V	5511	3	0.92
Platais 8	5303854293507991680	HD 78027	A1V	8521	1	3.31
Platais 8	5310127655876188544	CD-55 2543	G8V	5406	1	3.84
Platais 9	5427272240335502848	–	–	3316	1	–
Platais 9	5427469843189439360	–	–	3759	1	3.49
Platais 9	5423893028786327168	HD 80484	A1V	8884	1	0.69
Platais 9	5327362504934951040		–	5732	1	1.23
Melotte 111	3959841756787187456	–	M3.0	3395	2	–
Melotte 111	4002505586787874560	–	M3.5	3421	5	–
Melotte 111	3960130997064687616	–	M3.5	3783	5	–
Melotte 111	4008440617411511552	Sand 64	M3.9	3921	2	–
Melotte 111	4009049575054518400	–	M2.4	3789	1	–
Melotte 111	3954074577781239936	Sand 63	M2.2	3628	2	–
Melotte 111	4009398051520907008	HK Com	M4.2	3848	4	–
Melotte 111	4009440382718550272	–	M3.7	3937	1	–
Melotte 111	4009455054326835968	–	M2.6	3899	3	3.39
Melotte 111	4002543008838439296	–	M3.8	–	1	1.87

[a] HD 290527 is probably a member of Gulliver 6 cluster, see text for details.

3. Discussion

3.1. Spectral distribution of selected flare stars

Most of stellar flares occur in red dwarfs, more often in cool M dwarfs (Güdel & Naz, 2009). Data from the first data release of *TESS* mission confirm it: among 1228 flare stars detected by Günther et al. (2020), 673 objects were classified as M dwarfs. Our data is in a good agreement with these previous studies. Figure 3 presents the histogram of the number of flare stars versus spectral type based on the data from Table 1. Indeed, the majority of selected objects are stars of late spectral type.

M-type dwarfs are very faint objects, an absolute visual magnitude of M0V star is $M_V = 9.0$ mag and for M5V is $M_V = 14.6$ mag (Schmidt-Kaler, 1982). In our work, we found M-type flare stars only in two nearby open clusters, Mamajek 1 (distance $D = 98.72$ pc) and Mel 111 ($D = 96$ pc). Figure 4 shows that flares were detected for almost 50 % of all considered M-type stars.

Stellar flares have been previously detected in some hot B–A type stars (in optical range (Schaefer, 1989; Balona, 2012); in X-ray (Schmitt et al., 1994; Yanagida et al., 2007)). Several objects from our sample are also early spectral type flare stars. In this study, we detected flares in seven A-type stars (Table 1). One of them – V948 Sco – belongs to α^2 CVn variables, chemically peculiar main sequence stars with a strong magnetic field. For all other A-type stars, the variability was registered for the first time.
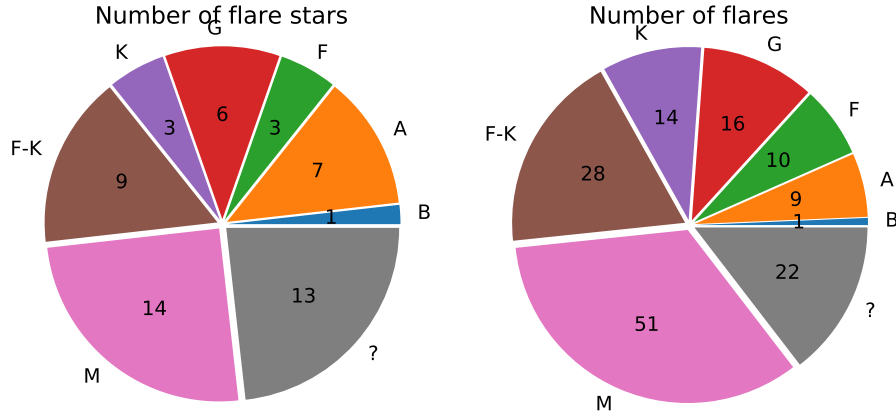
Figure 3. Distribution of flare stars in our sample (left panel), and detected flares from them (right panel) over spectral types from Table 1.

Another selected hot star is HD 36030, classified as B9V star by Houk & Swift (1999). Figure 5 presents the light curve of HD 36030 and a clearly detected flare. As in the case with A-type stars, we did not find any previously published work about variability of this object.

Flares of hot stars may be explained through binarity. As mostly A-type stars are probably double or multiple systems, it is natural to expect flares to originate in a cool companion. However, Balona (2019) gives strong arguments that flares originate in A-type stars themselves. These arguments are based on ratio of luminosity: an M- or K-type companion is about 50–100 times less luminous than an A-type star. The flare amplitude originating in a cool companion should therefore, on average, appears to be about 50–100 times smaller when observed together with A-type star. However, flares detected in hot stars are comparable with their luminosity (Balona, 2019). Flares in A-stars of our sam-
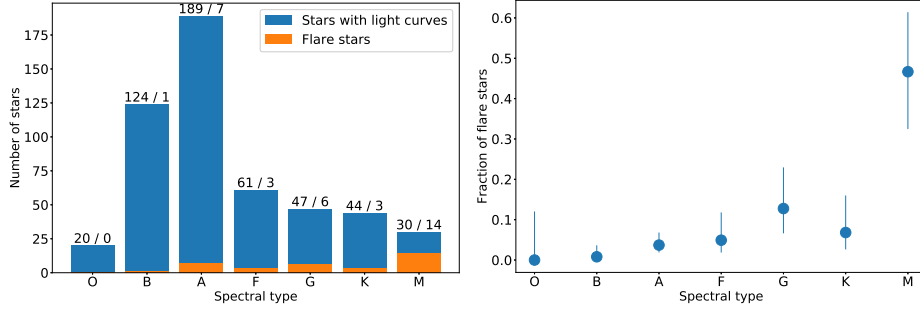
Figure 4. Left panel – histogram of total number of light curves and flare stars among them per spectral type (where it was reliably determined).
Right panel – fraction of flare stars as a function of spectral type. Error bars depict the 90 % confidence intervals for the corresponding values.
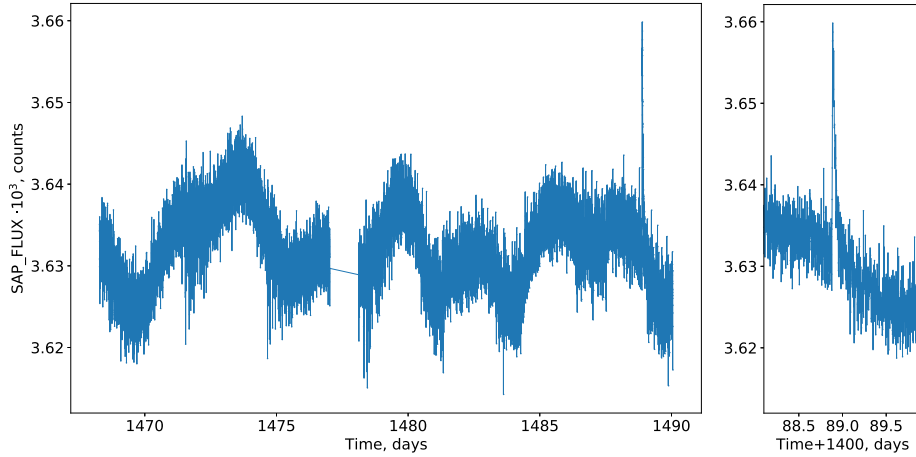
Figure 5. Light curve of HD 36030 (B9V) with a clearly detected flare.

ple have amplitudes of couple percents only, and may be in principle, at least partially, explained by a giant flares with amplitudes of several magnitudes on a late type companion, like the ones reported in Beskin et al. (2017). However, such giant flares are quite rare, and are not detected in our sample of M stars. Thus, we may not expect them to be abundant among the possible components of our A stars too. On the other hand, magnetic interaction with the companion star could provide a plausible explanation for observed flaring activity (Balona, 2012).

According to Balona (2015), the relative number of flare stars from cool M dwarfs to hot A-type stars is probably the same. According to our results (see

Figure 4), the fraction of flare stars among G-M type objects is significantly higher.

There are already no published data about spectral types for fourteen flare stars in our sample (see Table 1, Figure 3). Future spectral observations of these objects could improve statistics.

3.2. Statistical analysis of flares

The mean duration of flares for stars in Table 1 varies between 20 to 70 minutes. This timescale is comparable with the one of GOES X-class solar flares, quite often visible in the white light (Harra et al., 2016). Only 4 stars among 56 analysed in this paper have more than 5 flares during period of *TESS* observations. One of them is EQ Cha (M3) – variable star of Orion type, close visual binary (Sicilia-Aguilar et al., 2009) and a member of Mamajek 1 open cluster. It showed 14 flares during 25 days of observations. Flaring activity of EQ Cha star has been already reported in X-ray by López-Santiago et al. (2010).
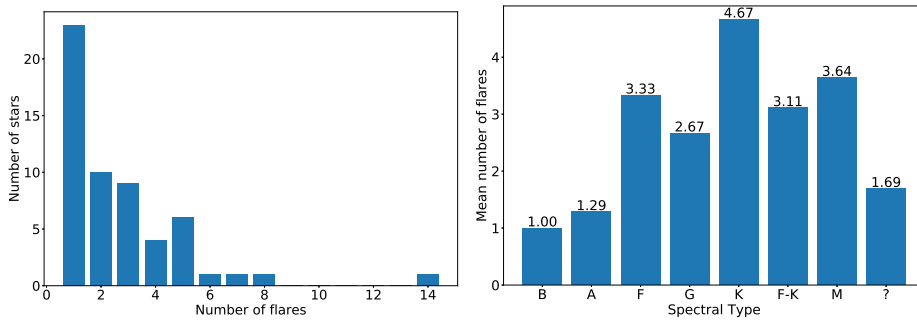
Figure 6. Histogram of number of flares detected from a star (left panel). Mean number of flares per star depending on spectral class from Table 1 (right panel).

On the right panel of Figure 6, we can see that K-type stars have the largest mean flare activity in their light curves. The largest number of flares belongs to M-type stars, which are all earlier than M4 in our sample (see Table 1) and thus are cool stars with convective envelope, as well as to K-type stars. These K and early M dwarfs, which retain a radiative core, presumably all have a quite efficient solar-type dynamo powering their magnetic activity. On the other hand, M dwarfs of spectral type later than M4 are fully convective, and have a turbulent dynamo at work (Wright et al., 2011; Stassun et al., 2011). The activity of G-type stars could be also associated with their convective envelopes. Figure 7 shows the dependence of a flare rate on the star' effective temperature.

The appearance of spots on the surface of stars and stellar flares are clear evidences of stellar magnetism. The connection between stellar rotation and magnetic activity has been studied in many works. For example, Guo et al.
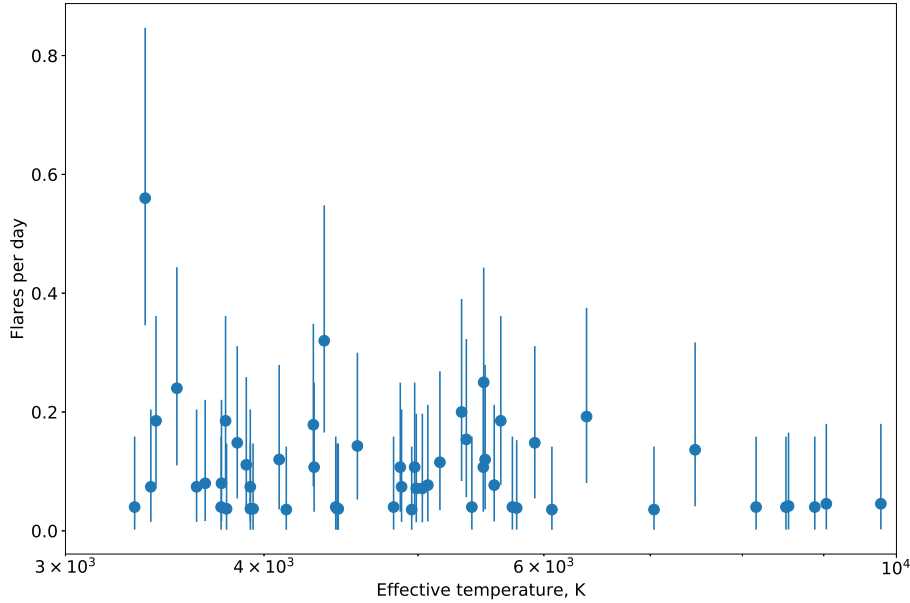
Figure 7. Rate of stellar flares as a function of temperature. Error bars correspond to the 90 % confidence intervals computed assuming Poissonian statistics.

(2014) analyzed X-class flares of Sun during the 22nd and 23rd solar cycles, and they found that flares closely follow the same 11 year cycle as sunspots. Doyle et al. (2018) did not find any correlation between the rotation phase and the number of flares for M-dwarfs based on *Kepler* data, but clearly detected the decrease of flaring activity for rotational periods longer than 10 days. The same dependence is seen in X-ray activity-rotation relation (Pizzocaro et al., 2019).

Figure 8 shows the dependence of flaring activity in our sample, estimated as a number of flares per day of observations on the rotational period of the star. We may spot just a slight trend of decreasing activity towards slower rotation. While we may not stress it as a significant dependence, let's note that it agrees with the expected behaviour of magnetic activity being as a result of internal magnetic dynamo, arising from the combination of stellar differential rotation and convection in the sub-photospheric layers.

3.3. Age distribution of flare stars

Mamajek 1 is the youngest open cluster among ones where we have found flare stars. Its age is 6 Myr. The oldest one where we have found flare is the cluster NGC 1662. Its age 1 Gyr is comparable with the maximal lifetime of open clusters (Fujii & Portegies Zwart, 2016). The ages of all examined clusters span from 1 Myr (IC 5146, the youngest) to 4.3 Gyr (NGC 188, the oldest one). Therefore,
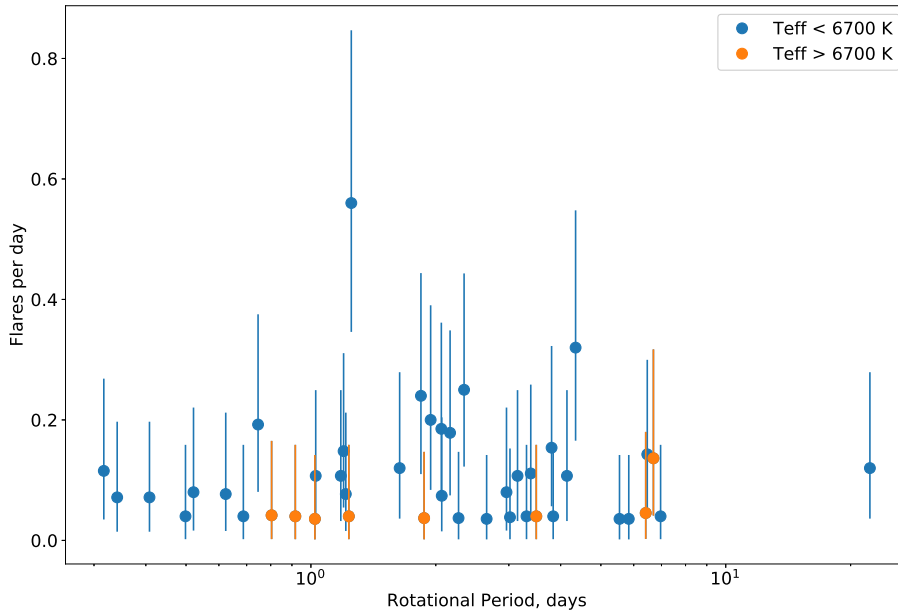
Figure 8. Rate of stellar flares as a function of rotational period. Error bars correspond to the 90 % confidence intervals computed assuming Poissonian statistics.

the collected data do not allow us to confidently determine the age after which flare stars in clusters disappear.

Figure 9 shows how flaring activity changes with stellar age. The resulting distribution is mostly flat, with just a single deviating point with 14 detected flares from EQ Cha star. We therefore cannot reliably see any dependence of flaring activity on the age.

4. Conclusion

In order to study the dependence of stellar flaring activity on the age, we performed an uniform study of large sample of Galactic open clusters from catalogue of Cantat-Gaudin et al. (2018a). We analyzed a total amount of 957 high-cadence *TESS* light curves for stars from 136 open clusters. By visual inspection and later using a `FLATW'RM` code, it finally turned out that 56 of them are flare stars with 151 flares detected.

41.5 % of all flares were detected in cool stars. 8 flare stars belong to B- and A-type stars. The flare activity was detected for the first time for all these hot stars. The flare with the largest amplitude appears on M3-type EQ Cha star. From total amount of detected flare stars in our sample, 25 % of them
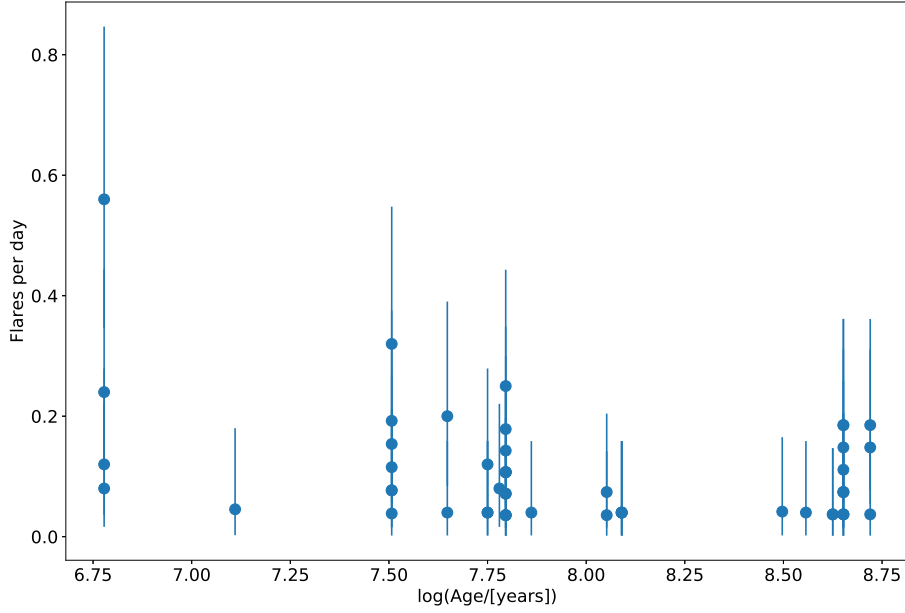
Figure 9. Rate of flares as a function of age. The rate was estimated from the number of detected flares divided by the effective light curve duration for every individual star. Error bars depict the 90 % confidence intervals computed assuming Poissonian statistics.

are members of spectral type M, 11 % are G-type stars and about 5.5% F- and K-type stars.

Statistical analysis of detected flare stars shows that:

- among cool stars up to 50 % have flares, while among A-type stars it is only 3.7 %.

- duration of flares varies between 20 to 70 minutes.

- we found no significant link between rotation rate and flare activity.

- we found no significant link between stellar age and flare activity.

In the study, we used *TESS* data recorded at 2-minute cadence light curves, which are an invaluable source of photometric data for various kinds of stars, pre-selected before the mission start. Although *TESS* full-frame images have a much wider coverage of objects, limited only by crowding, their utility for studies of stellar flares are significantly lower due to much worse temporal resolution (30 minutes, which is comparable to total duration of flares). As TESS mission now continues into its third year, re-visiting the regions of the sky already observed

before, we expect to get more data for the objects we studied in the future. In the future, we plan to do spectroscopic observations of B-A type stars with flare activity we had detected, in order to investigate their possible multiplicity.

References

Balona, L. A., Kepler observations of flaring in A-F type stars. 2012, *Monthly Notices of the RAS*, **423**, 3420, DOI: 10.1111/j.1365-2966.2012.21135.x

Balona, L. A., Flare stars across the H-R diagram. 2015, *Monthly Notices of the RAS*, **447**, 2714, DOI: 10.1093/mnras/stu2651

Balona, L. A., Pulsation, Rotation and Flares in A Stars. 2019, in IAU Symposium, Vol. **339**, *Southern Horizons in Time-Domain Astronomy*, ed. R. E. Griffin, 77–82

Barnes, S. A., Ages for illustrative field stars using gyrochronology: viability, limitations and errors. 2007, *Astrophysical Journal*, **669**, 1167, DOI: 10.1086/519295

Beskin, G., Karpov, S., Plokhotnichenko, V., Stepanov, A., & Tsap, Y., Polarimetric Observations of Flare Stars. 2017, in Astronomical Society of the Pacific Conference Series, Vol. **510**, *Stars: From Collapse to Collapse*, ed. Y. Y. Balega, D. O. Kudryavtsev, I. I. Romanyuk, & I. A. Yakunin, 303

Bossini, D., Vallenari, A., Bragaglia, A., et al., Age determination for 269 Gaia DR2 open clusters. 2019, *Astronomy and Astrophysics*, **623**, A108, DOI: 10.1051/0004-6361/201834693

Cantat-Gaudin, T., Jordi, C., Vallenari, A., et al., A Gaia DR2 view of the open cluster population in the Milky Way. 2018a, *Astronomy and Astrophysics*, **618**, A93, DOI: 10.1051/0004-6361/201833476

---

[3]`https://www.cosmos.esa.int/gaia`

[4]`https://www.cosmos.esa.int/web/gaia/dpac/consortium`

Cantat-Gaudin, T., Vallenari, A., Sordo, R., et al., Characterising open clusters in the solar neighbourhood with the Tycho-Gaia Astrometric Solution. 2018b, *Astronomy and Astrophysics*, **615**, A49, DOI: 10.1051/0004-6361/201731251

Chen, Y., Girardi, L., Bressan, A., et al., Improving PARSEC models for very low mass stars. 2014, *Monthly Notices of the RAS*, **444**, 2525, DOI: 10.1093/mnras/stu1605

Davenport, J. R. A., The Kepler Catalog of Stellar Flares. 2016, *Astrophysical Journal*, **829**, 23, DOI: 10.3847/0004-637X/829/1/23

Doyle, L., Ramsay, G., Doyle, J. G., Wu, K., & Scullion, E., Investigating the rotational phase of stellar flares on M dwarfs using K2 short cadence data. 2018, *Monthly Notices of the RAS*, **480**, 2153, DOI: 10.1093/mnras/sty1963

Evans, D. W., Riello, M., De Angeli, F., et al., Gaia Data Release 2. Photometric content and validation. 2018, *Astronomy and Astrophysics*, **616**, A4, DOI: 10.1051/0004-6361/201832756

Fujii, M. S. & Portegies Zwart, S., The Formation and Dynamical Evolution of Young Star Clusters. 2016, *Astrophysical Journal*, **817**, 4, DOI: 10.3847/0004-637X/817/1/4

Gaia Collaboration, Brown, A. G. A., Vallenari, A., et al., Gaia Data Release 2. Summary of the contents and survey properties. 2018, *Astronomy and Astrophysics*, **616**, A1, DOI: 10.1051/0004-6361/201833051

Gaia Collaboration, Prusti, T., de Bruijne, J. H. J., et al., The Gaia mission. 2016, *Astronomy and Astrophysics*, **595**, A1, DOI: 10.1051/0004-6361/201629272

Güdel, M. & Naz, Y., X-ray spectroscopy of stars. 2009, *The Astronomy and Astrophysics Review*, **447**, 309, DOI: 10.1007/s00159-009-0022-4

Günther, M. N., Zhan, Z., Seager, S., et al., Stellar Flares from the First TESS Data Release: Exploring a New Sample of M Dwarfs. 2020, *Astronomical Journal*, **159**, 60, DOI: 10.3847/1538-3881/ab5d3a

Guo, J., Lin, J., & Deng, Y., The dependence of flares on the magnetic classification of the source regions in solar cycles 22-23. 2014, *Monthly Notices of the RAS*, **441**, 2208, DOI: 10.1093/mnras/stu695

Harra, L. K., Schrijver, C. J., Janvier, M., et al., The Characteristics of Solar X-Class Flares and CMEs: A Paradigm for Stellar Superflares and Eruptions? 2016, *Solar Physics*, **291**, 1761, DOI: 10.1007/s11207-016-0923-0

Houk, N. & Swift, C., Michigan catalogue of two-dimensional spectral types for the HD Stars, Vol. 5. 1999, *Michigan Spectral Survey*, **5**, 0

Lawson, K. D., Wisniewski, J. P., Bellm, E. C., Kowalski, A. F., & Shupe, D. L., Identification of Stellar Flares Using Differential Evolution Template Optimization. 2019, *Astronomical Journal*, **158**, 119, DOI: 10.3847/1538-3881/ab3461

Lippincott, S. L., Search for flares of dM stars on the sproul astrometric programm . 1952, *Astrophysical Journal*, **115**, 582, DOI: 10.1086/145584

López-Santiago, J., Albacete Colombo, J. F., & López-García, M. A., Deep XMM-Newton observation of the η Chamaleontis cluster. 2010, *Astronomy and Astrophysics*, **524**, A97, DOI: 10.1051/0004-6361/201015306

Netopil, M., Paunzen, E., & Cararro, G., A comparative study on the reliability of open cluster parameters. 2015, *Astronomy and Astrophysics*, **582**, 19, DOI: 10.1051/0004-6361/201526372

Pizzocaro, D., Stelzer, B., Poretti, E., et al., Activity and rotation of the X-ray emitting Kepler stars. 2019, *Astronomy and Astrophysics*, **628**, A41, DOI: 10.1051/0004-6361/201731674

Röser, S., Schilbach, E., & Goldman, B., Nine new open clusters within 500 pc from the Sun. 2016, *Astronomy and Astrophysics*, **595**, A22, DOI: 10.1051/0004-6361/201629158

Schaefer, B. E., Flashes from Normal Stars. 1989, *Astrophysical Journal*, **337**, 927, DOI: 10.1086/167162

Schmidt-Kaler, T. 1982, *Stars and Star Clusters, ed. K. Schaifers & H. H. Voigt*

Schmitt, J. H. M. M., Guedel, M., & Predehl, P., Spatially resolved X-ray and radio observations of Castor A+B+C. 1994, *Astronomy and Astrophysics*, **287**, 843

Sicilia-Aguilar, A., Bouwman, J., Juhász, A., et al., The Long-Lived Disks in the η Chamaeleontis Cluster. 2009, *Astrophysical Journal*, **701**, 1188, DOI: 10.1088/0004-637X/701/2/1188

Stassun, K. G., Hebb, L., Covey, K., et al., The M4 Transition: Toward a Comprehensive Understanding of the Transition into the Fully Convective Regime. 2011, in Astronomical Society of the Pacific Conference Series, Vol. **448**, *16th Cambridge Workshop on Cool Stars, Stellar Systems, and the Sun*, ed. C. Johns-Krull, M. K. Browning, & A. A. West, 505

Vida, K. & Roettenbacher, R. M., Finding flares in Kepler data using machine-learning tools. 2018, *Astronomy and Astrophysics*, **616**, 163, DOI: https://doi.org/10.1051/0004-6361/201833194

Wright, N. J., Drake, J. J., Mamajek, E. E., & Henry, G. W., The Stellar-activity-Rotation Relationship and the Evolution of Stellar Dynamos. 2011, *Astrophysical Journal*, **743**, 48, DOI: 10.1088/0004-637X/743/1/48

Yanagida, T., Ezoe, Y., Kawaharada, M., Kokubun, M., & Makishima, K., Large X-ray Flares from B-Type Stars, HD261902 and HD47777, in NGC2264 Observed with CHANDRA. 2007, *Astronomical Society of the Pacific Conference Series*, **361**, 533

Yen, S. X., Reffert, S., Schilbach, E., et al., Reanalysis of nearby open clusters using Gaia DR1/TGAS and HSOY. 2018, *Astronomy and Astrophysics*, **615**, A12, DOI: 10.1051/0004-6361/201731905

A. Clusters with *TESS* light curves available

Table 2. Complete list of Galactic open clusters investigated in this work, with ages τ taken from various sources (see the last column), distances D and number of members N_{mem} taken from Cantat-Gaudin et al. (2018a), number of available light curves N_{lc} in the *TESS* database and number of flare stars N_{fs} estimated in this work.

Name	$\log(\tau/[\mathrm{yr}])$	D [pc]	N_{mem}	N_{lc}	N_{fs}	Reference for age
Alessi 13	8.72	104.34	48	10	3	Yen et al. (2018)
Alessi 19	7.38	584.80	74	1	0	Bossini et al. (2019)
Alessi 20	8.22	432.71	124	2	0	WEBDA[a]
Alessi 21	7.816	581.40	137	2	0	Bossini et al. (2019)
Alessi 24	7.945	485.67	163	1	0	Bossini et al. (2019)
Alessi 3	8.90	280.43	178	8	0	Yen et al. (2018)
Alessi 37	8.125	722.54	142	1	0	Bossini et al. (2019)
Alessi 43	7.48	968.99	318	2	0	WEBDA
Alessi 5	7.723	399.84	302	3	0	Bossini et al. (2019)
Alessi 9	8.42	207.38	194	5	0	Yen et al. (2018)
Alessi Teutsch 12	7.977	612.75	44	1	0	Bossini et al. (2019)
Alessi Teutsch 5	7.02	900.09	158	1	0	WEBDA
Alessi Teutsch 8	8.65	1034.13	341	2	0	WEBDA
ASCC 105	7.994	560.85	127	1	0	Bossini et al. (2019)
ASCC 10	8.599	685.40	71	1	0	Bossini et al. (2019)
ASCC 12	8.42	1062.70	162	1	0	WEBDA
ASCC 16	7.047	352.36	226	9	0	Bossini et al. (2019)
ASCC 19	7.086	361.27	188	3	1	Bossini et al. (2019)
ASCC 21	7.032	348.92	131	3	1	Bossini et al. (2019)
ASCC 32	7.404	813.01	259	2	0	Bossini et al. (2019)
ASCC 58	7.826	485.44	137	2	0	Bossini et al. (2019)
ASCC 79	6.86	850.34	129	1	0	Bossini et al. (2019)
ASCC 85	7.42	893.66	119	1	0	WEBDA
Aveni Hunter 1	8.26	425.89	82	3	0	WEBDA
Basel 8	8.102	1600.00	33	1	0	WEBDA
Berkeley 86	7.116	1792.11	31	2	0	WEBDA
Berkeley 87	7.152	1745.20	131	1	0	WEBDA
BH 164	7.81	423.01	209	2	0	Bossini et al. (2019)
BH 221	8.01	1131.22	162	1	0	WEBDA
BH 23	7.14	443.07	94	1	0	WEBDA
BH 56	7.24	927.64	122	3	0	WEBDA

Table 2. Continued.

Name	$\log(\tau/[\mathrm{yr}])$	D [pc]	N_{mem}	N_{lc}	N_{fs}	Reference for age
BH 99	7.908	449.44	389	1	0	Bossini et al. (2019)
Biurakan 2	7.011	1845.02	68	2	0	WEBDA
Blanco 1	7.975	237.53	381	82	12	Bossini et al. (2019)
Bochum 13	6.823	1763.67	73	1	0	WEBDA
Collinder 106	6.74	1574.80	114	1	0	WEBDA
Collinder 107	7.00	1620.75	159	1	0	WEBDA
Collinder 132	7.08	666.22	99	1	0	WEBDA
Collinder 135	7.407	305.06	352	1	0	WEBDA
Collinder 197	7.128	967.12	243	4	0	WEBDA
Collinder 258	7.834	1308.90	124	1	0	Bossini et al. (2019)
DBSB 104		1101.32	27	1	0	
Dolidze 8		1007.05	43	3	0	
FSR 0771	8.195	1618.12	48	1	0	Bossini et al. (2019)
FSR 0951	8.589	1808.32	195	1	0	Bossini et al. (2019)
Gulliver 11		942.51	64	1	0	
Gulliver 21	8.472	664.89	126	1	0	Bossini et al. (2019)
Gulliver 6		422.48	343	6	2	
Gulliver 9	7.154	503.78	265	1	0	Bossini et al. (2019)
Haffner 13	7.497	574.05	210	1	0	Bossini et al. (2019)
Harvard 10	7.899	705.22	164	1	0	Bossini et al. (2019)
Harvard 5	7.812	1308.90	52	1	0	Bossini et al. (2019)
IC 1396	7.054	938.09	460	2	0	WEBDA
IC 2391	7.561	151.93	224	7	0	Bossini et al. (2019)
IC 2395	7.223	725.16	297	4	0	WEBDA
IC 2488	8.2	1392.76	435	1	0	Bossini et al. (2019)
IC 2602	7.547	152.42	311	33	6	Bossini et al. (2019)
IC 2714	8.55	1390.82	934	1	0	Bossini et al. (2019)
IC 4651	9.057	946.97	854	8	0	WEBDA
IC 5146	6.00	824.40	108	2	0	WEBDA
King 6	8.582	742.94	234	1	0	Bossini et al. (2019)
L 1641S		437.06	101	1	0	
Mamajek 1	6.778	98.72	20	9	5	WEBDA
Mamajek 4	8.824	449.64	199	3	0	Bossini et al. (2019)
Melotte 111	8.652	96^b	859	98	10	WEBDA
Melotte 20	7.938	176.43	764	50	0	Bossini et al. (2019)
Melotte 22	7.937	136.13	992	5	0	Bossini et al. (2019)
Muzzio 1		1926.78	40	1	0	

Table 2. Continued.

Name	$\log(\tau/[\mathrm{yr}])$	D [pc]	N_{mem}	N_{lc}	N_{fs}	Reference for age
NGC 129	7.886	1956.95	392	1	0	WEBDA
NGC 1333		299.04	50	3	0	
NGC 1545	8.019	731.53	139	1	0	Bossini et al. (2019)
NGC 1579		552.49	56	2	0	
NGC 1662	8.957	416.67	238	24	2	Bossini et al. (2019)
NGC 188	9.632	1972.39	864	3	0	WEBDA
NGC 1901	8.918	424.09	75	15	0	Bossini et al. (2019)
NGC 2232	7.87	326.05	198	2	0	WEBDA
NGC 2244	6.896	1620.75	623	13	0	WEBDA
NGC 2287	8.486	735.29	645	1	0	Bossini et al. (2019)
NGC 2323	7.975	1003.01	866	1	0	Bossini et al. (2019)
NGC 2354	8.126	1328.02	276	2	0	WEBDA
NGC 2422	8.104	483.09	442	43	1	Bossini et al. (2019)
NGC 2423	8.991	956.94	430	1	0	Bossini et al. (2019)
NGC 2437	8.390	1658.37	1797	1	0	WEBDA
NGC 2451A	7.647	193.61	337	26	1	Bossini et al. (2019)
NGC 2451B	7.592	367.78	298	15	2	Bossini et al. (2019)
NGC 2516	8.4	413.74	798	144	1	Bossini et al. (2019)
NGC 2546	7.962	967.12	165	1	0	Bossini et al. (2019)
NGC 2547	7.432	391.70	233	4	0	Bossini et al. (2019)
NGC 2548	8.557	775.80	479	37	1	WEBDA
NGC 3114	8.093	1048.22	1296	6	0	WEBDA
NGC 3532	8.601	484.03	1889	11	0	Bossini et al. (2019)
NGC 3680	9.077	1071.81	100	8	0	WEBDA
NGC 5662	7.968	776.40	255	1	0	WEBDA
NGC 5822	8.95	842.46	667	1	0	Bossini et al. (2019)
NGC 6124	8.147	642.26	1327	1	0	WEBDA
NGC 6178	7.248	909.92	45	1	0	WEBDA
NGC 6193	6.775	1231.53	465	2	0	WEBDA
NGC 6231	6.843	1697.79	653	11	0	WEBDA
NGC 6242	7.767	1324.50	523	1	0	Bossini et al. (2019)
NGC 6250	7.415	1012.15	85	1	0	WEBDA
NGC 6281	8.497	533.90	513	6	0	WEBDA
NGC 6475	8.477	279.96	941	29	0	Bossini et al. (2019)
NGC 6811	8.936	1149.43	306	4	0	Bossini et al. (2019)
NGC 6866	8.89	1457.73	104	1	0	Bossini et al. (2019)
NGC 6871	6.958	1945.53	594	11	0	WEBDA

Table 2. Continued.

Name	$\log(\tau/[\text{yr}])$	D [pc]	N_{mem}	N_{lc}	N_{fs}	Reference for age
NGC 6910	7.127	1834.86	159	2	0	WEBDA
NGC 6913	7.111	1808.32	89	2	0	WEBDA
NGC 6940	9.01	1055.97	593	4	0	Bossini et al. (2019)
NGC 7092	8.491	299.67	161	6	0	Bossini et al. (2019)
NGC 7129		920.81	36	1	0	
NGC 7243	8.006	896.06	313	2	0	Bossini et al. (2019)
NGC 743		1135.07	62	1	0	
NGC 752	9.05	446.63	240	9	0	WEBDA
Pismis 5	7.197	974.66	92	1	0	WEBDA
Platais 3	8.319	177.94	90	12	0	Bossini et al. (2019)
Platais 8	7.75	134.86	211	13	3	WEBDA
Platais 9	7.894	183.05	128	18	4	Bossini et al. (2019)
Pozzo 1	7.117	350.51	390	3	0	Bossini et al. (2019)
Roslund 3	7.643	1709.40	112	1	0	Bossini et al. (2019)
RSG 5	7.70	339.56	173	1	0	Röser et al. (2016)
RSG 7	8.30	427.90	133	1	0	Röser et al. (2016)
RSG 8	8.50	452.49	211	1	0	Röser et al. (2016)
Ruprecht 91	6.90	1078.75	214	2	0	WEBDA
Stephenson 1	7.435	359.84	97	3	0	Bossini et al. (2019)
Stock 12	8.188	442.28	109	2	0	Bossini et al. (2019)
Stock 1	8.676	408.66	183	2	0	Bossini et al. (2019)
Stock 23	7.973	619.96	89	3	0	Bossini et al. (2019)
Stock 2	8.23	378.64	1190	1	0	WEBDA
Stock 5	7.73	987.17	115	1	0	WEBDA
Stock 7	7.214	693.96	141	1	0	WEBDA
Teutsch 38	8.14	665.78	109	1	0	WEBDA
Trumpler 10	7.74	437.25	478	2	0	Bossini et al. (2019)
Trumpler 2	7.962	698.81	179	2	0	Bossini et al. (2019)
Trumpler 3	7.83	684.46	222	2	0	WEBDA
Turner 5	8.49	421.41	28	1	0	WEBDA
vdBergh 1	8.025	1912.05	73	1	0	WEBDA

[a] WEBDA database https://webda.physics.muni.cz/

[b] Distance for Melotte 111 are taken from WEBDA.

PRÁCE ASTRONOMICKÉHO OBSERVATÓRIA
NA SKALNATOM PLESE
LI, číslo 1

Zostavovatelia:	RNDr. Richard Komžík, CSc.
	M. Skarka
	J. Janík
	E. Paunzen
	V. Glos
Vedecký redaktor:	RNDr. Augustín Skopal, DrSc.
Vydal:	Astronomický ústav SAV, Tatranská Lomnica
IČO vydavateľa:	00 166 529
Periodicita:	3-krát ročne
ISSN (on-line verzia):	1336-0337
CODEN:	CAOPF8
Rok vydania:	2021
Počet strán:	98

Contributions of the Astronomical Observatory Skalnaté Pleso are processed using
LaTeX 2_ε CAOSP DocumentClass file 3.08 ver. 2020.